CRANFIELD UNIVERSITY

EFSTATHIOS SIAMPIS

OPTIMAL TORQUE VECTORING CONTROL STRATEGIES FOR STABILISATION OF ELECTRIC VEHICLES AT THE LIMITS OF HANDLING

SCHOOL OF AEROSPACE, TRANSPORT AND MANUFACTURING
Advanced Vehicle Engineering Centre

PhD
Academic Year: 2016–2017

Supervisor: Dr E. Velenis and Dr S. Longo
October 2016

CRANFIELD UNIVERSITY

SCHOOL OF AEROSPACE, TRANSPORT AND MANUFACTURING
Advanced Vehicle Engineering Centre

PhD

Academic Year: 2016–2017

EFSTATHIOS SIAMPIS

Optimal Torque Vectoring Control Strategies for Stabilisation of Electric Vehicles at the Limits of Handling

Supervisor: Dr E. Velenis and Dr S. Longo
October 2016

This thesis is submitted in partial fulfilment of the requirements for the degree of PhD.

Abstract

The study of chassis control has been a major research area in the automotive industry and academia for more than fifty years now. Among the popular methods used to actively control the dynamics of a vehicle, torque vectoring, the method of controlling both the direction and the magnitude of the torque on the wheels, is of particular interest. Such a method can alter the vehicle's behaviour in a positive way under both sub-limit and limit handling conditions and has become even more relevant in the case of an electric vehicle equipped with multiple electric motors.

Torque vectoring has been so far employed mainly in lateral vehicle dynamics control applications, with the longitudinal dynamics of the vehicle remaining under the full authority of the driver. Nevertheless, it has been also recognised that active control of the longitudinal dynamics of the vehicle can improve vehicle stability in limit handling situations. A characteristic example of this is the case where the driver misjudges the entry speed into a corner and the vehicle starts to deviate from its path, a situation commonly referred to as a 'terminal understeer' condition. Use of combined longitudinal and lateral control in such scenarios have been already proposed in the literature, but these solutions are mainly based on heuristic approaches that also neglect the strong coupling of longitudinal and lateral dynamics in limit handling situations.

The main aim of this project is to develop a real-time implementable multivariable control strategy to stabilise the vehicle at the limits of handling in an optimal way using torque vectoring via the two independently controlled electric motors on the rear axle of an electric vehicle. To this end, after reviewing the most important contributions in the control of lateral and/or longitudinal vehicle dynamics with a particular focus on the limit handling solutions, a realistic vehicle reference behaviour near the limit of lateral acceleration is derived. An unconstrained optimal control strategy is then developed for terminal understeer mitigation. The importance of constraining both the vehicle state and the control inputs when the vehicle operates at the limits of handling is shown by developing a constrained linear optimal control framework, while the effect of using a constrained nonlinear optimal control framework instead is subsequently examined next. Finally an optimal estimation strategy for providing the necessary vehicle state information to the proposed optimal control strategies is constructed, assuming that only common vehicle sensors are available. All the developed optimal control strategies are assessed not only in terms of performance but also execution time, so to make sure they are implementable in real time on a typical Electronic Control Unit.

This research was supported by EPSRC under Grant EP/K502820/1.

Contents

List of Figures

List of Tables

Nomenclature

General

α	Tyre slip angle
β	Vehicle sideslip angle at its centre of mass
δ	Steering angle at the front wheels
δ_{ratio}	Steering gear ratio
ε	Slack variable
μ_x, μ_y	Longitudinal and lateral tyre force coefficient
μ_{max}	Tyre/road friction coefficient
ψ	Vehicle yaw angle at its centre of mass
ω	Wheel angular rate
a_x, a_y	Vehicle longitudinal and lateral acceleration at its centre of mass
c_{aero}	Aerodynamic drag coefficient
c_F, c_R	Front and rear suspension shock absorber damping
f_x, f_y, f_z	Longitudinal, lateral and normal tyre force
g	Constant of gravitational acceleration
h	Vertical distance of centre of mass from the ground
h_{veh}	Height of the vehicle
i, j	Subscripts $i = F,R$ (front, rear), $j = L,R$ (left, right)
k_{aF}, k_{aR}	Front and rear anti-roll bar torsional stiffness

k_F, k_R	Front and rear suspension spring stiffness
ℓ_F, ℓ_R	Longitudinal distance of centre of mass from the front and the rear track
ℓ_{veh}	Length of the vehicle
m	Mass of the vehicle
m_w	Mass of the wheel
s, s_x, s_y	Total, longitudinal and lateral tyre slip
w_L, w_R	Lateral distance of centre of mass from the left and right wheels
w_{veh}	Width of the vehicle
B_{MF}	Pacejka's Magic Formula stiffness factor
C_{MF}	Pacejka's Magic Formula shape factor
D_{MF}	Pacejka's Magic Formula peak value
E_{MF}	Pacejka's Magic Formula curvature shift
S_h	Pacejka's Magic Formula horizontal shift
S_v	Pacejka's Magic Formula vertical shift
I_w	Wheel moment of inertia of each wheel about its axis of rotation
I_x	Vehicle moment of inertia about its horizontal axis
I_y	Vehicle moment of inertia about its lateral axis
I_z	Vehicle moment of inertia about its vertical axis
K	Understeer gradient
N	Horizon
N_p	Prediction horizon
N_u	Control horizon
R	Vehicle path radius
R_w	Wheel radius
T	Torque
T_s	Sampling time

T_{sim}	Simulation time
V	Vehicle velocity at its centre of mass
V_{char}	Characteristic vehicle velocity

Signals and matrices

x, u, y	Plant state, input and output vectors
r, l	State and input references
w, v	Process and measurement noises
A, B, C, D	Plant matrices
Q_c, R_c, M_c	Continuous-time state, input and cross weighting matrices
Q_d, R_d, M_d	Discrete-time state, input and cross weighting matrices
Q_e, R_e	Process and measurement covariance matrices

List of Abbreviations

AFS	Active Front Steering
ATTS	Active Torque Transfer System
AYC	Active Yaw Control
ARE	Algebraic Riccati Equation
AWD	All-Wheel Drive
ABS	Anti-lock Braking System
BFGS	Broyden-Fletcher-Goldfarb-Shanno
CM	Centre of Mass
CAN	Controller Area Network
CC	Cruise Control
DOF	Degrees of Freedom
DYC	Direct Yaw Control
DARE	Discrete Algebraic Riccati Equation
EV	Electric Vehicle
ESP	Electronic Stability Program
EUC	Enhanced Understeering Control
EOM	Equations of Motion
EKF	Extended Kalman Filter
EKBF	Extended Kalman-Bucy Filter

4WS	Four Wheel Steering
FWD	Front-Wheel Drive
GPS	Global Positioning System
HIL	Hardware-In-the-Loop
HEV	Hybrid Electric Vehicle
ICE	Internal Combustion Engine
IMU	Inertial Measurement Unit
KF	Kalman Filter
LPV	Linear Parameter Varying
LQG	Linear Quadratic Gaussian
LQR	Linear Quadratic Regulator
LTV	Linear Time Varying
MF	Magic Formula
MPC	Model Predictive Control
MIMO	Multi-Input Multi-Output
NMPC	Nonlinear Model Predictive Control
NLP	NonLinear Program
PDIP	Primal-Dual Interior Point
PID	Proportional-Integral-Derivative
QP	Quadratic Program
RTI	Real Time Iteration
RWD	Rear-Wheel Drive
RHE	Receding Horizon Estimation
RI	Rollover Index
SQP	Sequential Quadratic Program
SMC	Sliding Mode Control

SUV	Sport Utility Vehicle
SH-AWD	Super Handling All-Wheel Drive
TCS	Traction Control System
TtR	Through-the-Road
UKF	Unscented Kalman Filter

Acknowledgements

My warmest gratitude to my mentor Dr Efstathios Velenis for introducing me to vehicle dynamics in my undergraduate years and guiding me through this research work. I would further like to thank Dr Stefano Longo who has been instrumental to the successful completion of this project.

Last but not least I would like to thank Eleni, who supported me under the indispensable grant W1Fe.

List of Publications

The following publications have been produced as a result of the work conducted in this thesis:

Journal articles

- E. Siampis, E. Velenis, and S. Longo. Rear wheel torque vectoring model predictive control with velocity regulation for electric vehicles. Vehicle System Dynamics, vol. 53, no. 11, pages 1555-1579, 2015.

- E. Siampis, S. Gariuolo, E. Velenis, and S. Longo. A Real-Time Nonlinear Model Predictive Control Strategy for Stabilisation of an Electric Vehicle at the Limits of Handling. Submitted for journal publication.

Conference papers

- E. Siampis, M. Massaro, and E. Velenis. Electric rear axle torque vectoring for combined yaw stability and velocity control near the limit of handling. In Decision and Control (CDC), 2013 IEEE 52st Annual Conference on, pages 1552-1557, 2013.

- E. Siampis, E. Velenis, and S. Longo. Model predictive torque vectoring control for electric vehicles near the limits of handling. In Control Conference (ECC), 2015 European, pages 2553-2558, 2015.

- E. Siampis, E. Velenis, and S. Longo. Front-to-rear torque vectoring Model Predictive Control for terminal understeer mitigation. In Proceedings of the 24th Symposium of the International Association for Vehicle System Dynamics (IAVSD), pages 153-160, 2015.

- E. Siampis, E. Velenis, and S. Longo. Predictive Rear Wheel Torque Vectoring Control with Terminal Understeer Mitigation using Nonlinear Estimation. In Decision and Control (CDC), 2015 IEEE 54st Annual Conference on, pages 4302-4307, 2015.

Chapter 1

Introduction

1.1 Overview

The study of chassis control has been a major research area for both the automotive industry and academia for more than forty years now. Chassis control can be defined as the control of the longitudinal, lateral and vertical vehicle motion to improve handling and traction/braking performance along with active safety [48]. Although it is a relatively new area of research, it has quickly grown into one of the most intensive subjects with a large volume of published literature [94]. This growth has a direct connection with the increased safety concerns due to the ever increasing number of vehicles on the road, combined with the higher performance found on vehicles today. At the same time, the rapid development of the microprocessor has offered faster and cheaper platforms for deployment of chassis control solutions.

After the introduction of the Anti-lock Braking System (ABS) in 1978 and the Trac-

tion Control System (TCS) five years later, chassis control systems have expanded to include the dynamics of the vehicle as a whole [84]. This was achieved with systems such as Four Wheel Steering (4WS) and semi-active/active suspension in the mid 1980s and braking systems such as the Electronic Stability Program (ESP) ten years later [131]. These systems offered greater control over the dynamics of the vehicle in a closed-loop fashion, differentiating themselves from systems such as the ABS and the TCS which focus on the individual wheels.

From the application methods used so far for control of the vehicle dynamics one method in particular is of great interest: torque vectoring, the method of controlling both the direction and magnitude of torque in order to influence the dynamics of the vehicle in a positive way [145], has attracted increasing attention over the past fifteen years. Torque vectoring on a conventional driveline can be applied between axles or between wheels of the same axle, or even in a front-rear and left-right operation combining axle and centre differentials or couplings. But with the re-emerging technologies of Electric Vehicles (EV) and Hybrid Electric Vehicles (HEV), torque vectoring has become even more important, since these platforms offer greater authority over a conventional driveline when it comes to effectively distributing torque. And while torque vectoring has been so far seen as a system that improves steerability and vehicle response in sub-limit situations, the new possibilities given from the EV and HEV platforms can extend its operation in the limit handling region.

In the context of active chassis control, systems that control the lateral dynamics of the vehicle have been the main topic of research so far. Such systems focus mainly on improving the steerability of the vehicle under sub-limit conditions and preventing loss of control in limit handling situations. Longitudinal vehicle control on the other hand has remained mainly under the command of the driver, with systems like Cruise Control (CC) only recently incorporating safety functions such as regulation of the vehicle's speed

to keep a safe following distance from the vehicle in front. However, it has been also recognised that active control of the longitudinal dynamics can improve the stability of the vehicle in terminal understeer situations.

Understeer along with oversteer and neutral steer are terms commonly used to explain how a vehicle responds to steering inputs. Since the actual connection between the steering angle on the wheels and the response of the vehicle is quite complex, the concept of understeer gradient has been introduced at this point: using a single-track model under steady-state cornering and also assuming that all tyres stay at their linear region of operation, the understeer gradient can give an indication of the natural behaviour of a vehicle subjected to a constant steering input. It can be shown that [113, 133]

$$\delta = \frac{L}{R} + Ka_y,$$

where δ is the steering angle on the front wheels, L the wheelbase of the vehicle, R the vehicle path radius, K the understeer gradient and $a_y = V_x^2/R$ the lateral acceleration of the vehicle at its Centre of Mass (CM). Then a vehicle is:

1. neutral steer when $K = 0$ and there is no need to adjust the steering angle when we vary the vehicle's speed on a constant radius path,

2. understeer when $K > 0$ and the steering angle will have to increase with speed according to Ka_y in order to keep a constant radius path, with the characteristic speed V_{char} defined as the speed at which that steering angle is double the Ackerman angle $\delta_{acker} = L/R$ [50],

3. oversteer when $K < 0$ and the steering angle has to decrease as the speed is increased until it reaches a zero value at the critical speed (Fig. 1.1).

While the use of the understeer gradient as introduced above can somehow quantify

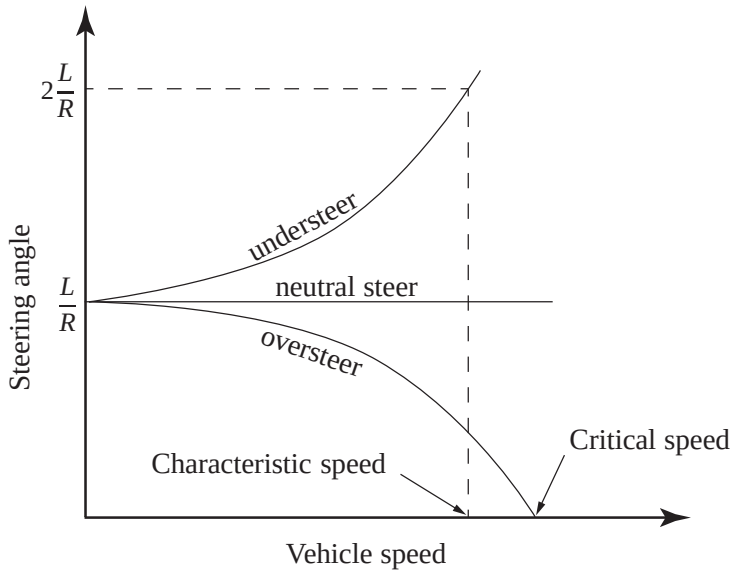

Figure 1.1: Change of steer angle with vehicle speed on a constant radius path for a neutral steer, an understeer and an oversteer vehicle.

the natural tendency of a car to follow a prescribed path radius or not, it is based on many simplifying assumptions. It is therefore important to note at this point that the behaviour of the vehicle while cornering can change depending on the vehicle drivetrain topology and/or the use of the acceleration/brake pedal. This is mainly due to the longitudinal and lateral tyre force coupling effect which dictates that the lateral tyre force capacity of a tyre reduces in the presence of a longitudinal tyre force. Then, for example:

- A Front-Wheel Drive (FWD) vehicle under acceleration while cornering has a smaller lateral force potential on the front tyres and exhibits increased understeer.
- A Rear-Wheel Drive (RWD) vehicle under acceleration while cornering has a smaller lateral force potential on the back tyres and exhibits increased oversteer.

Returning to the limit handling cases, terminal understeer therefore refers to that kind of vehicle operation in which the front tyres have reached their maximum lateral force potential due to excessive vehicle speed through a corner. The necessity for velocity

regulation in terminal understeer situations is already mentioned by van Zanten et al. [139] as part of the performance requirements for the future development of ESP system by Bosch. Van Zanten [139] points out that especially in the case of J-turns, where the turning radius is continuously reduced along the trajectory (a scenario typical on highway exits), the ESP's yaw moment correction on the lateral dynamics alone is not sufficient. In those cases the requirement of minimum speed change from the ESP intervention needs to get reduced in its priority and thus, by appropriately reducing the vehicle's speed the radius of the turn can be decreased as well.

While the necessity to reduce the vehicle's velocity in terminal understeer cases is well documented [53, 89, 106, 139], the method that this velocity reduction will take place remains an open question: proposed solutions range from simple control strategies that superimpose individual braking of all four wheels on the ESP intervention on a standard vehicle [89] to torque vectoring algorithms which combine a high level supervisory controller with a static control allocation scheme on an All-Wheel Drive (AWD) EV [74]. No matter the approach used, a recurring problem in the proposed so far solutions is the assumption that the longitudinal dynamics of the vehicle are decoupled from its lateral dynamics, while it is often the case that a similar assumption is also made on the tyre level by assuming decoupled longitudinal and lateral tyre forces. While it is understood that such assumptions can greatly simplify the control design and minimise computational requirements, they are not valid anymore in limit handling cases.

Another point of interest in limit handling cases is the chosen drivetrain topology, since disturbing the longitudinal dynamics of the vehicle will change its understeer characterisitics as already evidenced above. The drivetrain topology used in this project is that of an RWD EV with two electric motors on the rear axle of the vehicle (refer to Appendix A for details), where the stabilising controller is able to manipulate the motor torques to follow the given reference vehicle behaviour, while the driver reserves full authority

of the steering angle input through which he commands the intended path of the vehicle. While such a drivetrain topology has the advantage that it does not interfere with the lateral tyre forces on the front wheels and the steering feel from the driver, it can result in induced oversteering behaviour on the vehicle, especially in the terminal understeer cases examined here where the desired velocity reduction demands for brake actions on the rear wheels. It is therefore important to carefully consider the vehicle, tyre and motor operation limits in limit handling cases as we are going to see in the chapters to follow.

1.2 Aim and Contribution

The aim of this project is to develop a real-time implementable multivariable control strategy to stabilise an RWD EV using torque vectoring at the limits of handling in an optimal way. While the understeer mitigation capabilities of the proposed control strategy through the necessary reduction of the vehicle's velocity will be the main focus in this project, the final solution will be able to stabilise the vehicle under any limit handling condition including oversteer cases.

To meet this aim, this project has led to the following contributions:

- review the most important contributions in the control of lateral and/or longitudinal vehicle dynamics, with a particular focus on the limit handling solutions (chapter 2),
- based on an original idea from [40], develop a realistic vehicle state reference near the limit of lateral acceleration for the controller to follow (chapter 3),
- based on an original idea from [40], develop an unconstrained optimal solution for terminal understeer mitigation (chapter 4),

- show the importance of constraining both the vehicle state and the control inputs when the vehicle operates at the limits of handling by developing a linear constrained optimal control framework (chapter 5),
- analyse the relative advantages and disadvantages of using a nonlinear constrained optimal control framework (chapter 6),
- develop an optimal estimation strategy for providing the necessary vehicle state information to the proposed optimal control strategies, assuming that no additional sensors than the ones found on a standard vehicle are available (chapter 7).

It is important to note at this point that all the developed strategies will be systematically assessed in terms of real-time feasibility, since in the context of active chassis control strategies like the ones presented here it is important to make sure that all solutions are real-time implementable. To this end, computational times using a standard desktop machine (i7-2600k at 3.40GHz with 16GB of memory) are reported throughout this report, while the final solution is also deployed on a dSPACE DS1005 board (PowerPC 750GX at 1.00GHz with 128MB of memory), the goal being to understand what are the processing requirements if such a solution is to be tested on a real vehicle.

1.3 Thesis Outline

Chapter 2 provides an overview of the most important contributions in the literature on the subject of active chassis control, with a particular focus on the limit handling solutions. We start with solutions that apply only on the lateral vehicle dynamics using conventional drivelines, which consist a major part of the literature. Then, after a short introduction on the distinct advantages and disadvantages of the HEV and EV platforms, we list lateral dynamics control solutions that have been successfully applied on such vehicles. Finally,

we examine more advanced solutions that use longitudinal dynamics control (usually in combination with lateral dynamics control) for terminal understeer mitigation.

Chapter 3 introduces the four-wheel vehicle model and the nonlinear tyre model used in this project, along with the steady-state cornering analysis used to derive the necessary reference for the derived controllers to follow. The target generation is based on the steady-state analysis presented in [40] and employs the same four-wheel vehicle model and tyre model so that the nonlinear tyre characteristics and coupled longitudinal and lateral vehicle dynamics and tyre forces are considered. In this way the computed references are specific to the chosen drivetrain topology and always feasible.

In chapter 4 an unconstrained optimal control strategy using combined yaw, sideslip and velocity regulation for terminal understeer mitigation is presented. To this end, a Linear Quadratic Regulator (LQR) to stabilise the vehicle using combined longitudinal and lateral dynamics control is developed in a way similar to [40], using the rear torque vectoring capabilities of the RWD EV under consideration. It is shown that it can successfully reduce off-tracking by appropriately regulating the vehicle velocity when the car enters a corner with excessive speed.

In chapter 5 two constrained optimal control strategies are presented using combined yaw, sideslip and velocity regulation in the Model Predictive Control (MPC) framework, a feedback implementation of constrained optimal control. The two MPC strategies are constructed using vehicle models or different levels of complexity: the first one linearises the four-wheel model from chapter 3, while the second linearises a reduced system with longitudinal slip inputs instead so that the fast wheel speed dynamics are neglected. After setting the state and input constraints for the MPC strategies, we analyse the relative trade-off in closed-loop performance and computational cost for both of them: it is shown that inclusion of the fast wheel speed dynamics results not only in a bigger optimization problem but also requires faster sampling times. Two limit handling tests confirm the

effectiveness of the two linear MPC strategies in correcting terminal understeer behaviour and the importance of constraining the system state and the inputs for improved stability in an obstacle avoidance scenario.

Chapter 6 examines recent developments in the area of fast linear MPC and Nonlinear MPC (NMPC) solvers, by replacing the generic Quadratic Program (QP) solver used in the previous chapter with a specialised one and by introducing two NMPC strategies using different nonlinear solvers. Comparing the three strategies against each other and against the optimal solution in terms of closed-loop performance and computational cost indicates that while the linear MPC remains the fastest strategy, it also returns solutions that can greatly deviate from the optimal one. The importance of retaining the nonlinear four-wheel vehicle model in an NMPC formulation is also confirmed in two limit handling manoeuvres, which show that using such a solution results in better state regulation and much smoother torque commands.

In chapter 7 the NMPC strategy from the previous chapter is coupled with a nonlinear optimal estimator for estimating the variables of interest. To this end, an Unscented Kalman Filter (UKF) is constructed assuming that only common sensors usually found on a standard vehicle are fitted. The proposed estimation strategy is first tested on a track before combining it the NMPC strategy from chapter 6 in a highly transient test scenario, with results showing that the complete solution is still effective in controlling the vehicle in limit handling cases.

Chapter 2

Active Chassis Control: A Literature Review

2.1 Introduction

In this chapter we detail the most important vehicle chassis control solutions in the automotive industry and academia, with a particular focus on those solutions that seek to stabilise the vehicle at the limits of handling. To this end, we first explore solutions that act on the lateral vehicle dynamics only and how these have evolved in the past thirty years before we divert our attention to more advanced solutions that interfere with the longitudinal dynamics of the vehicle in a controlled manner when a limit handling case is detected.

2.2 Active Lateral Dynamics Control

In the early limited commercial applications of active chassis control throughout the 1980s, 4WS with or without a semi-active/active suspension was the solution of choice [131]. However, the benefits of using such systems to improve the manoeuvrability and stability of the vehicle were outweighed by their high production and maintenance costs, making it difficult to justify them for mass production [84, 94]. Active brake systems on the other hand have remained under the full control of the ABS and the TCS for preventing wheel lock and spin, although early investigations on their use for active chassis control can be found in the literature [57].

The first time that an increased number of papers appeared in a conference session on the use of left-right tyre force distribution for control of the lateral dynamics of the vehicle was in AVEC '92 [48]. One paper of particular interest was that from Shibahata et al. [148], where the 'β-method' was first presented. While stability during cornering has been analysed before [118] the β-method demonstrated the importance of sideslip angle, especially when acceleration or braking is applied on the vehicle while cornering. Results from [148] showed that manoeuvrability of a vehicle is greatly influenced by its sideslip angle, with the possible yaw moment gain for different values of steering angle decreasing rapidly with increased sideslip angles. The β-method also graphically showed the 'shifting' of this yaw moment gain to higher values during acceleration creating understeer behaviour on a neutral base vehicle, while the opposite happens during deceleration. Shibahata et al. [148] also indicated that the yaw moment gain under steady-state cornering can be expressed as a function of longitudinal and lateral acceleration and thus, through the use of a hypothetical external yaw moment, the influence of acceleration and deceleration on the manoeuvrability of a vehicle can be eliminated. This method, called the Direct Yaw Control (DYC), was then applied on an AWD vehicle where this yaw mo-

ment was expressed as a distribution of the traction and braking forces on the rear wheels, while the front-rear distribution was kept constant. The simulation and experimental results showed the validity of the method and paved the road for the domination of the brake stability systems by the end of the 90s.

Three types of application of the DYC methodology on conventional vehicles have been so far the most popular [96]:

1. The lateral braking control using independent braking, so as to create a difference in braking forces between the left and right side of the vehicle hence generate a yaw moment.

2. The lateral torque distribution control which splits the engine torque to the left and right wheels, resulting in a difference in the driving torque between them hence a yaw moment generation.

3. The lateral torque vectoring control which is able to transfer torque from the left to the right wheel and vice versa, as to create a braking torque on one wheel while transferring the same amount as a driving torque to the opposite wheel.

While lateral braking control dominated the market by the late 90s, lateral torque distribution and torque vectoring systems quickly gained popularity mainly due to their less intrusive character in sub-limit conditions.

2.2.1 Lateral Braking Control

In this type of control, the use of the brakes for yaw moment generation means that control is effective across a wide range of vehicle operating conditions but can also create a negative feeling on the driver due to the deceleration of the vehicle [96]. Nevertheless,

lateral braking control is very effective during limit handling and is widely used in these situations since stability is more important than comfort in such cases [139].

Under this category we find the most successful so far active chassis control system in the automotive history: Bosch's ESP [90]. As Manning et al. [94] points out, while many theoretical papers on tyre force distribution quickly appeared after AVEC '92, the best practical application on yaw rate and sideslip control to date is the one presented by Bosch in 1995 [140]. In their original paper, Shibahata et al. [148] analysed the effect of a corrective moment on the dynamics of the vehicle across the full range of lateral acceleration. Bosch, focusing only on the limit handling cases, presented the concept of ESP in [140] pointing out that since vehicle instability at its handling limit is caused by the deteriorating effect of large sideslip angles on the yaw moment gain, it is necessary to control the sideslip angle along with the yaw motion of the vehicle [140, 141]. The ESP uses the existing hardware for ABS and TCS, but is distinctively different from these two systems: while both ABS and TCS operate at the tyre limit of adhesion having as controlled plant the individual wheels, the ESP system has the whole vehicle as the controlled plant and controls the wheels' slip in order to keep the vehicle motion close to the nominal one [141]. ESP achieves this using a hierarchical control structure: (i) the yaw rate target is set using a bicycle model and then saturated according to the tyre/road friction coefficient, while the sideslip angle target is set according to the β-method and then saturated according to the vehicle's speed [139, 141], (ii) this nominal vehicle behaviour is compared to the actual one, with the necessary yaw moment for minimization of the vehicle response error achieved through the distribution of braking forces on the individual tyres [139]. In its most basic form the ESP brakes the outer front wheel if an oversteer situation is detected and the inner rear wheel if an understeer situation is detected [52], the choice of the wheel accounting for the importance of lateral tyre force in the yaw moment generation.

Similar systems to Bosch's ESP can be found elsewhere in the automotive industry, with Ford [137], BMW [88] and Mando [80] being just a few of the examples. On the other hand, academia has mainly focused on the integration of a differential braking strategy with Active Front Steering (AFS) as to extend the operation of the system in the whole range of lateral acceleration. For example, in [13] we find a H_∞ controller that uses AFS and differential braking to achieve the yaw rate and sideslip angle targets, whereas the driver wheel steering angle command and sideslip angle and yaw rate references are modelled as disturbances. Other interesting examples are the differential braking strategy presented in [136] which uses a Sliding Mode Control (SMC) strategy for yaw and sideslip control while taking into account variations in the longitudinal dynamics, and [71] which uses differential braking and throttle control to manipulate the slipping condition of the rear tyres on an RWD vehicle according to the yaw rate target.

2.2.2 Lateral Torque Distribution and Torque Vectoring Control

While ESP is still the preferred stability control solution due to its quick and authoritative action and examples of coupling the braking system with AFS show that it is possible to extend its operation in the sub-limit region, placing the braking system at the centre of an integrated control system can have a deteriorating effect on the performance aspect of the vehicle as perceived by the driver [106, 127]. Due to this fact systems with lateral torque distribution have gained popularity in the late 90s and, although expensive to develop and produce, are still used today. In this type of control the possibility to freely portion the engine torque on the left and right wheels gives a way to generate a yaw moment to correct both understeer and oversteer situations under most operating conditions but has a clear disadvantage during cruising or deceleration where the engine torque is not large enough [96]. Under this category we mainly find active differentials that can regulate

the direction of torque to the left and right wheels under both limit and sub-limit conditions but cannot generate a corrective yaw moment when the engine input is zero [125]. The most successful example in this category is Honda's Active Torque Transfer System (ATTS) [132] as implemented for the first time on the driving axle of the FWD 1998 Honda Prelude Type SH, with the system showing improved stability and handling during combined steering and acceleration/deceleration commands [94].

In the case of torque vectoring control, torque can be transmitted between the wheels for yaw moment generation regardless of the engine input torque. It therefore does not conflict with the acceleration and braking commands from the driver, although it can have a negative effect on the steering action of the vehicle if it is applied on the front axle. The most characteristic example in this category is Mitsubishi's Active Yaw Control (AYC) system originally installed on the 1996 Mitsubishi Lancer Evolution IV along with its later variant, the Super AYC [138]. According to its basic principle of operation, torque vectoring is achieved by engaging the right or the left clutch of the torque vectoring differential, with the engagement of the clutches regulated by a feedforward-feedback controller: the feedforward path calculates the necessary yaw moment according to the wheel steering angle and throttle opening while the feedback path corrects this yaw moment request based on the left-right wheel speed difference [126].

2.2.3 Front-Rear and AWD Torque Distribution

With the increased popularity of the Sport Utility Vehicle (SUV) segment in the turn of the century, more research was conducted on the use of a front-rear distribution for active chassis control purposes. Front-rear distribution can change the understeer characteristics of the vehicle - Piyabongkarn [106, 107] showed that if torque is transferred from the front to the rear wheels of the vehicle, then oversteering is induced. However this method is not

as effective as left-right distribution: an early analysis from Motoyama [98] shows that front-rear has a lesser potential than left-right torque distribution in improving the turning characteristics of a vehicle. A good example of front-rear distribution is the paper series from Ricardo [144–146] on the development of a novel centre differential for use on an SUV. Here, a small electric motor is added for torque modulation in a centre differential configuration which makes possible to force a torque difference between the front and rear wheels. Experiments using the system on a BMW X5 showed mixed results [144] and Ricardo changed to a left-right differential device in the last paper of the series [146].

In the case of an AWD platform, distribution of the torque to all four wheels gives better traction when compared to an FWD or RWD solution and if the torque distribution is appropriately controlled, cornering performance can be improved without interfering with the acceleration/deceleration commands from the driver [127]. On the other hand, AWD solutions result in increased system complexity and production/maintenance costs which cannot be possibly justified in low cost vehicles, resulting in constraining such solutions on the higher segment vehicles, motorsport cars and off-road applications. The most characteristic example from this category is the Super Handling AWD (SH-AWD) system from Honda. SH-AWD was developed in the beginning of the century and was initially fitted on the 2004 LEGEND model, with later variants appearing in the 2006 RDX and MDX models amongst others [87]. The system combines a set of electromagnetic clutches (to vary the front-rear distribution) and an improved variant of the ATTS (to vary the left-right distribution) in a single unit at the rear axle. For the control unit a feedforward-feedback scheme is employed, whereas the feedforward path sets the front-rear and left-right torque distribution according to the yaw rate error and the driving conditions while the feedback path is used for correction in the event of excessive sideslip angle values [87]. Experimental results showed a less understeering behaviour from the vehicle when the SH-AWD system is used, but also that off-throttle it is not possible

anymore to transfer torque between the wheels.

2.2.4 The Electric Motor as a Chassis Control Device

While the refinement of the chassis control systems on conventional vehicles will continue in the foreseeable future, the parallel and rapid development of the EV and HEV platforms already presents some exciting new possibilities on the active chassis control front. The (H)EVs have attracted attention in the past two decades as a response to the ever-increasing fuel prices and growing environmental concerns [29]. For active chassis control purposes, the (H)EVs can eliminate the distinction between the different methodologies as documented above: braking, torque distribution and torque vectoring can be possibly achieved using only one type of actuator, the electric motor. In the sections to follow, after a brief introduction on the distinct advantages (and disadvantages) of the electric motor as an actuator for active chassis control purposes, we will focus on the different lateral vehicle dynamics control strategies using torque vectoring that have been investigated so far specifically on the EV and HEV platforms.

Most of the so far research on (H)EVs has concentrated on the energy management and powertrain technology challenges [29]. However, it has been also recognised that the electric motor has some distinct advantages over conventional drivelines as an actuator [59, 65]:

1. it has an extremely quick and accurate response and can be controlled according to a speed or torque demand,

2. its operation is reversible so it can be used as either a motor or a generator with almost equal efficiency, and

3. it can achieve high energy efficiency of up to 90%.

Furthermore, in the case of in-wheel motors the powertrain architecture is greatly simplified with less mechanical parts while new possibilities also open for the design of the passenger cell [120].

From the above we can conclude that when electric motors are used, an improvement on the vehicle handling characteristics can be achieved throughout the whole range of vehicle operation, encompassing functionalities like the ESP, ABS/TCS and torque vectoring. Furthermore, the behaviour of a vehicle can be directly 'designed' through the active control of the electric powertrain rather than indirectly tuned through changes in the mass distribution or the suspension characteristics. And while energy management for efficiency and vehicle dynamics management can be mistaken as two conflicting tasks, energy regeneration and consumption are directly associated with vehicle braking, suspension damping and vehicle sideslip angle, hence have a strong coupling with the control of the dynamics of the vehicle [32].

Despite the clear advantages of using an electric powertrain as documented above there are still some open questions which, along with the concerns on the use of a battery as the new energy storage device on a vehicle, can somehow explain the slow transition to (H)EV architectures. While the 'basic rules' of vehicle dynamics do not need to be re-invented [115], certain challenges arise when the powertrain is changed from a conventional Internal Combustion Engine (ICE) setup to an electric one with the most important being the increased sprung mass and packaging constraints (mainly related to the necessary inclusion of the battery) and the increased unsprung mass and suspension packaging (in the case of in-wheel motors). In view of these challenges, Crolla and Cao [32] looked into the impact of an EV architecture on the roll, pitch and yaw dynamics of a vehicle. Their investigations reveal that the increase in the sprung mass due to the extra load from the batteries can impact roll stability, ride vibration and comfort while the increase in the unsprung mass in the case of in-wheel motors makes the vertical wheel motion control

more challenging. Use of in-wheel motors may create further problems: (i) it can necessitate rethinking of the steering system and/or the suspension kinematics and packaging and (ii) it may yield a lower natural frequency for the unsprung mass, bringing it undesirably close to the frequency range that is most sensitive for the human body in the vertical direction (4-8Hz) [55]. On the other hand, in the case of HEVs Crolla and Cao [32] point out that the integration of an electric powertrain can create problems on the transient handling dynamics since these are strongly affected by the mass distribution and yaw moment of inertia of the vehicle. Use of regenerative braking may also be proved more limited than originally thought, with Crolla and Cao [32] showing that only a relatively small part of the total regeneration energy can be actually harvested back due to two limiting factors: (i) the actual process of regeneration is rather complicated - several aspects ranging from generator power to battery state of charge need to be considered in the process and (ii) the overall braking performance need to appropriately blend the regenerative braking with the existing hydraulic brake system, account for the brake feel from the driver and not disturb the handling balance of the vehicle (for example regenerating braking on the rear wheels if the driver lifts off during cornering can induce oversteer).

It is obvious from the above that there are both clear advantages and distinct disadvantages in the use of the electric motor as the main actuator in a electric powertrain. Both the automotive academia and industry have been actively looking at appropriate solutions, while government agencies have increased their initiative for research on the (H)EV architectures. But as Chan [29] has already pointed out, it will take the coordinated effort of not only government agencies and the automotive industry but also the electric industry to really establish the new platforms of HEVs and especially EVs as the primary choice of transportation for the average consumer.

2.2.5 Lateral Dynamics Control on EV and HEV Platforms

A large body of work exists on control of the lateral vehicle dynamics using torque vectoring on (H)EVs. One of the earliest examples is from Chong et al. [31] where some of the ideas introduced by Ackermann [3] for 4WS control are employed on an AWD EV, and a feedforward-feedback control law is developed so that the yaw rate and the sideslip angle of the vehicle are controlled through lateral torque vectoring on the front and rear tracks.

Examples of torque vectoring on an EV using two electric motors at the front or rear can be found in [119] where an SMC strategy is used with the driver steering input modelled as a disturbance, and in [149] where a Linear Quadratic Gaussian (LQG) controller is used to enhance steerability within a given yaw and sideslip control region or manoeuvrability outside it. Another example in [72] presents the investigations of Mitsubishi on the use of in-wheel motors for DYC. The authors attempt to match the characteristics of lateral dynamics from a high performance car using two electric motors on the rear track of the small test vehicle by employing classical control techniques and, while a good match is not achieved, the yaw rate and lateral acceleration response of the test vehicle show a noticeable improvement over the baseline vehicle.

In the case of AWD EVs one of the earlier investigations were presented from the Hori Laboratory in Tokyo University, where the previous work from the group on ABS and TCS implementations on an EV [59] is extended to yaw rate tracking [49,56,99,122]. Other examples of torque vectoring on AWD EVs can be found in [135] where a fuzzy logic controller is used and [147] where a control allocation strategy is employed instead. A very recent example from the industry is the 2013 Mercedes Benz AMG SLS Electric Drive vehicle where four motors are mounted on the chassis and final drives are used to connect them to the wheels in order to avoid the increase of the unsprung mass found in

an in-wheel motor solution [45]. Although no details on the specifics of the control strategy used are given, the authors claim that the vehicle can assume different behaviours depending on the setting from the driver ranging from understeering to oversteering setups. Regenerative braking is also coordinated with the ESP to achieve a good balance between energy regeneration and stability requirements.

A number of other drivetrain topologies and control methodologies can also be found in the literature, ranging from the integrated torque control of an rear electric motor and the electro-hydraulic brake system using a fuzzy logic controller in [79], to the use of an adaptive controller on a system with independent rear in-wheel motors and AFS [20, 99], to the use of autonomous corner modules where each wheel corner has its own set of steering and suspension actuators along with an in-wheel motor [68]. A rather unique drivetrain topology can be found in 'MUTE', an EV concept developed by the Technical University of Munich, where apart from the main electric motor a second smaller one is superimposed in the rear differential to obtain torque vectoring capabilities [58].

Studies on lateral vehicle dynamics control on Through-the-Road (TtR) HEVs can be found in the investigations from MIRA [105] and in [69, 91]. In [105] two electric motors are retrofitted at the back of the H4V test vehicle [30] and a Proportional-Integral-Derivative (PID) controller calculates the torque requests on the two rear axle electric motors for minimization of the yaw rate and sideslip angle errors from the target values which are set using a bicycle model. These torque requests are set equal in magnitude and opposite in sign so that no disturbance of the longitudinal dynamics is observed by the driver and are saturated for large sideslip angle and rates, large longitudinal slips on the wheels and according to the maximum motor power. Results show a significant reduction in the understeer gradient of the vehicle under steady-state cornering and increased manoeuvrability at the limit of adhesion, while relaxation of the maximum torque requests results in what the authors call a 'controlled drift': close to the limit of adhesion a

controlled oversteering was achieved using only steering commands from the driver.

A characteristic example on the development of a (H)EV platform using torque vectoring is the series of papers from the 7FP EU project *eFuture* [2]. The main goal of this project was to investigate the use of (H)EV platforms that minimise energy consumption but can also dynamically decide between energy efficiency and safety. Focusing on the vehicle dynamics aspect of the system, in [69] a feedforward-feedback controller structure is used to find the necessary torques on the four wheels according to the steering and driving/braking commands from the driver. For the feedback path, a PID controller with an LQG are separately used to calculate the necessary vehicle total longitudinal force and yaw moment respectively assuming decoupled longitudinal and lateral vehicle dynamics. Then a torque distribution unit is used to set the individual wheel torques in a manner similar to [105]: the ICE engine is responsible for delivering the longitudinal force command while the two electric motors on the rear axle take care of the yaw moment request. In [91] the previous control design is replaced by a polytopic Linear Parameter Varying (LPV) controller with scheduling parameters as functions of the longitudinal velocity, while an anti-windup scheme is employed in the feedback path to avoid actuator saturation. Results show much better reference tracking performance when compared to the previous PID-LQG design [69] and good disturbance rejection. The last two papers [12, 70] continue on the same control design, but this time using a pure EV architecture instead (FWD with two electric motors). In [70] the LPV controller presented in [91] is modified by including yaw rate in the scheduling parameters, while the anti-windup scheme is extended to a torque and slip limiter. In [12], a further refinement is achieved by using parameter-dependent Lyapunov functions and shaping filters in the controller synthesis. The outcome is slightly better simulation results with smaller torque inputs when compared to [70] but at the expense of greater computational effort.

A more pragmatic approach can be found in the series of papers from the 7FP EU

project *E-VECTOORC* [1], where a control allocation scheme is employed for torque vectoring of the four electric motors of a pure EV. Control allocation, a method widely used in robotics, aerospace and marine applications for control of overactuated systems, has lately become popular in the area of vehicle dynamics control. This is especially apparent in research related to (H)EVs, two architectures which can easily result in an overactuated system when more than two electric motors are used or the electric drivetrain is combined with other actuators like an AFS system. Control allocation has some very attractive features for this type of applications because it can [67]:

- meet fault tolerance and control reconfiguration requirements,
- distribute effectors to different control systems to serve different objectives,
- separate fast actuators from slower ones,
- offer the opportunity to introduce secondary objectives like minimization of power consumption.

The main aim of the *E-VECTOORC* project was to develop a torque vectoring strategy that enhances the fun-to-drive factor of the vehicle while improving energy efficiency, along with novel strategies on torque modulation for brake energy recuperation, ABS and TCS functionality [1]. Based on these criteria, research in [63] focuses on the derivation and evaluation of an appropriate cost function for control of the vehicle dynamics, while [33, 62] present initial results of the set control targets and the control allocation strategy used to achieve them. The following requirements are set for the target vehicle behaviour [33, 62]: (i) reduction of the understeer gradient in the linear part of the understeer characteristic under constant velocity, (ii) extension of the area of linearity of the understeer characteristic, (iii) increase of the maximum achievable lateral acceleration and (iv) reduction of the variation of the understeer characteristic with longitudinal

acceleration. The resulting reference understeer characteristic is therefore set as a function of both longitudinal and lateral accelerations [62]. Focusing on the control allocation problem, Novellis et al. [33] use an off-line optimization algorithm for evaluation of different control allocation cost functions employing a quasi-static vehicle model and a motor modelled as a simple first order delay. A range of different cost functions based on performance and power usage criteria is presented for evaluation, for minimization of the input power, the tyre force coefficient, the longitudinal slip loss or the slip standard deviation. Comparisons between the different cost functions showed amongst others a strong correlation between the input power and the reference understeer characteristic, emphasising the benefits of setting a less understeer target not only for stability but also energy consumption reasons. The authors conclude that slip-based cost functions are highly recommended for control allocation of the wheel torques in EV applications. Finally, in [101] the yaw rate controller presented in the previous papers is extended by an additional sideslip angle control strategy which activates a sideslip-based yaw moment contribution when the sideslip angle value exceeds a pre-defined threshold.

2.3 Active Longitudinal Dynamics Control

Up to this day, the control of the longitudinal dynamics of the vehicle has largely remained under the full authority of the driver, and active longitudinal control of the vehicle has been restricted in systems such as the CC for comfort reasons and in autonomous vehicle control applications. On the other hand, braking systems for DYC that can decelerate the vehicle are still viewed as deteriorating on the driving experience [96, 106, 126].

While it is true that the driver should remain at the centre of the longitudinal vehicle dynamics control, it has been also recognised that active control of the longitudinal dynamics can have a positive impact on stability in limit handing situations [53,89,106,139].

The key idea is that terminal understeer arising from overspeeding in a curve cannot be corrected by means of lateral control only, since there is a integral connection between the velocity of a vehicle and the minimum radius it can achieve through its maximum feasible lateral acceleration. One of the earliest examples that explores this idea can be found in [86], where the authors notice that the combined action of a corrective yaw moment and deceleration through appropriate brake control of the four wheels improves stability and path tracking. In ICE vehicles, a stability system that actively changes the longitudinal dynamics to account for this fact is already mentioned by van Zanten et al. [139]. This early remark on the importance of longitudinal control was later realised as one of the ESP new functions [89]: the Enhanced Understeering Control (EUC) function attempts to correct terminal understeer by superimposing individual braking of all four wheels on the standard ESP intervention. The target velocity is set as a function of the intended path radius, which in turn is set according to the steering input from the driver. Experimental results on a middle segment vehicle show an improvement in road holding with reduced curve radius of 12% when the EUC function is used so that, as the authors mention, the driver is able to keep the intended vehicle path and possibly avoid an accident [89].

The use of longitudinal control for terminal understeer correction was also studied in [53], where a direct comparison between a yaw control system and a simple velocity controller using braking only was performed in both simulation and experiment. The authors conclude that for off-tracking minimisation as is the case in terminal understeer, an early reduction in vehicle's speed is more efficient than increasing its yaw rate. More recently, Rajamani and Piyabongkarn [114] came into similar conclusions while looking into the concept of speed reduction for rollover mitigation based on an earlier remark from the same authors [106]: it was noticed that since the rollover propensity of a vehicle can be expressed by its dynamic Rollover Index (RI) which is a function of both the roll angle and the lateral acceleration, appropriate reduction of the latter by decreasing the

vehicle's velocity can prevent rollover. Rajamani and Piyabongkarn [114] conclude that reducing the vehicle's speed before entering a sharp curved road provides better cornering performance compared to the typical yaw rate control.

An example that focuses on oversteer correction instead using longitudinal dynamics control can be found in [82], which documents the investigations of Honda on this matter. Assuming decoupled longitudinal and lateral dynamics the authors attempt to achieve both the stability (i.e. correcting oversteer of the vehicle) and steerability (i.e. allow faster yaw rate response to steering inputs) targets by using braking of the appropriate wheels. While oversteer correction is achieved using braking of the front outside wheel as per basic ESP functionality, the rear tyres are braked as well to recover the front tyre grip and improve steerability. Results comparing the system against a yaw rate controller in a slalom and a J-turn manoeuvre on a snow packed road show a faster tracking of the yaw rate target with lower sideslip angle values and smoother steering angle inputs from the driver.

For AWD EVs, in [81] regulation of vehicle's velocity is achieved as part of a DYC method, whereas the torque request from the driver is reduced when the lateral acceleration exceeds a specified threshold which is set as a function of steering input under kinematic cornering conditions. Another implementation example on an AWD EV can be found in [85], where a velocity limit is set as a function of the desired yaw rate and turning radius of the car, the latter calculated by the current estimates on velocity and yaw rate of the vehicle. While both papers use simplifications in the controller synthesis, like assuming decoupled longitudinal and lateral dynamics, neglecting the load transfer effects and superimposing the torque requests for velocity reduction to the torque distribution as calculated by the yaw rate controller, they show that implementation of the idea on an EV can be straightforward since longitudinal control is an inherent part of the vehicle control problem in such architectures.

A more interesting EV implementation of active longitudinal dynamics control can be found in [74]. Here, a torque vectoring control algorithm which utilises a static control allocation scheme on an AWD EV is presented. The system is equipped with a front in-line motor and rear twin in-wheel motors with regenerative capabilities along with independent wheel braking control, and extends on the work by the same authors in [75], where two in-line motors were used instead. The purpose of the proposed system is to minimise the vehicle's path and yaw rate error using yaw rate and velocity control, and is constructed in three layers, namely a supervisory controller, an upper-level controller, and an optimal torque vectoring algorithm. The supervisory controller is responsible for computing the desired vehicle velocity and yaw rate, and for selecting the appropriate control mode: yaw rate control is enabled after a given threshold is passed, whereas speed control is enabled if the path requested from the driver, expressed by its curvature, is too tight. The latter is judged according to an admissible control region found by superimposing curvature constraints according to the maximum steering angle, a sideslip angle limit and the RI of the vehicle. Then, if the desired speed and curvature combination as requested by the driver falls outside the admissible control region, the supervisory controller enables the speed control mode and thus takes full control of the vehicle's speed over the driver. Having obtained the desired vehicle velocity and yaw rate from the supervisory controller, the upper level controller then finds the necessary traction force and yaw moment to meet these requests using an SMC strategy. Finally the distribution of the driving/braking torques on the four wheels is found using a static control allocation scheme: the optimization problem is formulated as a weighted least-squares problem which seeks to minimise the control allocation error, maximise the energy dissipation of the system, and minimise the slip control error (a slip controller is activated when the slip ratio of a wheel exceeds a given limit), subject to the motor and tyre force limits. Simulation results comparing the derived torque vectoring controller against a baseline vehicle

with no stability control and a vehicle equipped with a similar controller but using an unconstrained optimization method instead show that the proposed controller can achieve good path following with lower steering inputs from the driver. In conclusion, the torque vectoring control algorithm detailed in [74] exhibits some nice features like the use of a rollover constraint in the calculation of the desired vehicle velocity and the inclusion of regenerative braking in the optimization problem. However, it assumes decoupled longitudinal and lateral vehicle dynamics and neglects the inevitable tyre forces nonlinearities in limit handling. Furthermore, while the modular structure presented encourages the use of a linear model in the high-level controller which does not need details of the specific vehicle configuration, careful consideration is needed if infeasible control targets are to be avoided.

2.4 Conclusions

From the above literature review we can conclude that although the problem of stabilising the vehicle at the limits of handling has been addressed before, all the so far proposed strategies rely on simplifying assumptions such as decoupled longitudinal and lateral vehicle dynamics and/or linear tyre models. While this approach has been proven to be an effective control design methodology in the sub-limit cases, resulting in simpler control strategies that can be easily tuned and deployed, it is not as effective when it is applied to limit handling cases where the strong coupling effects and the nonlinear tyre characteristics become important. Furthermore, the necessity to regulate the vehicle velocity in terminal understeer behaviour cases results in an even more demanding problem to be solved, which asks for more tuning effort with questionable results if such simplifying assumptions are used.

Based on these observations, in this project we present a real-time implementable mul-

tivariable control strategy to stabilise an RWD EV at the limits of handling in an optimal way using combined longitudinal and lateral dynamics control. We show the importance of accounting for the nonlinear tyre characteristics and coupled longitudinal and lateral vehicle dynamics and tyre forces under such cases. We also show that accounting for the system and actuator limits results in better control actions and ultimately a better control strategy with less tuning effort. Finally we show that, thanks to the huge leaps in computational power and memory storage in the past 20 years along with the introduction of new optimisation algorithms and the continuous improvement of existing ones, advanced optimal control strategies can be now successfully applied on such complicated problems in real-time.

Chapter 3

Vehicle Model and Reference Generation

3.1 Introduction

In this chapter we introduce the vehicle and tyre models used in the development of the optimal control strategies in this project, along with the methodology for generating the reference vehicle state for the controllers to follow.

The structure of this chapter is as follows: after introducing the four-wheel vehicle model and the simplifying assumptions used in its derivation, the basic principles of the tyre force generation are explained along with the tyre model used, followed by the steady-state cornering analysis and the methodology used to find the equilibrium state to be used as the reference vehicle behaviour for the controller to follow.

3.2 The Vehicle Model

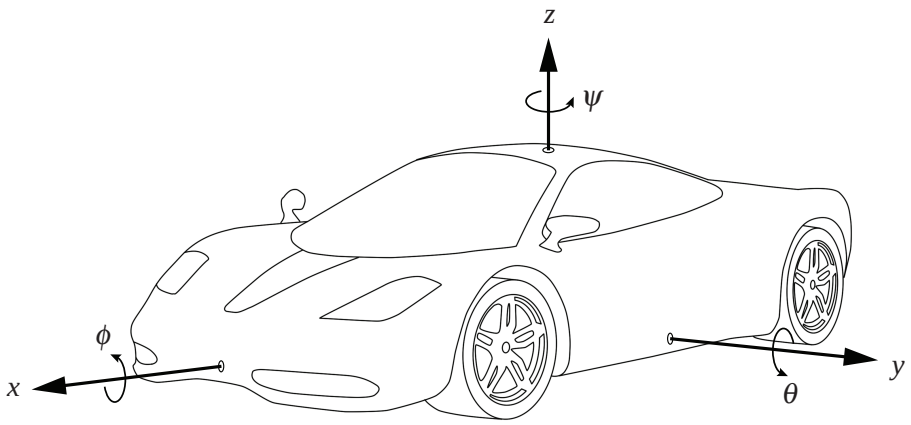

Figure 3.1: Vehicle coordinate frame.

A seven Degrees of Freedom (DOF) vehicle model is used in this work, with its Equations of Motion (EOM) expressed in a coordinate frame attached to its CM as in Fig. 3.1. As it is usual in the modelling of the vehicle dynamics for control design purposes, certain assumptions are made at this point to reduce the model complexity [104]. We therefore neglect:

- the Ackerman Principle (both front wheels will steer with the same angle),
- the rolling resistance, aligning moment and camber angle of the tyres,
- the suspension dynamics,
- the pitch and roll motion of the vehicle,
- the characteristics of the transmission and brake systems,
- the aerodynamic forces on the vehicle.

Then the EOM for the four-wheel vehicle model can be derived using Newton's 2nd Law in the longitudinal and lateral direction on the vehicle local frame:

$$ma_x = \sum f_x,$$
$$ma_y = \sum f_y,$$

where a_x and a_y can be expressed in terms of the velocity vector components V_x and V_y using the translational part of the Newton-Euler equations [66]:

$$a_x = \dot{V}_x - \dot{\psi} V_y, \tag{3.1a}$$
$$a_y = \dot{V}_y + \dot{\psi} V_x. \tag{3.1b}$$

It follows that, by also including the rotational part of the Newton-Euler equations [66] and the angular rate dynamics of the four wheels, the EOM for the four-wheel vehicle model are

$$\begin{aligned} m\dot{V} &= (f_{FL_x} + f_{FR_x})\cos(\delta-\beta) - (f_{FL_y} + f_{FR_y})\sin(\delta-\beta) \\ &\quad + (f_{RL_x} + f_{RR_x})\cos\beta + (f_{RL_y} + f_{RR_y})\sin\beta, \qquad (3.2a) \\ \dot{\beta} &= \frac{1}{mV}\Big[(f_{FL_x} + f_{FR_x})\sin(\delta-\beta) + (f_{FL_y} + f_{FR_y})\cos(\delta-\beta) \\ &\quad - (f_{RL_x} + f_{RR_x})\sin\beta + (f_{RL_y} + f_{RR_y})\cos\beta\Big] - \dot{\psi}, \qquad (3.2b) \\ I_z\ddot{\psi} &= \ell_F\Big[(f_{FL_y} + f_{FR_y})\cos\delta + (f_{FL_x} + f_{FR_x})\sin\delta\Big] \\ &\quad - \ell_R(f_{RL_y} + f_{RR_y}) + w_L(f_{FL_y}\sin\delta - f_{FL_x}\cos\delta - f_{RL_x}) \\ &\quad + w_R(f_{FR_x}\cos\delta - f_{FR_y}\sin\delta + f_{RR_x}), \qquad (3.2c) \\ I_w\dot{\omega}_{ij} &= T_{ij} - f_{ijx}R_w, \qquad i = F,R,\ j = L,R, \qquad (3.2d) \end{aligned}$$

where I_z is the vehicle's moment of inertia about the vertical axis, m the vehicle's mass, V is the vehicle velocity, $\dot{\psi}$ the yaw rate and β the sideslip angle at the CM. The radius of each wheel is R_w, its moment of inertia about its axis of rotation is I_w, and its angular rate (or more commonly speed) is ω_{ij} $(i = F\,(\text{front}), R\,(\text{rear}),\ j = L\,(\text{left}), R\,(\text{right}))$. The steering angle for both the front wheels is δ, and the driving/brake torques applied on the wheels T_{ij}. The longitudinal and lateral tyre forces are denoted by f_{ijk} ($i = F, R$, $j = L, R$ and $k = x, y$). Finally the distances ℓ_F, ℓ_R, w_L and w_R determine the location of the centre of each wheel with respect to the CM (Fig. 3.2).

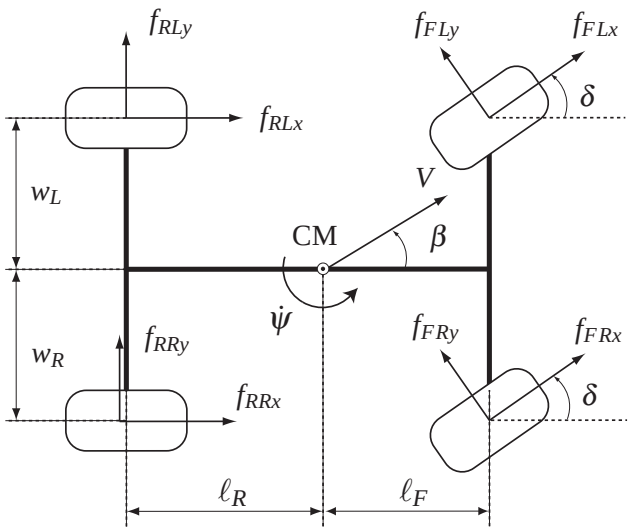

Figure 3.2: Four-wheel vehicle model [134].

3.2.1 Longitudinal and Lateral Tyre Forces and Velocities

The tyre forces f_{ijk} in (3.2) are calculated as functions of tyre slip using Pacejka's Magic Formula (MF) [10]. Tyre slip refers to the non-dimensional relative velocity of the tyre

with respect to the road. The theoretical slip quantities are defined as [10]:

$$s_{ijx} = \frac{V_{ijx} - \omega_{ij} R_w}{\omega_{ij} R_w}, \qquad s_{ijy} = \frac{V_{ijy}}{\omega_{ij} R_w}, \tag{3.3}$$

where V_{ijk} $(i = F,R,\ j = L,R,\ k = x,y)$ are the tyre frame components of the vehicle velocity vector at the centres of the four wheels. These tyre frame velocities are the result of the combined effect of the translational motion of the wheel due to V plus its rotational motion about the CM due to $\dot{\psi}$. For example, the tyre frame velocity component V_{FLx} at the centre of the front-left wheel is

$$V_{FLx} = V\cos(\delta - \beta) - \dot{\psi} l_{FL} \sin(\gamma_{FL} - \delta),$$

where $\ell_{FL} = \sqrt{\ell_F + w_L}$ is the distance of the centre of the front-left wheel from the CM and $\gamma_{FL} = \tan^{-1}(w_L/\ell_F)$ the corresponding angle with respect to the vehicle's y-axis (Fig. 3.2).

Similarly the remaining tyres' velocity components can be derived, with the complete set being

$$V_{FLx} = V\cos(\delta - \beta) - \dot{\psi}\ell_{FL}\sin(\gamma_{FL} - \delta), \quad V_{FLy} = -V\sin(\delta - \beta) - \dot{\psi}\ell_{FL}\cos(\gamma_{FL} - \delta),$$
$$V_{FRx} = V\cos(\delta - \beta) + \dot{\psi}\ell_{FR}\sin(\gamma_{FL} + \delta), \quad V_{FRy} = -V\sin(\delta - \beta) + \dot{\psi}\ell_{FR}\cos(\gamma_{FL} + \delta),$$
$$V_{RLx} = V\cos\beta - \dot{\psi}\ell_{RL}\sin\gamma_{RL}, \qquad V_{RLy} = V\sin\beta - \dot{\psi}\ell_{RL}\cos\gamma_{RL},$$
$$V_{RRx} = V\cos\beta + \dot{\psi}\ell_{RR}\sin\gamma_{RR}, \qquad V_{RRy} = V\sin\beta - \dot{\psi}\ell_{RR}\cos\gamma_{RR}.$$

3.2.2 Longitudinal and Lateral Tyre Slip

The longitudinal slip on a tyre s_{ijx} as given in (3.3) accounts for the fact that when a moment is applied on a wheel, a difference appears between the actual speed of the tyre

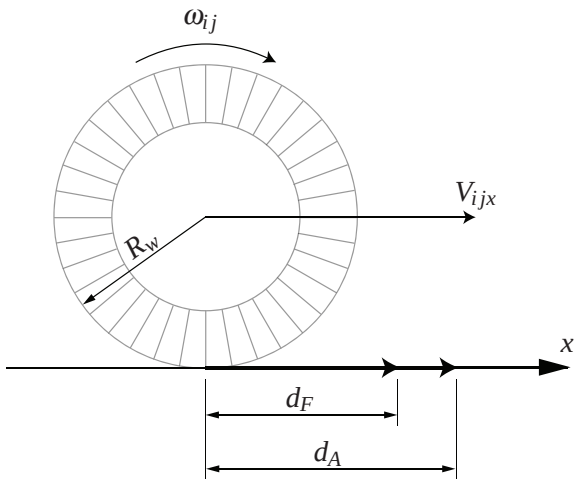

Figure 3.3: No slip travel distance d_F compared to actual travel distance d_A.

V_{ijx} and its equivalent speed $\omega_{ijx}R_w$. The appearance of longitudinal slip is the main factor for the creation of a longitudinal force f_{ijx} on the tyre [66] and as we can see from Fig. 3.3, the wheel will travel a larger distance d_A under longitudinal slip when compared to the free-rolling case d_F. While different approaches have been suggested for the calculation of s_{ijx} [10, 39, 121] in this work we employ the above definition (3.3) according to [10].

The lateral slip s_{ijy} as given in (3.3) accounts for the fact that when a vehicle is steered, a slip angle α_{ij} appears on the tyre which results in the development of a lateral force f_{ijy}, hence the vehicle turns towards its intended direction. The tyre slip angle and the lateral force work as 'action and reaction' [66], with a negative α_{ij} resulting in a positive f_{ijy}. For example in the case of a single tyre steered by a positive steering angle δ to the left as seen in Fig. 3.4, a negative tyre slip angle appears and subsequently a positive lateral force is created to move the vehicle to the left. It follows that the resultant slip on a tyre is defined as:

$$s_{ij} = \sqrt{s_{ijx}^2 + s_{ijy}^2}. \tag{3.4}$$

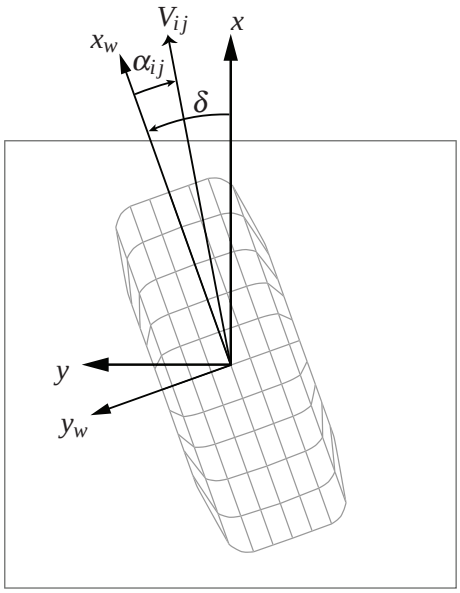

Figure 3.4: Angular orientation of a moving tyre at a slip angle α_{ij} and a steer angle δ.

3.2.3 Friction Coefficient

Assuming that the friction coefficient μ between the tyre and the road is independent of the vertical force on the tyre f_{ijz}, it together with the vertical force gives the total force on the tyre:

$$f_{ij} = \mu f_{ijz}. \tag{3.5}$$

The friction generated between the tyre and the road is the result of their very complex interaction and arises due to following three main factors [66]:

1. The adhesion friction: results from the tyre 'sticking' on the road thus creating and breaking molecular bonds with it continuously. It is the main contributor under dry road conditions.

2. The deformation friction: results from the tyre's tread penetration in the road's

irregularities. It is the main contributor under wet road conditions.

3. The wear friction: results from deformation of the tyre past its elastic limit due to high localised stresses.

The combination of the above friction mechanisms gives the tyre force as a function of the tyre's load and the road conditions according to (3.5), with the peak values for the tyre/road friction coefficient μ_{max} set according to Table 3.1.

Road surface	μ_{max}
Asphalt, dry	$0.8 - 1.0$
Asphalt, wet	$0.5 - 0.7$
Snow, packed	0.2
Ice	0.1

Table 3.1: Typical variation of μ_{max} with road surface condition.

3.2.4 Tyre Modelling

One of the most important aspects in the study of vehicle dynamics is the tyre model, since it provides a way to calculate the tyre forces as functions of the observed slip quantities, while its accuracy is decisive in reliable vehicle simulations. Although direct use of tyre data in tables and graphs is possible these two methods are difficult to implement in a theoretical study, hence different formulae have been suggested throughout the years [133]. As noticed by Pacejka and Besselink [104] exponential, arctangent, parabolic hyperbolic tangent functions have been tried with more and less success, while higher order polynomials have also been used but proved to be inaccurate outside the original tyre measurement data.

Three of the most popular tyre models used in the study of vehicle dynamics are the Fiala, the Dugoff and the Pacejka model [113]. The elastic foundation analytical tyre

B_{MF}	stiffness factor	E_{MF}	curvature shift
C_{MF}	shape factor	S_h	horizontal shift
D_{MF}	peak value	S_v	vertical shift

Table 3.2: MF's parameters.

model developed by Fiala in 1954 focuses on the lateral force generation only, assuming that the contact patch can be divided into small elements with individual foundation stiffness springs that try to restore the elements to their original position. An alternative analytical model is Dugoff's model which was developed in the late 60s from force balance calculations and takes into account the longitudinal-lateral tyre force generation. According to Rajamani [113] both Fiala's and Dugoff's models are physically intuitive but can give inaccurate results, especially at large and/or combined longitudinal-lateral slip. An alternative approach is to use an empirical expression as the one found in Pacejka's MF [10]. The MF is capable of describing the tyre longitudinal and lateral force, along with its self aligning torque with good accuracy and, although it is normally validated only under steady-state conditions during either pure braking or pure cornering, it is widely used in dynamic simulations of vehicle models under combined longitudinal-lateral slip conditions.

According to the MF, in the case when only a lateral or a longitudinal force is generated on the tyre the output variable Y can be expressed as a function of the input variable X as follows [113]:

$$y = D_{MF} \sin\left[C_{MF} \tan^{-1}\left(B_{MF}x - E_{MF}\left(B_{MF}x - \tan^{-1}\left(B_{MF}x\right)\right)\right)\right], \tag{3.6}$$

with $Y(X) = y(x) + S_v$ and $x = X - S_h$. The output variable Y can be the longitudinal or the lateral tyre force as a function of the input variable X, which can be the longitudinal slip or the slip angle respectively. The parameters B_{MF}, C_{MF}, D_{MF}, E_{MF}, S_v, and S_h (Table

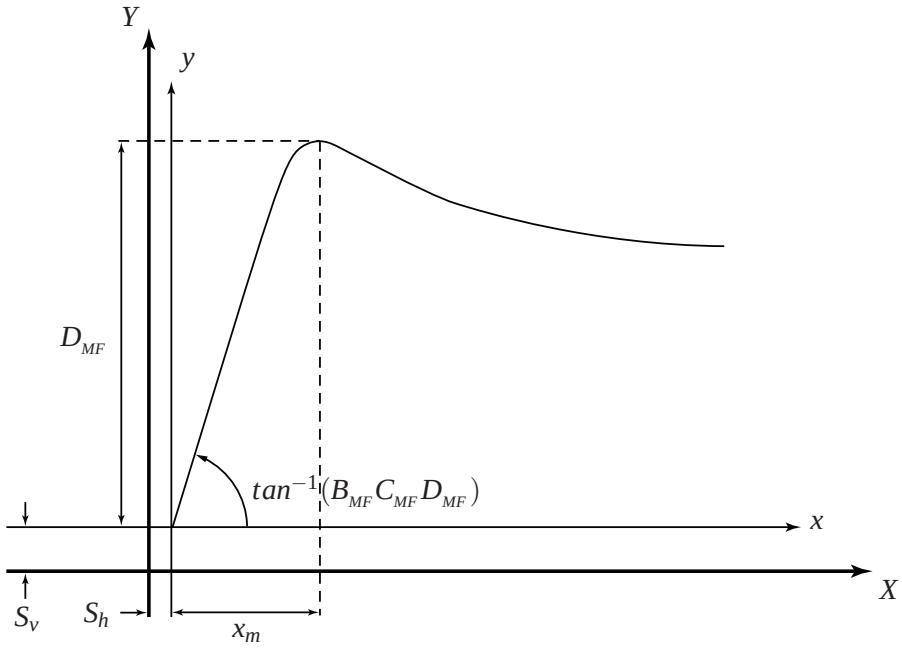

Figure 3.5: MF curve and parameters.

3.2) are identified experimentally and define the shape of the curve as seen in Fig. 3.5.

A simplified version of the MF which neglects the shift factors S_h and S_v as well as the curvature factor E_{MF} is [10]:

$$y = D_{MF}\sin(C_{MF}\tan^{-1}(B_{MF}x)). \tag{3.7}$$

The omission of the shift factors as well as the curvature factor does not change the important features of the MF: D_{MF} is still the peak value, B_{MF} is still the stiffness factor, C_{MF} still governs the shape of the curve, while the product $B_{MF}C_{MF}D_{MF}$ still corresponds to the slope at the origin ($x = y = 0$) of the curve [133].

From (3.7) and Fig. 3.5 we can draw some useful conclusions. For example, in the case of pure acceleration or braking so that only a longitudinal force exists on the tyre we can analyse the longitudinal force and slip relationship by splitting Fig. 3.5 into two distinct regions:

1. Linear region: the longitudinal force increases linearly with longitudinal slip for a small range of values up to x_m close to the origin, with the slope of the curve at this region estimated using the product $B_{MF}C_{MF}D_{MF}$. Shortly after this linear region, the longitudinal force reaches a peak which is equal to the maximum possible longitudinal force.

2. Nonlinear region: After the maximum peak, the longitudinal force drops to an almost constant value. Hence the peak represents not only the maximum longitudinal force but also the point where the tyre starts locking in the case of braking or spinning in the case of acceleration.

Similar conclusions can be drawn for the lateral tyre force in the case of pure cornering.

3.2.5 Friction Circle

A tyre under both longitudinal and lateral slip is under a combined slip state, with the resultant friction force on the tyreprint being [66]

$$f_{ij} = \sqrt{f_{ijx}^2 + f_{ijy}^2}.$$

The longitudinal and lateral tyre forces cannot exceed their maximum values $f_{ijx_{max}}$ and $f_{ijy_{max}}$ as already indicated in section 3.2.4. Then the tip point of the maximum resultant force f_{ij} is always on the friction ellipse:

$$\left(\frac{f_{ijx}}{f_{ijx_{max}}}\right)^2 + \left(\frac{f_{ijy}}{f_{ijy_{max}}}\right)^2 = 1.$$

Assuming also a homogeneous tyre with symmetric characteristics in the longitudinal and lateral directions the friction ellipse becomes a circle. The friction circle is an im-

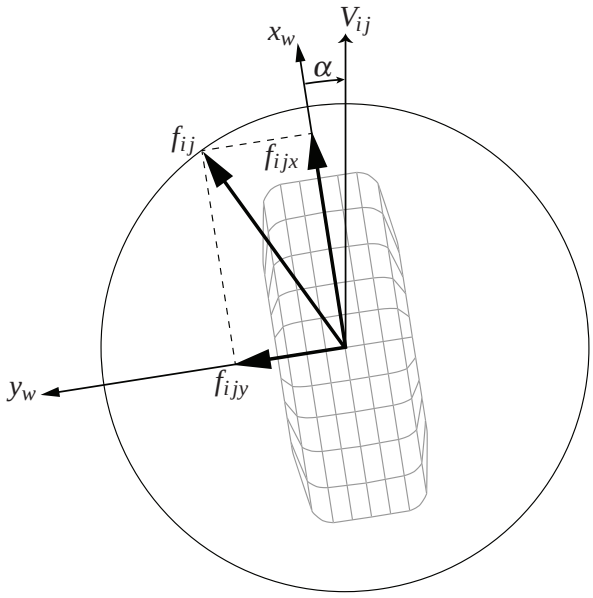

Figure 3.6: Friction circle.

portant concept that emphasises the connection between the longitudinal and lateral tyre force, especially as we approach the limit of adhesion. From Fig. 3.6 we can see that for a specific longitudinal force, the maximum resultant force can only reach the peak value specified by the friction circle so that the lateral force cannot exceed a limiting value.

Using the friction circle we can finally find f_{ijx} and f_{ijy} when the tyre is under a combined slip state. After calculating the total friction coefficient as a function of total slip using the simplified MF (3.7)

$$\mu_{ij} = \mathrm{MF(s)} = D_{MF} \sin(C_{MF} \tan^{-1}(B_{MF} s_{ij})), \tag{3.8}$$

we can derive the longitudinal and lateral tyre friction components using [10]

$$\mu_{ijx} = -\frac{s_{ijx}}{s_{ij}} \mu_{ij}, \qquad \mu_{ijy} = -\frac{s_{ijy}}{s_{ij}} \mu_{ij}, \tag{3.9}$$

and from these expressions f_{ijx} and f_{ijy} can be found from

$$f_{ijx} = \mu_{ijx} f_{ijz}, \qquad f_{ijy} = \mu_{ijy} f_{ijz}, \tag{3.10}$$

if f_{ijz} is known. Notice that the minus signs in (3.9) account for the fact that friction always resists the relative motion of the tyre on the road.

3.2.6 Vertical Tyre Forces

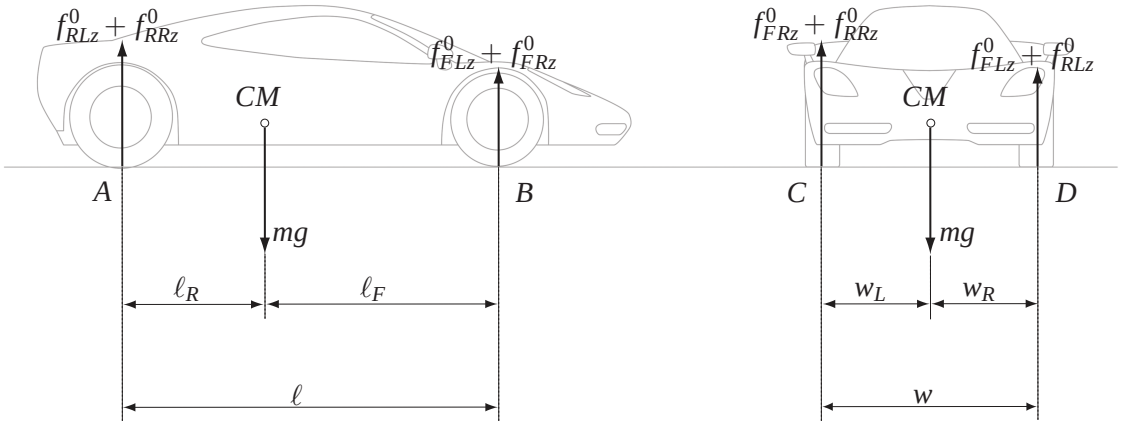

Figure 3.7: Static load distribution.

The total vertical force (or normal load) on a tyre of a moving vehicle can be expressed as a function of the static load on that tyre plus the dynamic loads due to longitudinal and lateral acceleration. It follows that:

$$f_{FLz} = f^0_{FLz} - \Delta f^x_L - \Delta f^y_F, \qquad f_{FRz} = f^0_{FRz} - \Delta f^x_R + \Delta f^y_F,$$
$$f_{RLz} = f^0_{RLz} + \Delta f^x_L - \Delta f^y_R, \qquad f_{RRz} = f^0_{RRz} + \Delta f^x_R + \Delta f^y_R,$$

where f^0_{ijz} are the static load components on each tyre and Δf^x_j, Δf^y_i account for the dynamic loads due to a_x and a_y respectively. For the derivation of f^0_{ijz} and Δf^x_j, Δf^y_i we

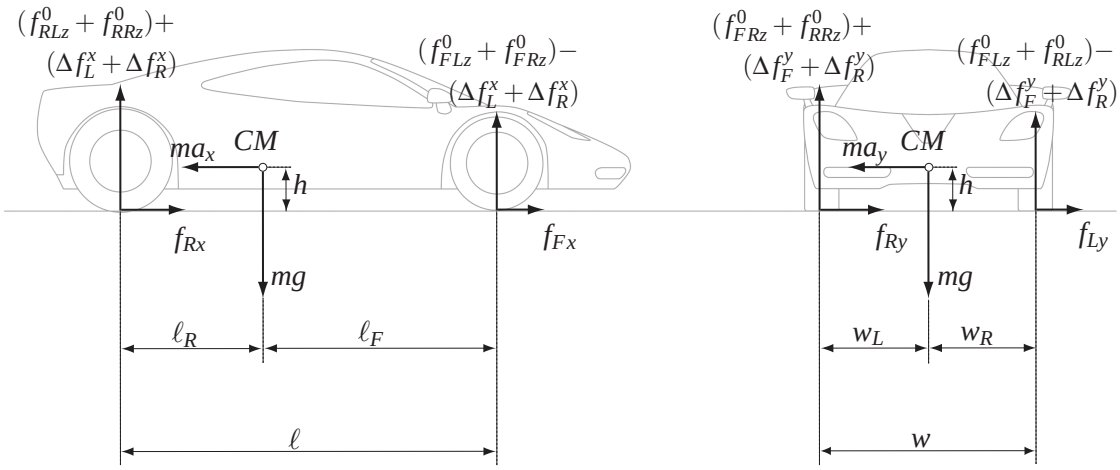

Figure 3.8: Dynamic loads due to a_x and a_y.

can use a simple moment analysis, as seen in Figs. 3.7-3.8.

From Fig. 3.7 and taking moments about points A,B and C,D under zero longitudinal and lateral acceleration we can show that:

$$f^0_{FLz}=\frac{mg\ell_R w_R}{(\ell_F+\ell_R)(w_L+w_R)}, \qquad f^0_{FRz}=\frac{mg\ell_R w_L}{(\ell_F+\ell_R)(w_L+w_R)},$$
$$f^0_{RLz}=\frac{mg\ell_F w_R}{(\ell_F+\ell_R)(w_L+w_R)}, \qquad f^0_{RRz}=\frac{mg\ell_F w_L}{(\ell_F+\ell_R)(w_L+w_R)}.$$

Similarly, from Fig. 3.8 and using the static load components f^0_{ijz} from above, we can find Δf^x_j and Δf^y_i as functions of a_x and a_y:

$$\Delta f^x_L=\frac{mhw_R}{(\ell_F+\ell_R)(w_L+w_R)}a_x, \qquad \Delta f^x_R=\frac{mhw_L}{(\ell_F+\ell_R)(w_L+w_R)}a_x,$$
$$\Delta f^y_F=\frac{mh\ell_R}{(\ell_F+\ell_R)(w_L+w_R)}a_y, \qquad \Delta f^y_R=\frac{mh\ell_F}{(\ell_F+\ell_R)(w_L+w_R)}a_y.$$

The analytical expressions derived above give a good match to experimental data [78] and will be used for the reminder of the text.

3.3 Reference Generation

3.3.1 Steady-State Cornering Analysis

In order to obtain feasible targets for the controller to follow a steady-state cornering analysis of the four-wheel vehicle model (3.2) is performed in a way similar to [40]. We therefore consider the nonlinear tyre characteristics and the coupled longitudinal and lateral vehicle dynamics and tyre forces to derive realistic reference steady-state cornering conditions specific to the given drivetrain topology.

Steady-state cornering is characterised by a trajectory of constant radius $R = R^{\text{ss}}$, negotiated at a constant speed $V = V^{\text{ss}}$, constant yaw rate $\dot{\psi} = \dot{\psi}^{\text{ss}} = V^{\text{ss}}/R^{\text{ss}}$ and constant sideslip angle $\beta = \beta^{\text{ss}}$. Since, according to the chosen drivetrain topology, only actuation of the rear wheels is used we set free rolling conditions on the front wheels,

$$s_{Fjx} = 0, \qquad f_{Fjx} = 0, \qquad j = L, R,$$

and also neglecting the wheel speed dynamics (3.2d), the four-wheel vehicle model (3.2) can be written as

$$\dot{V} = f_1(V, \beta, \dot{\psi}, \delta, s_{RLx}, s_{RRx}), \tag{3.11a}$$

$$\dot{\beta} = f_2(V, \beta, \dot{\psi}, \delta, s_{RLx}, s_{RRx}), \tag{3.11b}$$

$$\ddot{\psi} = f_3(V, \beta, \dot{\psi}, \delta, s_{RLx}, s_{RRx}), \tag{3.11c}$$

where the vehicle dynamics are expressed as functions of the reduced state $(V,\ \beta,\ \dot{\psi})$ and the new input $(\delta^{\text{ss}},\ s_{RLx}^{\text{ss}},\ s_{RRx}^{\text{ss}})$, with the necessary rear axle lateral slips found as functions of the corresponding longitudinal and lateral tyre velocities along with the corresponding

longitudinal slip:

$$s_{Rjy} = (1 + s_{Rjx})\frac{V_{Rjy}}{V_{Rjx}}, \qquad j = L, R.$$

Then enforcing the steady-state cornering conditions:

$$\dot{V} = 0, \qquad \dot{\beta} = 0, \qquad \ddot{\psi} = 0,$$

the above system (3.11) reduces to a set of three algebraic equations with six unknowns, namely the equilibrium state $(V^{\text{ss}},\ \beta^{\text{ss}},\ R^{\text{ss}} = V^{\text{ss}}/\dot{\psi}^{\text{ss}})$ and the input $(\delta^{\text{ss}},\ s^{\text{ss}}_{RLx},\ s^{\text{ss}}_{RRx})$. This system can be therefore solved numerically using the nonlinear equation solver `fsolve` in MATLAB by providing any of the three unknown variables, for example the triplet $(V^{\text{ss}},\ R^{\text{ss}},\ \delta^{\text{ss}})$. The remaining variables of interest can then be computed using (3.2) and (3.3): the steady-state wheel speeds of the rear wheels ω^{ss}_{RL} and ω^{ss}_{RR} can be found using the calculated values for s^{ss}_{RLx} and s^{ss}_{RRx} and (3.3), while the steady-state drive/brake torques at the rear wheels T^{ss}_{Rj} can be found using the wheel speed dynamics from (3.2d) under steady-state conditions.

3.3.2 Feasibility of Requested Path Radius

We next examine the feasibility of the requested path radius from the driver. Similar to common practice in vehicle stability control [113] we obtain an estimate of the driver's intended path using a neutral steer linear bicycle model under steady-state cornering[1]

$$R_{kin} = \frac{\ell_F + \ell_R}{\tan\delta^{\text{ss}}}.$$

[1]Note that a understeer or oversteer characteristic can be easily used instead if needed.

In the above expression the desired path radius R_{kin} depends only on the steering input from the driver, so it may or may not be feasible depending on the vehicle's velocity. Consider for example the steady-state conditions for a range of steering inputs δ^{ss} and three different fixed velocities V^{ss} in Fig. 3.9. Lets assume that the driver, through a steering command of $\delta = 10$deg, requests a path radius $R = R_{kin}$ of around 14m. Then, if the vehicle velocity is 10.6m/s the requested R_{kin} is feasible, whereas if the vehicle velocity is 12.6m/s the R_{kin} is smaller than the minimum achievable R^{ss} and not feasible anymore. In this case the controller will reduce the vehicle velocity so that the desired R_{kin} becomes feasible again. Taking into consideration the driver's intention this speed reduction needs to be kept to a minimum. To this end, the steady-state velocity is selected such that R_{kin} coincides with the minimum R^{ss}, which in the above example corresponds to a maximum vehicle velocity of $V_{max} = 11.6$m/s.

It follows that there is a limiting value for the steady-state conditions (V^{ss}, β^{ss}, $\dot{\psi}^{ss}$, s^{ss}_{RLx}, s^{ss}_{RRx}) for a specific δ^{ss}: Fig. 3.10 shows the envelopes of the feasible steady-state vehicle velocities V^{ss} and steady-state sideslip angles β^{ss} for a range of steady-state steering angles δ^{ss}. We notice that the value of the maximum V^{ss} decreases exponentially with higher δ^{ss}, while the corresponding limits of β^{ss} show a linear relationship with δ^{ss} and range from negative to positive values.

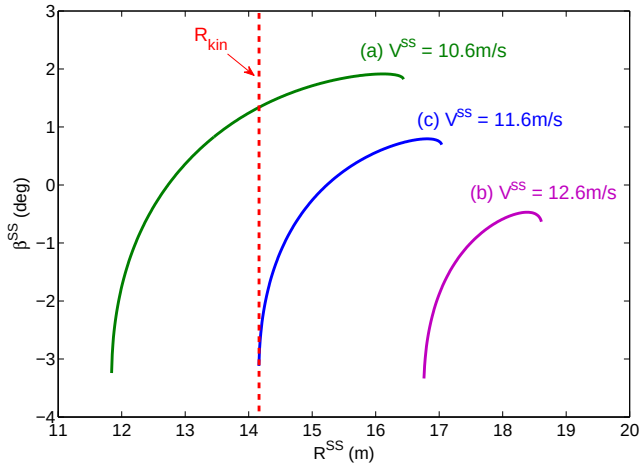

Figure 3.9: Selection of target steady-state according to the driver's steering angle command of δ=10deg: (a) R_{kin} within range of feasible R^{ss} if $V = 10.6$m/s; (b) R_{kin} outside range of feasible R^{ss} if $V = 12.6$m/s; (c) R_{kin} coincides with the minimum calculated R^{ss} if $V = 11.6$m/s.

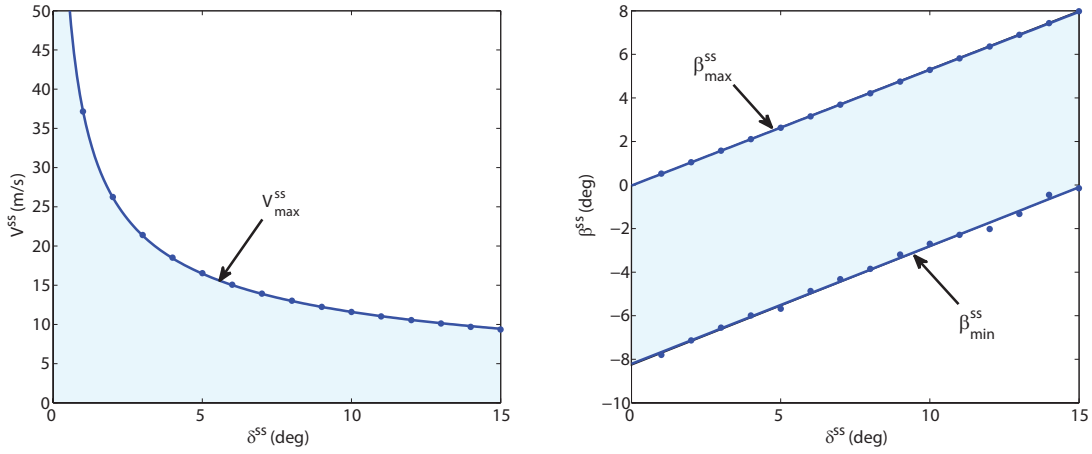

(a) (b)

Figure 3.10: Steady-state regions for V^{ss} and β^{ss} for a range of δ^{ss} values.

Chapter 4

Unconstrained Optimal Control Strategy

4.1 Introduction

In this chapter we examine the use of an unconstrained optimal control strategy to stabilise the vehicle in a terminal understeer situation using the rear axle electric torque vectoring configuration of an RWD EV. The controller is designed to minimise the error between the actual and the reference vehicle state in order to meet the requested path radius through the steering wheel input from the driver according to the analysis of section 3.3 and is constructed in two layers:

1. A unconstrained optimal control strategy based on an LQR provides stabilising rear wheel longitudinal slip inputs.

2. A backstepping control strategy then calculates the necessary drive/brake torques to achieve the longitudinal slips as dictated by the LQR.

After a short review on the use of unconstrained optimal control theory in active chassis control applications, we detail the proposed control strategy and compare it against a baseline vehicle with no active control and a vehicle equipped with a DYC strategy using a PID controller in CarMaker environment, so that its effectiveness in mitigating terminal understeer can be analysed.

4.2 Review of LQR strategies for Active Chassis Control

Optimal control theory seeks to "determine the control signal that will cause a process to satisfy the physical constraints and at the same time minimise (or maximise) a performance criterion" [83]. Such control signal, when it exists, is called the optimal control. Optimal control theory has been so far applied in a diverse number of fields, from biology and ecology, to engineering, management and economics. In the automotive engineering sector it can be found in a variety of topics, ranging but not limited to active and semi-active suspension control [123], driver modelling [130], state estimation [5], obstacle and collision avoidance [47], spark-ignition engine air/fuel ratio control [51] and minimum time manoeuvring [28].

In the case of an unconstrained optimal control problem, the LQR in both its discrete and continuous time forms is the most popular so far design technique, with its basic principle covered in many textbooks [7, 83, 102]: the control is applied on a linear system and seeks to minimise a quadratic cost function, which contains terms that represent both system outputs and inputs, with weights used to specify the relative importance of each term. In the standard LQR formulation, the system is assumed time-invariant and the optimisation extends over infinite time while it is also assumed that the state of the plant is

available for feedback, with the existence of the optimal control depending on the system's detectability and stabilisability. This latter requirement is sometimes relaxed by using an output-feedback control, with examples in the literature showing that an optimal control based on a restricted set of measurements can be as good as one that is based on full-state information [129].

Looking more specifically in the application of LQR for active chassis control, in [122] we find a DYC strategy applied on an AWD prototype EV. For the optimal control problem, the bicycle model with the yaw moment and the steering angle as inputs is augmented with the rate of yaw moment in order to eliminate steady state yaw rate tracking errors. A 'skid detector' is also constructed, in order to detect locking/spinning of the wheels and reduce the requested yaw moment from the controller under such cases. Experimental results show that the proposed strategy is robust against cornering stiffness errors but results in loss of stability on low-μ surfaces, despite the use of the skid detector to identify large tyre slip values.

Another example of an LQR application for active chassis control can be found in [109] where a lateral dynamics control strategy constructed in two levels is presented. On the high level, a bicycle model is augmented with integral action on the yaw rate and a LQR finds the 'control effects' (as the authors call them) so that the yaw rate and sideslip angle errors are minimised. Then the low level control allocation computes the necessary steering angle and individual wheel braking to meet these 'control effects' by solving a QP problem, which seeks to minimise a quadratic cost function subject to the allocation error (equality constraint) and the actuator limits (inequality constraints). Simulations results focusing on the reconfiguration abilities of the proposed solution in the event of a front brake or steering failure show that the controller successfully completes a double-lane change by redistributing the control effort to the available actuators.

Use of an LQR strategy for stabilisation of a vehicle during extreme operating condi-

tions using longitudinal control only can be found in [40, 142]. Here steady-state cornering conditions which include operation of the tyres in the nonlinear region are calculated considering a single-track vehicle model with independent front and rear wheel torque inputs that also takes into consideration the normal load transfer effect during acceleration/braking. The resulting steady-state trajectories therefore include cases of aggressive sideslip angle, more commonly referred to as 'drifting' conditions. The stabilising control architecture then consists of an LQR strategy with longitudinal slip inputs, and an SMC to provide the necessary drive/brake torques, the reason for using longitudinal control only motivated by techniques such as the 'left-foot braking' used in race driving. Simulation studies show that the proposed strategy can stabilise the vehicle under different equilibrium conditions, including extreme vehicle operating cases usually achieved only by expert rally drivers.

Stabilization of high sideslip angle cornering equilibria on an RWD vehicle using an LQR is presented in [143]. Here, the single-track model from the previous papers [40, 142] is replaced by a four-wheel vehicle model – thus avoiding simplifications associated with the use of pure longitudinal control – and the complete control strategy consists of: (i) a LQR which finds the front steering angle and the rear wheel speeds in order to stabilise the vehicle with respect to drifting equilibria, (ii) a backstepping controller which calculates the rear differential drive torque necessary to meet the rear wheel speeds commands from the LQR. The steady-state cornering equilibria are calculated using the same four-wheel vehicle model, with the computed steady-state drifting conditions giving a close match to experimental data for vehicle trajectories with the same constant path radius. Two simulation scenarios set to emulate the cornering conditions recorded during experiments using a rally car reveal that the actions from the proposed controller shows a close resemblance to the response of the actual vehicle despite the absence of disturbances in the simulation model.

4.3 LQR with Backstepping Strategy

From section 4.2, we can see that unconstrained optimal control theory can be successfully applied on a active chassis control problem, both in sub-limit and limit handling conditions. Another recurring theme of interest from the above analysis is the distinction between the high level vehicle dynamics and the low level wheel dynamics, with most of the solutions using an optimal control strategy to follow a target on the top vehicle level, combined with a low level slip controller to provide the necessary torques on the wheels. This distinction is not unusual in the active chassis control literature and comes from the fact that the high level vehicle dynamics are much slower than the wheel dynamics, giving the opportunity to differentiate them by using a Multi-Input Multi-Output (MIMO) control strategy for the first and a simpler low level control strategy for the second.

Based on the above observations, in this section we present an unconstrained optimal control strategy combined with a backstepping controller in order to stabilise the vehicle in a terminal understeer situation which is constructed in a way similar to [143], with the complete structure as seen in Fig. 4.1.

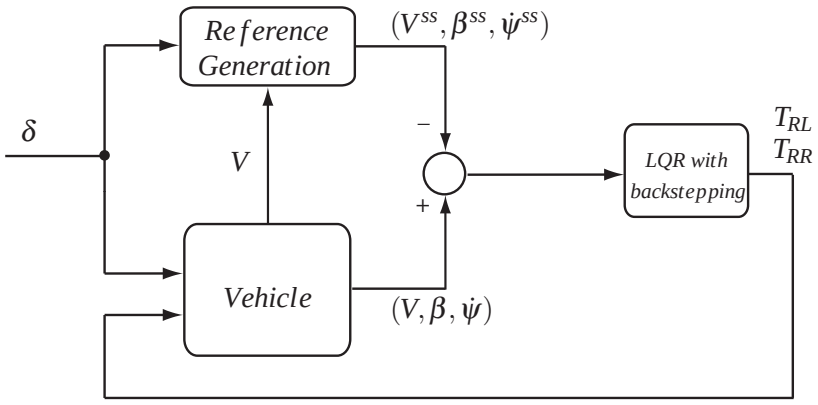

Figure 4.1: LQR with backstepping control structure.

4.3.1 Rear Wheel Longitudinal Slip Control

Neglecting the wheel speed dynamics (3.2d), enforcing zero longitudinal tyre forces at the front wheels according to the chosen drivetrain topology and considering the steering angle $\delta = \delta^{ss}$ as a constant parameter provided by the driver, the four-wheel vehicle model (3.2) can be expressed as a system with s_{RLx} and s_{RRx} as control inputs:

$$\dot{V} = h_1(V, \beta, \dot{\psi}, s_{RLx}, s_{RRx}), \tag{4.1a}$$

$$\dot{\beta} = h_2(V, \beta, \dot{\psi}, s_{RLx}, s_{RRx}), \tag{4.1b}$$

$$\ddot{\psi} = h_3(V, \beta, \dot{\psi}, s_{RLx}, s_{RRx}). \tag{4.1c}$$

Linearising (4.1) about the equilibrium point (x^{ss}, u^{ss}) we obtain:

$$\dot{\widetilde{x}} = A^{ss}\widetilde{x} + B^{ss}\widetilde{u}, \tag{4.2}$$

where

$$\widetilde{x} = \begin{bmatrix} V - V^{ss} \\ \beta - \beta^{ss} \\ \dot{\psi} - \dot{\psi}^{ss} \end{bmatrix}, \quad \widetilde{u} = \begin{bmatrix} s_{RLx} - s_{RLx}^{ss} \\ s_{RRx} - s_{RRx}^{ss} \end{bmatrix},$$

and A^{ss} and B^{ss} are the Jacobian matrices evaluated at the equilibrium point,

$$A^{ss} = \begin{bmatrix} \frac{\partial h_1}{\partial V} & \frac{\partial h_1}{\partial \beta} & \frac{\partial h_1}{\partial \dot{\psi}} \\ \frac{\partial h_2}{\partial V} & \frac{\partial h_2}{\partial \beta} & \frac{\partial h_2}{\partial \dot{\psi}} \\ \frac{\partial h_3}{\partial V} & \frac{\partial h_3}{\partial \beta} & \frac{\partial h_3}{\partial \dot{\psi}} \end{bmatrix}, \quad B^{ss} = \begin{bmatrix} \frac{\partial h_1}{\partial s_{RLx}} & \frac{\partial h_1}{\partial s_{RRx}} \\ \frac{\partial h_2}{\partial s_{RLx}} & \frac{\partial h_2}{\partial s_{RRx}} \\ \frac{\partial h_3}{\partial s_{RLx}} & \frac{\partial h_3}{\partial s_{RRx}} \end{bmatrix}. \tag{4.3}$$

Then the linear control law

$$\widetilde{u} \;=\; K\widetilde{x}, \tag{4.4}$$

where

$$K = -R_c^{-1}(B^{ss})^T P, \tag{4.5}$$

is the control gain matrix with P the symmetric positive-definite solution to the associated Algebraic Riccati Equation (ARE)

$$(A^{ss})^T P + PA^{ss} - PB^{ss}R_c^{-1}(B^{ss})^T P + Q_c = 0, \tag{4.6}$$

stabilises the equilibrium $\widetilde{x} = [0\ 0\ 0]^T$ and minimises the quadratic cost functional [102]

$$J = \int_0^\infty \left[\widetilde{x}(t)^T Q_c \widetilde{x}(t) + \widetilde{u}(t)^T R_c \widetilde{u}(t)\right] \mathrm{dt}. \tag{4.7}$$

In the above expression Q_c is the real, symmetric and positive semi-definite matrix,

$$Q_c = \mathrm{diag}\left\{ q_V \left(\frac{1}{V_{max}(\delta)}\right)^2, \quad \left(\frac{1}{\beta_{max}(\delta)}\right)^2, \quad \left(\frac{1}{\dot{\psi}_{max}(\delta)}\right)^2 \right\}, \tag{4.8}$$

and R_c is the real, symmetric and positive definite matrix [102],

$$R_c = \mathrm{diag}\left\{ \left(\frac{1}{s_{RLx_{max}}(\delta)}\right)^2, \quad \left(\frac{1}{s_{RRx_{max}}(\delta)}\right)^2 \right\}, \tag{4.9}$$

where both matrices are set as function of the given steering input and, after normalization with respect to the maximum expected state and input values according to Bryson's rule [22], the only tuning parameter is q_V. Then, higher q_V values can result in faster tracking of the set velocity reference, but at the expense of a more oscillatory yaw rate and sideslip

angle response in the case of the unconstrained optimal control formulation considered in this chapter.

4.3.2 Motor Torque Control

A backstepping controller is designed next to calculate the necessary wheel drive/brake torques T_{RL} and T_{RR} for the regulation of the longitudinal slips on the rear wheels as requested by the LQR.

The dynamic equations that govern s_{RLx} and s_{RLx} can be derived by differentiating the longitudinal slip equation (3.3) and using the wheel speed dynamics (3.2d):

$$\dot{s}_{RLx} = f_1 + g_1 T_{RL}, \tag{4.10a}$$

$$\dot{s}_{RRx} = f_2 + g_2 T_{RR}, \tag{4.10b}$$

where

$$f_1 = \frac{\dot{V}_{RLx}}{\omega_{RL} R_w} + \frac{1}{I_w}\frac{V_{RLx} f_{RLx}}{\omega_{RL}^2}, \qquad g_1 = -\frac{1}{I_w}\frac{V_{RLx} R_w}{(\omega_{RL} R_w)^2},$$
$$f_2 = \frac{\dot{V}_{RRx}}{\omega_{RR} R_w} + \frac{1}{I_w}\frac{V_{RRx} f_{RRx}}{\omega_{RR}^2}, \qquad g_2 = -\frac{1}{I_w}\frac{V_{RRx} R_w}{(\omega_{RR} R_w)^2}.$$

Incorporating the longitudinal slip dynamics into (4.2) we obtain

$$\dot{\widetilde{x}} = A^{ss}\widetilde{x} + B_1\widetilde{u}_1 + B_2\widetilde{u}_2, \tag{4.11a}$$

$$\dot{\widetilde{u}}_1 = f_1(\widetilde{x}, \widetilde{u}_1) + g_1(\widetilde{x}, \widetilde{u}_1) T_{RL}, \tag{4.11b}$$

$$\dot{\widetilde{u}}_2 = f_2(\widetilde{x}, \widetilde{u}_2) + g_2(\widetilde{x}, \widetilde{u}_2) T_{RR}, \tag{4.11c}$$

where B_1 and B_2 are the first and second columns of B^{ss} from (4.3), and $\widetilde{u}_1$ and $\widetilde{u}_2$ the first

and second rows of $\widetilde{u}$ from (4.4).

Recall that the control law $\widetilde{u}_1 = \phi_1(\widetilde{x}) = K_1\widetilde{x}$ and $\widetilde{u}_2 = \phi_2(\widetilde{x}) = K_2\widetilde{x}$ asymptotically stabilises (4.2) with Lyapunov function $\mathscr{V}_0 = \frac{1}{2}\tilde{x}^T P\tilde{x}$, where K_1 and K_2 are the first and second columns of K from (4.5) and P is the solution of (4.6). Defining $z_1 = u_1 - \phi_1(\widetilde{x})$ and $z_2 = u_2 - \phi_2(\widetilde{x})$ results in the equivalent system representation

$$\begin{aligned}
\dot{\widetilde{x}} &= (A^{ss}\widetilde{x} + B_1\phi_1 + B_2\phi_2) + B_1 z_1 + B_2 z_2, && \text{(4.12a)}\\
\dot{z}_1 &= v_1, && \text{(4.12b)}\\
\dot{z}_2 &= v_2, && \text{(4.12c)}
\end{aligned}$$

with

$$\begin{aligned}
v_1 &= f_1 + g_1 T_{RL} - \frac{\partial \phi_1}{\partial \widetilde{x}}(A^{ss}\widetilde{x} + B_1\phi_1 + B_2\phi_2 + B_1 z_1 + B_2 z_2), && \text{(4.13a)}\\
v_2 &= f_2 + g_2 T_{RR} - \frac{\partial \phi_2}{\partial \widetilde{x}}(A^{ss}\widetilde{x} + B_2\phi_2 + B_2\phi_2 + B_1 z_1 + B_2 z_2). && \text{(4.13b)}
\end{aligned}$$

Then, considering the Lyapunov Function candidate $\mathscr{V} = \mathscr{V}_0 + \frac{1}{2}(z_1^2 + z_2^2)$, we obtain

$$\begin{aligned}
\frac{\mathrm{d}\mathscr{V}}{\mathrm{dt}} &= \frac{\partial \mathscr{V}_0}{\partial \widetilde{x}}(A^{ss}\widetilde{x} + B_1\phi_1 + B_2\phi_2 + B_1 z_1 + B_2 z_2) + z_1 v_1 + z_2 v_2\\
&\leq \frac{\partial \mathscr{V}_0}{\partial \widetilde{x}} B_1 z_1 + \frac{\partial \mathscr{V}_0}{\partial \widetilde{x}} B_2 z_2 + z_1 v_1 + z_2 v_2,
\end{aligned}$$

hence the control

$$\begin{aligned}
v_1 &= -\frac{\partial \mathscr{V}_0}{\partial \widetilde{x}} B_1 - \hat{k}_1 z_1, \qquad \hat{k}_1 > 0, && \text{(4.14a)}\\
v_2 &= -\frac{\partial \mathscr{V}_0}{\partial \widetilde{x}} B_2 - \hat{k}_2 z_2, \qquad \hat{k}_2 > 0, && \text{(4.14b)}
\end{aligned}$$

asymptotically stabilises (4.12) [77]. Equivalently, solving (4.13) for T_{RL} and T_{RR} and

using (4.14), we obtain the rear wheel torque inputs which asymptotically stabilise (4.11).

4.4 Evaluation of the LQR strategy

In this section we compare the above derived LQR strategy against a baseline vehicle with no active control and a vehicle equipped with a DYC strategy (refer to Appendix B for details on the DYC structure) in a terminal understeer scenario. The purpose of this test is to see the effect of the combined control of the longitudinal and lateral dynamics of the vehicle in the case of overspeeding through a corner, and the relative advantages and disadvantages of employing an unconstrained optimal control strategy in such cases.

For this simulation scenario the driver model available in CarMaker is used to steer the vehicle around a U-turn (details on the road geometry can be found in Appendix F). It is assumed that the road is dry (μ_{max}=1) and that no acceleration or deceleration commands come from the driver for the duration of the manoeuvre, while the entry speed is set to 80km/h and the velocity error penalty in (4.8) to $q_V = 150$. Note also that, considering the power limitations of the electric motors, the actual torques applied on the rear wheels are always saturated according to the static torque map (Fig. A.1 in Appendix A).

Fig. 4.2a shows the trajectories of the uncontrolled vehicle (in green), the vehicle with the DYC (in red) and the vehicle with the LQR (in blue). We can see that both the uncontrolled vehicle and the vehicle using the DYC strategy follow a wider trajectory, with almost identical response close to the apex of the corner. On the other hand, the vehicle with the LQR strategy achieves a tighter trajectory and stays at the inner part of the corner for the duration of the manoeuvre.

In Figs. 4.2b-4.2e we find the steering wheel angle, velocity, sideslip angle and yaw rate time histories for the three vehicle configurations. As we can see from Fig. 4.2c, the LQR strategy successfully regulates the velocity of the vehicle, but at the expense of

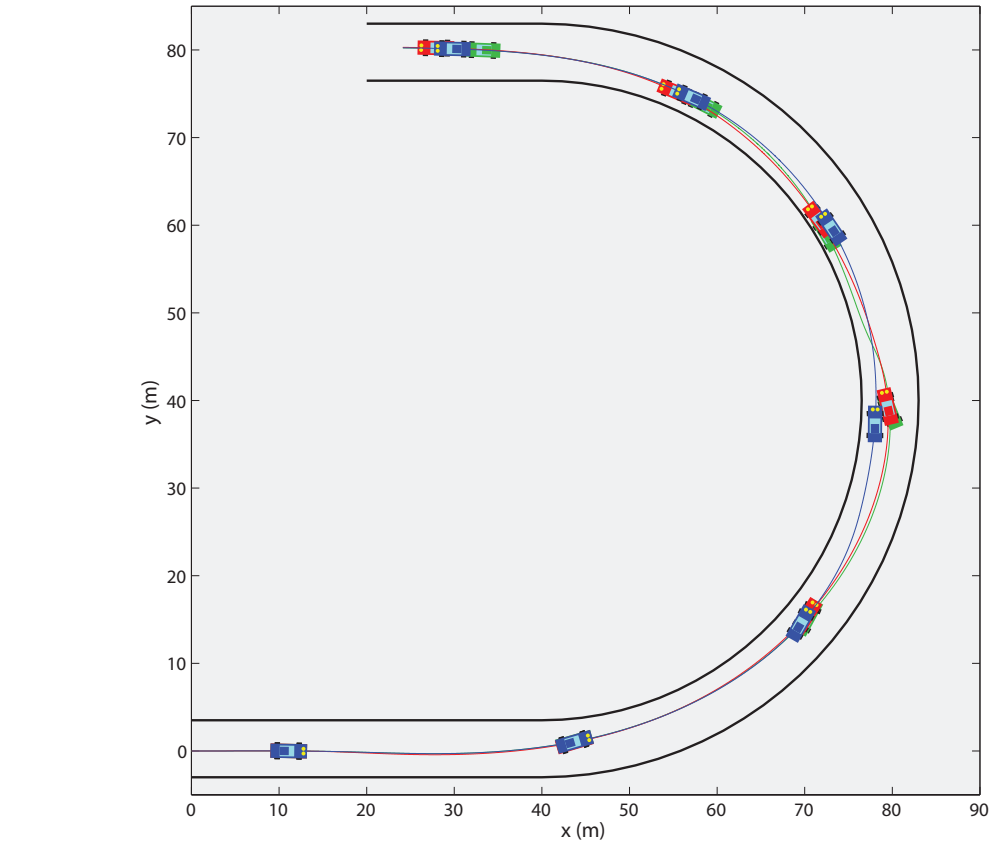

(a) Trajectory

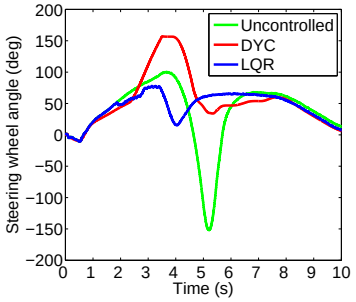

(b) Steering wheel angle

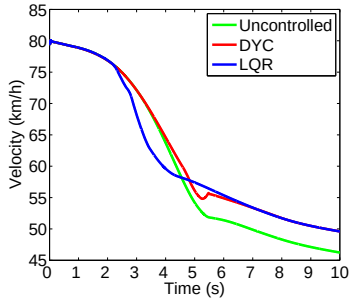

(c) Velocity

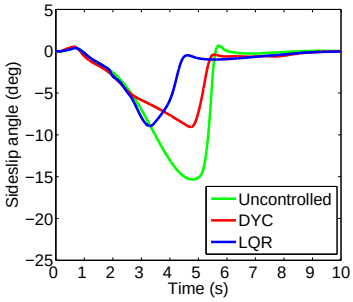

(d) Sideslip angle

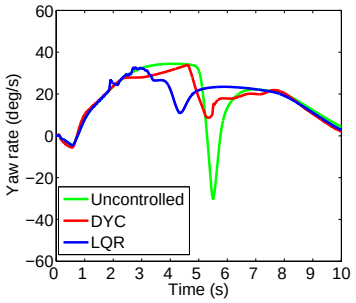

(e) Yaw rate

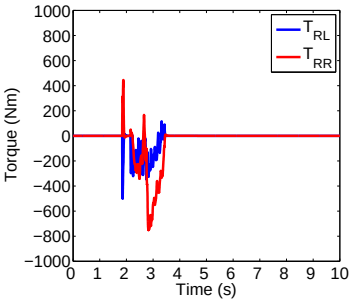

(f) LQR torques

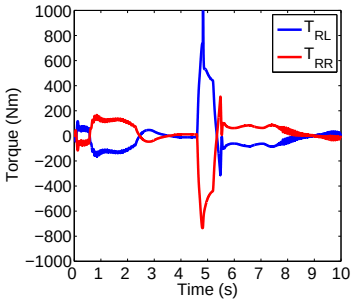

(g) DYC torques

Figure 4.2: Comparison of the uncontrolled vehicle (in green), the vehicle with the DYC (in red) and the vehicle with the LQR (in blue).

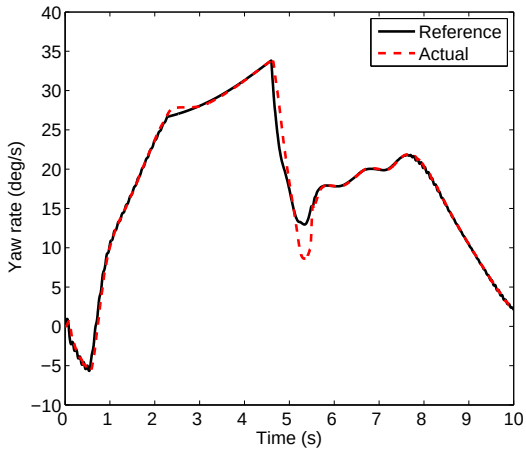

Figure 4.3: Yaw rate reference tracking from the DYC strategy.

large sideslip angle (Fig. 4.2d) and yaw rate (Fig. 4.2e) values. On the other hand, the vehicle with the DYC strategy exhibits a velocity drop similar to the one observed for the uncontrolled vehicle and a large sideslip angle (Fig. 4.2d) with a peak similar to the LQR strategy. Finally, the uncontrolled vehicle shows an even larger sideslip angle (Fig. 4.2d) which requires a counter-steering action from the driver as observed in the steering wheel angle time history of Fig. 4.2b so that the vehicle stays on path.

Looking at the torque commands from the two strategies in Figs. 4.2f-4.2g we observe that the LQR strategy requests mainly braking torques from the two motors, while the DYC uses a differential torque to achieve the reference yaw rate. It is interesting to note at this point the difference between the rear-left and rear-right torque commands from the LQR which is an indication of the combined longitudinal and lateral regulation of the vehicle from this strategy, and come in clear contrast to the differential torque from the DYC strategy.

The inability of the DYC strategy to achieve a tighter turn as evidenced above is not a result of poor yaw rate tracking from the controller: as we can see from Fig. 4.3 the performance of the controller is, apart from a small undershoot at around 5s, excellent.

It is therefore obvious that in a terminal understeer scenario like the one examined here, regulating the velocity of the vehicle through a strategy like the LQR strategy presented in this section is necessary.

4.5 Summary

In this chapter we presented an unconstrained optimal control strategy to stabilise the vehicle under terminal understeer cases using the rear axle electric torque vectoring configuration of an RWD EV. A test scenario involving a car entering a U-turn with excessive speed confirmed the importance of velocity regulation in the terminal understeer cases, but also showed that using an unconstrained control strategy can result in large sideslip angle values. Such behaviour could be potentially avoided by changing the relative penalisation on the velocity, yaw rate and sideslip angle errors from the given references in (4.7). However, even after excessive tuning of the parameter q_V in (4.8), there are no guarantees that the final solution will perform as expected under all possible scenarios. On the other hand, a more direct and efficient way to avoid large yaw rate and sideslip angle values is through the use of a constrained optimal control strategy, as we are going to see in the chapters to follow.

Chapter 5

Linear Constrained Optimal Control Strategy

5.1 Introduction

In this chapter we investigate the use of MPC for stabilization of the vehicle near the limits of lateral acceleration using the same rear axle electric torque vectoring configuration of an RWD EV as before. While the use of a constrained optimisation strategy such as the MPC has obvious advantages over the LQR of chapter 4 it also has distinct disadvantages as we are going to see in the section to follow, which are mainly related to the computational time needed to construct and solve the resulting optimization problem. Based on this observation, the goal of this chapter is not only to develop an appropriate MPC strategy for the demanding task of stabilising the vehicle near the limits of handling in the best possible way, but also one that can be implemented in real time.

The structure of this chapter is as follows: after a short historical perspective on MPC and its applications on active chassis control problems, two linear MPC strategies of different complexity are constructed: (i) one using the full four-wheel vehicle model 3.2 and (ii) a simpler one that neglects the wheel speed dynamics (3.2d) in a way similar to the LQR strategy of chapter 4. The effect of varying the sampling time and the horizon on the performance and the computational load of each strategy are then analysed. Finally, the two strategies are compared against each other and the LQR strategy from chapter 4 under two limit handling manoeuvres in CarMaker environment: the first one examining the terminal understeer correction capabilities of the two MPC strategies and the second one checking the importance of constraining the state and input in the case of a highly transient manoeuvre.

5.2 Review of MPC strategies for Active Chassis Control

MPC takes its name from the way the control law is computed [97]:

1. At current time k a model of the plant, called hereafter 'the internal model', is used to predict its response $\overline{y}(t|k)$[1] to changes in the control input u along the prediction horizon N_p.

2. The control input sequence along the control horizon $N_u \leq N_p$ is chosen so that the response of the system meets specific requirements subject to the imposed constraints.

3. Only the first control input calculated is applied.

4. At the next time $(k+1)$ the procedure is repeated with the N_p and N_u moved by one time step.

[1]The notation $(t|k)$ is used to show that the prediction depends on the system condition at time k.

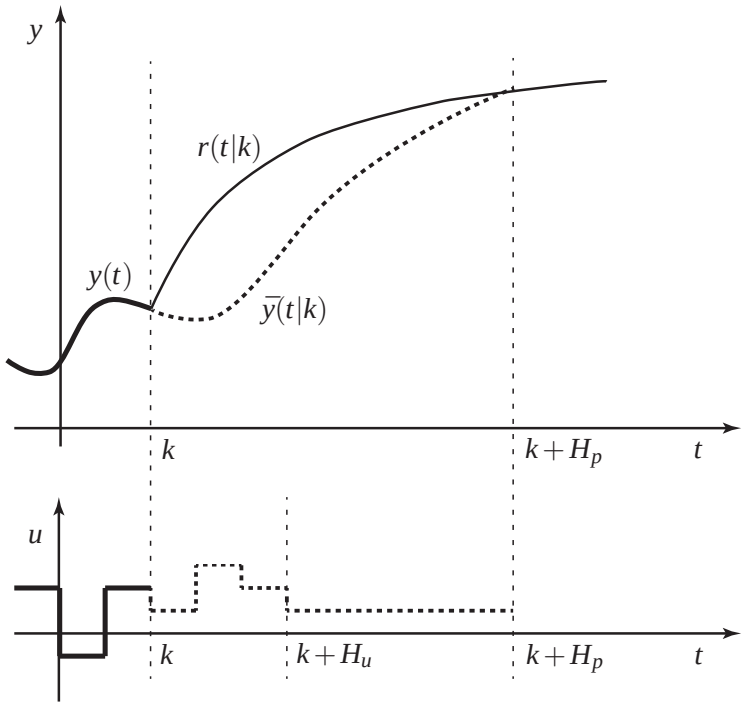

Figure 5.1: The basic MPC idea.

The requirements are usually set so that the output of the system follows a prescribed trajectory $r(t|k)$ with as small control effort as possible in the form of a quadratic cost function, the latter guaranteeing that the solution of the subsequent optimization problem is unique [93]. The constraints on the other hand are included in the problem formulation to avoid exceeding specific thresholds, usually related to the physical limits of the system.

MPC traces its origins in the control of chemical processes where it has been extensively used due to its distinctive features which fit nicely with the problem of running efficiently a chemical plant: it has slow dynamics with sampling times measured in minutes or hours, a large number of inputs and outputs, while the optimum point of operation is usually close to its physical limits. Furthermore, the controller can be appropriately tuned for a single plant and the cost for controller development becomes irrelevant when compared to the building and running costs of the plant [24]. The evolution of MPC can be seen through the development of the different algorithms published in the past fifty

years: early examples used step and impulse response models and ad hoc treatments of input and output constraints, which was changed in the 2nd generation by formulating the problem as a QP problem, followed by the 3rd generation which featured different levels of constraints (hard, soft, ranked) and provided mechanisms to recover from an infeasible solution, and the 4th generation which looked closer to the NMPC problem [110]. In a rather independent way a similar methodology called Generalised Predictive Control was developed in the adaptive control community. By the 90s, it became obvious that the differences between the above mentioned formulations are irrelevant and the generic title of MPC was used for "that mode of control in which the current control action is determined by solving on-line an optimal control problem" [95]. The focus has now shifted to the study of stability and robustness: the use of a terminal cost and/or a terminal constraint set was studied to address stability, while formulations such as the min-max and feedback MPC were suggested to address robustness. In the last 15 years both academia and industry have tried to address the open challenges still remaining if the MPC is to be applied in a wider range of systems. However, guaranteeing closed-loop properties such as stability and robustness while reducing the computational cost is definitely not an easy task. Furthermore, a fast and systematic way to design and tune MPC controllers has yet to be found. Despite these challenges, the benefits of using MPC for construction of optimal controllers have attracted a lot of research, with a multitude of solutions addressing general or application specific systems.

The huge leaps in computational power and memory storage in the past 20 years have led to extensive research on potential application of MPC in 'large volume' domains, such as the aerospace, automotive and robotics industries [24]. This technological advancement allowed for the expensive MPC formulation to be adapted by industries which have different characteristics and requirements to the chemical process industry: here the system dynamics are fast, exhibit highly nonlinear behaviour, and the controller needs to

be applied to large volumes with reduced costs. On the other hand, the number of inputs and outputs is lower, while the system usually does not operate close to its physical limits [24].

From the automotive sector a variety of MPC solutions can be found in the literature, ranging from steering [42] to active and semi-active suspension control [27], engine management [51], emission regulation [112] and control of vehicle platoons [111]. Looking more specifically in the area of active chassis control, we can distinguish two main MPC application areas: (i) on the control of autonomous and semi-autonomous vehicles and (ii) on active safety control systems. However, it is interesting to note at this point that the distinction between autonomous vehicle control and active safety control is becoming less clear nowadays, mainly due to the rapid development of sensor technologies and sensor fusion algorithms.

5.2.1 MPC in Autonomous Vehicle Applications

Autonomous vehicles pose a problem which fits the MPC formulation nicely: the idea of following a predefined trajectory as close as possible while respecting the road, vehicle and actuator limits can be directly addressed by solving a constrained optimization problem. A recurring theme in the autonomous vehicle literature is how the controller will handle an obstacle avoidance scenario. Such a scenario calls for a difficult problem to be solved and advanced strategies are required in order to achieve a stable operation of the vehicle in both the longitudinal and lateral direction while respecting the constraints of the problem like the road geometry and the vehicle and tyre physical limits. In this section we will therefore list all solutions that assume road preview information, including solutions that allow the driver to interact with the vehicle and take full control only under emergency situations (commonly known as semi-autonomous vehicle applications).

From the autonomous vehicle applications, a characteristic example is the series of papers from Borrelli, Falcone and Keviczky [21, 41–44, 76], which explore the application of MPC for trajectory tracking in an autonomous vehicle application using the AFS system with/without differential braking and traction control. In the first two papers of the series [21, 76] we find an NMPC strategy for tracking a predefined trajectory using the AFS of an autonomous vehicle that, according to the authors, sets the 'benchmark' against which future sub-optimal strategies can be compared against. The first paper [21] presents the NMPC strategy which is based on a bicycle model coupled with a MF as the tyre model that does not take into account the load transfer effects due to acceleration/deceleration of the vehicle and tries to track the yaw angle and the lateral displacement references in the global frame while respecting the steering rate input constraints. Using a double-lane change scenario under different entry speeds, the authors report the necessary increase in both the prediction and control horizon with higher speeds to keep the vehicle stable and the subsequent increase in computational time. From the simulation results we can also see that higher entry speeds result in higher deviations from the reference trajectory, something that is expected according to the analysis on terminal understeer presented in section 2.3. The authors also present a short analysis of the impact of constraint violations on the computational time. For the second paper [76], the effect of a sidewind is modelled, with simulation results showing good disturbance rejection up to 10m/s, but again high computational costs. Although the NMPC application presented in [21, 76] gives the opportunity to check what is physically possible in a highly nonlinear case, the use of a bicycle model as an internal model for the NMPC formulation along with the disregard of load transfer effects (therefore the nonlinearity in the model coming from the tyre model only) negates somehow the benefits of such formulation used as a benchmark solution.

Since the NMPC strategy proposed in [21, 76] can not be implemented online, a Linear

Time Varying (LTV) MPC controller is presented in the next paper [42]. For the LTV-MPC formulation the NMPC problem from [21,76] is linearised about the operating point while an additional constraint is imposed on the front slip angle, the main reason being that the vehicle becomes unstable without it. Simulation and experimental results show that the LTV-MPC strategy shows no infeasibility problems with higher initial velocities but poorer tracking when compared to the NMPC. Another control strategy that is based on the same LTV-MPC but with a control horizon of only one time step is also presented: this simplifies the optimization problem even further and makes possible to compute the maximum number of operations per time step, with only a slight degradation on tracking performance reported from the authors.

In the next two papers the authority of the MPC controller is extended by including independent wheel braking [41] or independent wheel braking and active front and rear differentials [44]. Another difference from the previous papers is the necessary replacement of the bicycle model by a four-wheel vehicle model for application of the braking/active differential strategy, although load transfer effects are again not taken into account. The vehicle model is linearised again about the operating point and, assuming a separate slip controller on each wheel, the MPC strategy is constructed using AFS and slip on the four wheels as the control input. The goal is then to follow a predefined trajectory like before but also keep the longitudinal velocity of the vehicle as close as possible to a given reference. Looking at the simulation tests from [44] using a double lane change on a low-μ surface, a comparison between the three drivetrain topologies presented so far can be found: (i) one using AFS with braking and traction control, (ii) another one that neglects the traction control and (iii) one that has AFS only. For the tests, the reference velocity is set equal to the initial vehicle velocity and therefore an inevitable decrease in speed is noticed due to the vehicle reaching a terminal understeer condition. It is interesting to note here that, although the authors report that the solution that combines AFS with brak-

ing and traction control has the best overall performance, the best lateral position tracking is achieved by the solution that uses AFS with braking control only. This observation actually points to a different result from the one drawn by the authors: in an autonomous vehicle application under an obstacle avoidance scenario as the authors claim this study to be, the lateral position tracking is more important than maintaining the initial speed, and then maybe the best performance is achieved by the AFS with braking control solution.

In the final paper of the series [43] the authors construct two NMPC strategies using internal vehicle models of different levels of fidelity, one that employs a four-wheel vehicle model with wheel dynamics and control inputs the front steering and individual wheel brake torques and another one that uses a bicycle model instead with a direct yaw moment along with AFS as control inputs. While simulation tests on a double-lane change show promising results, the main problem for both controllers remains the high computational cost which makes it impossible to implement them in real time. For this reason, a third controller which uses a linearisation of the first, more complex, controller about the operating point is also developed and tested on a vehicle with rather good path tracking results. The three controllers presented in [43] show again some of the trade-offs that are sometimes necessary when we setup an MPC problem with each controller exhibiting certain advantages and disadvantages, although a recurring topic seems to be the importance of good tuning. An interesting point to note here is that although velocity regulation was included in the first controller, the authors set the reference velocity simply equal to the initial one and chose not to check the effect of setting a lower reference velocity. This was done in an attempt to follow the original assumption that velocity will remain largely unchanged – indeed, the setting of the second controller was heavily based on this assumption – something that was not the case as we can see from the constant velocity reduction from all controllers in the performed tests.

An autonomous vehicle controller assuming decoupled longitudinal and lateral dy-

namics can be found in [8], which presents an NMPC for lateral dynamics control using AFS combined with a simple CC for control of the longitudinal dynamics to avoid overspeeding through a curve. NHTSA's criterion on the maximum entry speed based on the curvature of the road and its camber angle, along with a dynamic criterion based on sideslip angle information are used to find the maximum allowable entry speed so that the necessary deceleration can be found. Simulation results using a double-lane change manoeuvre show that a good tracking is achieved when the entry speed is below the maximum allowable. The authors in [8] present a decoupled longitudinal and lateral dynamics control based on the observation that excessive entry speed degrades the path-following abilities of a lateral dynamics only controller. The choice to design a separate CC strategy was most probably done on the basis that including the speed regulation in the optimization problem (indeed, the vehicle model used allows for this) would result in higher computational costs for the NMPC formulation. However, it would be interesting to check the decoupled strategy presented here against such a formulation.

Two papers that explore the application of fast optimization algorithms in the context of a real-time MPC in autonomous vehicle applications can be found in [47, 100]. In [47] a real-time NMPC strategy that employs the Real Time Iteration (RTI) scheme originally proposed in [35] on an autonomous vehicle application is presented. The authors use a four-wheel vehicle model and a nonlinear tyre model to derive the track-dependent spatial dynamics for the NMPC strategy. Results show that the proposed solution is implementable online and that it can successfully navigate around two consecutive obstacles in a simulation test but at a relative low vehicle speed. In [100] a collision avoidance method for an autonomous vehicle is presented, with the NMPC strategy constructed using a single-track vehicle model and a nonlinear tyre model and solved using the continuation/GMRES algorithm [103]. Simulation results show that a vehicle equipped with the proposed controller can successfully avoid an obstacle, however the time to compute a

solution is still much greater than the sampling time and the solution is not implementable online.

A semi-autonomous vehicle application can be found in [4], which presents a controller that predicts and corrects road departure using road preview information. The proposed solution is constructed in two layers: (i) the 'Threat Assessment' layer evaluating the risk and choosing the most effective control policy with the least intrusion to the driver and (ii) the 'Intervention' layer that applies the corresponding control strategy. By control policies the authors denote the level of intervention from the controller, whereas the first policy corresponds to no control action, the second to braking intervention and the third to AFS with braking intervention. From the three policies, only the third one uses a MPC strategy to calculate the necessary steering input and braking torques for minimization of the yaw and lateral position error, subject to constraints on the inputs and the wheel slip angle. Experimental and simulation results through a turn on an icy road with a high entry speed show that the controller brakes in anticipation of the turn, something that allows for a smoother negotiation of the corner when compared to results from a standard ESP intervention which brakes later in the turn but much harder in order to keep the vehicle stable. The controller presented shows that using road preview information is more effective with its early brake application than an ESP strategy in keeping the vehicle stable while being much less intrusive to the driver, with less counter-steering needed from the driver and less deceleration.

Another semi-autonomous vehicle application can be found in [54], where an MPC strategy for roadway departure prevention using AFS and braking is presented. The MPC is formulated so that only the control effort is minimised subject to the input constraints and the soft safety constraints, the latter set so that: (i) the vehicle stays within the lane boundaries, expressed as constraints on the lateral position of all four wheels from the lane centreline, and (ii) the vehicle operates within its stable operating region, expressed

as constraints in the tyre slip angles. A series of simulation experiments with a driver in the loop is then used to assess the effectiveness of the controller. In the first test the authors check if the driver model correctly predicts the behaviour of the driver, with moderate results. In the next test the scenario of a vehicle overspeeding through a turn is investigated with good results: the controller successfully keeps the vehicle within the lane boundaries by using both the AFS and the braking capabilities of the vehicle. The last test checks what would happen if the driver is distracted, hence the vehicle drifts towards the inside (or outside) of the lane: although in this case the driver could still correct the problem he would have to deviate from the 'nominal behaviour' described by the driver model, something that is correctly identified by the controller which steers the vehicle back in the lane according to the safety constraints.

5.2.2 MPC in Active Safety Control Systems

In the scope of active safety systems, most solutions have so far focused in the control of the lateral dynamics of the vehicle using a linear or an explicit MPC formulation. For example, in [11] a yaw stability controller based on an LTV-MPC strategy using independent braking of the four wheels is presented. For the MPC formulation, the lateral vehicle dynamics model with the braking longitudinal forces on all four wheels as the control inputs is linearised about the current position and hard constraints are imposed on states and inputs, whereas the braking longitudinal forces are constrained according to the corresponding estimated lateral tyre forces. The 'sine and dwell' test in Carsim is then used on three different cars, where the tuning parameters (sampling time, control horizon etc) are chosen according to the specific vehicle configuration. Using NHTSA's performance indices for yaw rate and lateral displacement, it is shown that the controller successfully completes the test within the performance requirements. The importance of

correctly choosing the weighting Q and R matrices in the cost function is also tested, with simulation results showing that over-penalising the yaw rate error over the sideslip angle error can create an unstable vehicle behaviour. It is interesting to note here that although the authors recognise that the problem of overspeeding through a curve is the main reason for failing to follow a reference yaw rate, they make no attempt to regulate the forward speed of the vehicle in a controlled matter. From the simulation results we can see that the vehicle eventually slows down, but this is directly connected to the fact that a braking strategy is used.

In [15], a linear MPC is used in a lateral stability control application using the steer-by-wire system of a prototype EV with two independent electric motors on the rear axle. For the control design a affine force-input model is tailored to the specific vehicle configuration: the bicycle model is set with the front lateral force as input, while the rear lateral force is linearised about the current rear tyre slip angle. The rear tyre force coupling is also accounted for by restricting the maximum available lateral tyre force according to the rear longitudinal tyre force demand. One of the distinctive features of this work is the use of the envelope boundary concept – originally found in the aerospace industry – to set the state constraints for the optimization problem: the yaw rate bounds are imposed according to the maximum available lateral tyre force, while for the sideslip angle bound the rear slip angle is used, the latter set in such a way because according to the authors the rear slip angle scales naturally with speed while also accounts for higher yaw rates. The optimization problem is then set to minimise the yaw rate and sideslip errors along with the control effort subject to the input constraints and the soft envelope boundary constraints. The sampling time is chosen at the low rate of 10ms with prediction and control horizons at 15 steps while delay compensation is also used by solving the optimization problem for the next time step, with the final solution deployed on the prototype EV using custom C-code. Simulation and experimental results using a slalom manoeuvre at a speed

of 10m/s on a loose surface show that the controller can successfully restrict the steering command from the driver when the yaw rate and sideslip angle limits are violated. The study in [15] shows a very interesting solution that emphasises the importance of using a 'tailor made' MPC formulation according to the specific vehicle configuration so that useful simplifications can be exploited without removing important nonlinear aspects in the model design. However, similarly to other limit-handling studies, the vehicle velocity is not directly controlled and is only taken into account in the setup of the envelope bounds, something that restricts the controller's authority in such cases.

In [34] a hybrid MPC and a switched MPC formulation for a yaw stability controller using an AFS system and differential wheel braking are presented, both formulations based on previous work from the same authors [16, 25]. Simulation results using the hybrid MPC formulation against a standard ESC strategy show that the first is faster to converge to the target yaw rate and slip angle targets with smaller overshoots. Since the complexity of the above hMPC makes it unsuitable for automotive-grade ECUs, an explicit switched MPC is presented next, which allows for a smaller sampling time of 50ms and online application. Experimental results on an RWD test vehicle under three different scenarios on a low-μ road with high speeds – so that limit-handing conditions are involved – show that the switched MPC controller can successfully stabilise the vehicle while keeping the tyre slip angles within the given limits.

Another example of an explicit MPC law can be found in [26], where a yaw control strategy using a rear active differential is presented. Here a single track model is used as the internal model for formulating the MPC strategy, whereas the current on the differential valves (mapped to Mz through a simple model) and the steering angle are taken as the inputs of the system, while yaw rate is taken as the output. On the other hand the yaw rate reference is set according to the desired improvement on the understeer characteristics of the vehicle. The optimization problem is then constructed, so that to minimise the yaw

rate error along with the control effort, subject to the input and the sideslip angle constraints. An extra yaw rate constraint is also set explicitly in the yaw rate reference static map. The resulted NMPC problem is then solved using the 'nearest point' approach: a number of optimal control sequences is computed offline with the online approximate solution picked by finding the nearest offline computed point. For simulation, the authors choose to constrain the sideslip angle to 5degs and the control current to 1A, while the prediction and control horizons are set to 100 and 5 steps respectively with a sampling time of 0.01s. The number of points computed offline is 5.5×10^5 for a rather limited set of variables: yaw rate was varied between -28 and 28deg, sideslip angle and steering angle between -5.7 and 5.7degs and velocity between 79.2 and 118.8km/h. Simulation results show a good agreement between the proposed approach and the nominal NMPC, but with some chattering. This could be potentially corrected with a higher number of offline computed points, but at higher memory and computational costs, which shows that there is again a trade-off between performance and solution complexity.

5.3 Linear MPC Formulation

From the above section 5.2 it is obvious that while MPC is an attractive control strategy especially when constraints are involved, it also has numerous drawbacks. Careful consideration is therefore needed when designing the MPC controller in relation to:

- The internal model: choosing a larger, nonlinear model increases the number of optimisation variables and the problem complexity.
- The sampling time: longer time steps reduce the number of optimisation variables for a fixed horizon but can result in slow, ineffective control actions.
- The prediction and control horizons: shorter horizons reduce the number of optimi-

sation variables for a fixed sampling time but can also result in ineffective control actions.

- The constraints: more constraints and nonlinear state and/or input constraints increase the problem complexity, but linear or linearised constraints can fail to capture the nature of the original limits.

- The weighting matrices: like any other optimal control problem which is based on the minimisation of a standard quadratic cost function, the relative weights in the cost function are tuning parameters to be chosen.

There is therefore a clear trade-off between performance and computational effort attached to both the choice of the internal model for the MPC and the tuning of the related parameters, which in the case of a vehicle control strategy as considered here with its relatively fast dynamics need to be carefully chosen.

Based on these observations, in this chapter we construct a linear MPC framework to be used in the linear MPC strategies in the sections to follow. Starting from the nonlinear continuous-time dynamical system

$$\dot{x} = f_c(x,u), \tag{5.1}$$

linearised about the equilibrium point (x^{ss}, u^{ss})

$$\dot{x} = A^{ss}x + B^{ss}u - (A^{ss}x^{ss} + B^{ss}u^{ss}), \tag{5.2}$$

with associated cost function state and input weighting matrices Q_c and R_c respectively and cross-weighting matrix M_c, the discrete-time model using an exact discretisation [6]

and sampling time T_s is

$$x_{k+1} = Ax_k + Bu_k + c, \tag{5.3}$$

with

$$c = -\int_0^{T_s} e^{A^{ss}\eta} \mathrm{d}\eta (\mathrm{A^{ss}x^{ss}} + \mathrm{B^{ss}u^{ss}}),$$

assuming that the input u and the disturbance term $(A^{ss}x^{ss} + B^{ss}u^{ss})$ both remain constant for the discretisation interval [46].

Then the MPC regulation problem with horizon $N = N_p = N_u$ is

$$\begin{aligned}
\min_{x,u} \quad & (x_N - r)^T S_d (x_N - r) + \sum_{k=0}^{N-1} \Big[(x_k - r)^T Q_d (x_k - r) \\
& + (u_k - l)^T R_d (u_k - l) + 2 (x_k - r)^T M_d (u_k - l) \Big], && \text{(5.4a)} \\
\text{subject to} \quad & x_0 = x_{in}, && \text{(5.4b)} \\
& x_{k+1} = Ax_k + Bu_k + c, \quad k = 0, 1, ..., N-1, && \text{(5.4c)} \\
& u_k^l \leq u_k \leq u_k^h, \qquad k = 0, 1, ..., N-1, && \text{(5.4d)} \\
& x_k^l \leq x_k \leq x_k^h, \qquad k = 1, 2, ..., N, && \text{(5.4e)}
\end{aligned}$$

where (5.4a) is the cost to minimise with r and l the state and input references respectively, (5.4b) sets the initial state x_0 equal to the current one, (5.4c) are the affine discrete system dynamics and (5.4d)-(5.4e) are the state and input inequality constraints. The positive (semi-)definite matrix Q_d and positive definite matrix R_d are the weighting matrices on the state error and control effort respectively, and the positive definite matrix M_d is the cross-weighting matrix. A terminal penalty $(x_N - r)^T S_d (x_N - r)$ is also included, with the matrix S_d selected as the solution of the Discrete Algebraic Riccati Equation (DARE)

$$S_d = A^T S_d A + Q_d - (B^T S_d A + M_d^T)^T (R_d + B^T S_d B)^{-1} (B^T S_d A + M_d^T).$$

Based on the standard linear MPC problem (5.4) a dense MPC formulation using soft constraints on the state is used in this chapter to avoid infeasibility problems (please refer to Appendix C for details on the derivation of the dense soft-constrained MPC formulation), with the necessary A and B matrices updated at each time step according to the current steering command from the driver and the current vehicle velocity using the analysis of section 3.3. The resulting QP problem is then solved using the active-set method as available through the `quadprog` command in MATLAB.

5.4 Linear MPC Strategies

One of the main disadvantages of using an MPC strategy for controlling a system is its computational burden, which is directly related to the time that is needed to construct and solve the MPC problem (5.4). As already mentioned in the above sections, many factors have a decisive role in this: the number of optimization variables and the number of constraints, along with the selected sampling time and horizon can result in a large optimization problem that is too difficult to solve online. To this end, in the following we present and tune two MPC strategies using internal models of different complexity:

1. The first MPC strategy, called hereafter 'MPCt' (where 't' stands for 'torque' input), uses the full four-wheel vehicle model (3.2) hence both the vehicle dynamics and the much faster wheel speed dynamics are included in the internal model. The input is set as the two torques on the rear wheels.

2. The second MPC strategy, called hereafter 'MPCs' (where 's' stands for 'slip' input), neglects the wheel speed dynamics (3.2d) from the internal model, while the input is set as the longitudinal slip at the rear wheels. Then a Sliding Mode Slip Controller is used to calculate the necessary torques on the rear wheels according

to the requested longitudinal slips.

5.4.1 MPCt: MPC using Wheel Torque Inputs

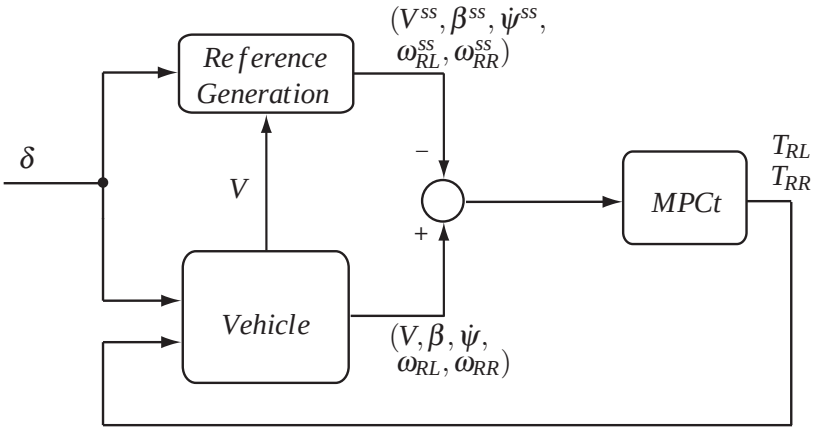

Figure 5.2: MPCt control structure.

For the MPCt the full four-wheel model (3.2) is used, hence (neglecting the free-rolling front wheels) we set $x = [V\ \beta\ \dot{\psi}\ \omega_{RL}\ \omega_{RR}]^T$, and $u = [T_{RL}\ T_{RR}]^T$ (Fig. 5.2).

When defining the optimal control problem, the cross-weighting matrix M_c is set to zero (note that after discretisation of the problem, M_d in (5.4a) will usually not be zero), while Q_d and R_d are the discrete equivalents of the continuous-time weighting matrices

$$Q_c = \text{diag}\left\{ q_V \left(\frac{1}{V_{max}(\delta)}\right)^2, \quad \left(\frac{1}{\beta_{max}(\delta)}\right)^2, \quad \left(\frac{1}{\dot{\psi}_{max}(\delta)}\right)^2, \right. \\ \left. \left(\frac{1}{\omega_{RL_{max}}(\delta)}\right)^2, \quad \left(\frac{1}{\omega_{RR_{max}}(\delta)}\right)^2 \right\}, \tag{5.5}$$

$$R_c = \text{diag}\left\{ \left(\frac{1}{T_{RL_{max}}}\right)^2, \quad \left(\frac{1}{T_{RR_{max}}}\right)^2 \right\}, \tag{5.6}$$

where, similarly to (4.8)-(4.9), the Q_c and R_c matrices are normalised with respect to the maximum expected state and input values, and the only tuning parameter is q_V. Note that

the use of state constraints in the case of the MPCt (and MPCs) strategy reduces somewhat the importance of tuning the q_V parameter: large oscillations in the yaw rate and sideslip angle response are avoided as part of the constrained optimal control problem.

5.4.1.1 State Constraints

In order to avoid large yaw rate values, a yaw rate constraint according to the current velocity V_{in} is imposed at the beginning of the optimization and fixed throughout the prediction horizon. This constraint is based on the lateral acceleration limit for the current velocity and is coupled to the tyre/road friction coefficient μ_{max} [113]:

$$|\dot{\psi}| \leq \mu_{max} g / V_{in}. \tag{5.7}$$

Following [11, 78], a constraint on the maximum sideslip angle is also set for subjective feel according to the current velocity:

$$|\beta| = \begin{cases} 2\dfrac{k_1 - k_2}{V_{char}^3} V_{cur}^3 - 3\dfrac{k_1 - k_2}{V_{char}^2} V_{in}^2 + k_1, & \text{if} \quad V_{in} < V_{char} \\ k_2, & \text{if} \quad V_{in} \geq V_{char} \end{cases} \tag{5.8}$$

where V_{char} is the characteristic speed of the vehicle [50] (refer to Appendix E for the calculation of V_{char} used in this work). The positive constants k_1 and k_2 are tuning parameters, chosen at $10\pi/180$ and $3\pi/180$ respectively. No constraints on the velocity or the rear wheel speeds are imposed.

The yaw rate and sideslip angle constraints (5.7)-(5.8) are softened by introducing two slack variables $\varepsilon_{\dot{\psi}}, \varepsilon_{\beta} \in \mathbb{R}^+$ in the cost function 5.4a. In this way the maximum violation for the two states within the prediction horizon is penalised and infeasibility problems in the solution of 5.4 are avoided (please refer to Appendix C for details on how the soft

constraints are implemented).

5.4.1.2 Input Constraints

For the MPCt the use of the two torques on the rear wheels as input of the internal model gives us the opportunity to set constraints on them based on the static torque map of the motors used.

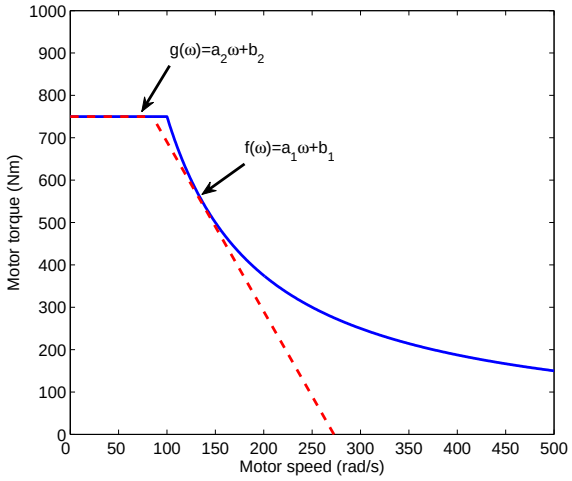

Figure 5.3: The static torque map and its approximation using affine functions of the wheel speed ω.

The maximum torque achievable on each of the two rear wheels of the car is a nonlinear function of the corresponding wheel speed. Since the MPC problem (5.4) is formulated as a convex optimization problem that allows only for affine inequality constraints, the static torque map is approximated by two affine functions of ω, as seen in Fig. 5.3. Taking for example the line $f(\omega) = a_1\omega + b_1$, we want

$$T_{Rj} \leq a_1\omega_{Rj} + b_1,$$

and expanding then to both the rear wheels' torques we get

$$\begin{bmatrix} 0 & 0 & 0 & -a_1 & 0 \\ 0 & 0 & 0 & 0 & -a_1 \end{bmatrix} \begin{bmatrix} V \\ \beta \\ \dot{\psi} \\ \omega_{RL} \\ \omega_{RR} \end{bmatrix} + \begin{bmatrix} T_{RL} \\ T_{RR} \end{bmatrix} \leq \begin{bmatrix} b_1 \\ b_1 \end{bmatrix}.$$

A similar procedure can be followed for line $g(\omega) = a_2\omega + b_2$. The resulting polyhedron, as seen in Fig. 5.3, is convex and can be therefore used to define the input inequality constraints in (5.4).

In this work, the above piecewise linear approximation of the static torque map is chosen in such way so that the error from the nonlinear constraint is minimised at a realistic range of wheel speeds. To this end, we choose a_2 and b_2 so that $g(\omega)$ coincides with the constant torque line (note that in this case $b_2 = 0$), and a_1 and b_1 so that $f(\omega)$ is tangent to the constant power curve and meets the longitudinal line at the high wheel speed of 270rad/s.

5.4.1.3 Longitudinal Slip Constraints

Since, for stability reasons, it is deemed necessary to constrain the longitudinal slips on the rear wheels, another constraint on the state is also constructed for the MPCt to address this. If, according to the simplified MF definition (3.7), the maximum longitudinal force on the wheel is

$$f_{Rjx}^{max} = f_{Rjz} D_{MF} sin\left(C_{MF} tan^{-1}(B_{MF} s_{Rjx}^{max})\right), \tag{5.9}$$

then, assuming steady-state conditions

$$T_{Rj}^{max} = f_{Rjx}^{max} R_w, \tag{5.10}$$

and the longitudinal slip based limit on the motor torque can be computed as

$$T_{Rj}^{max} = f_{Rjz} D_{MF} \sin\left(C_{MF} \tan^{-1}(B_{MF} s_{Rjx}^{max})\right) R_w. \tag{5.11}$$

5.4.2 MPCs: MPC Neglecting the Wheel Speed Dynamics

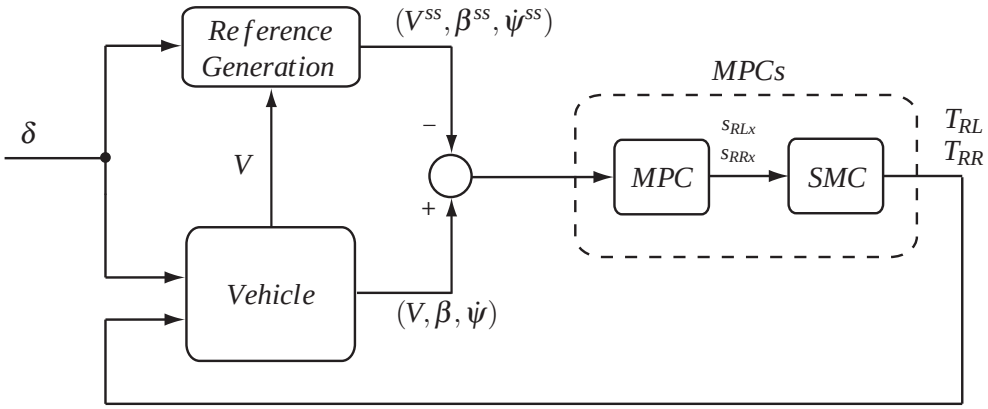

Figure 5.4: MPCs control structure.

The second MPC strategy neglects the fast wheel speed dynamics, so that a simpler internal model is used with $x = [V\ \beta\ \dot{\psi}]^T$ and $u = [s_{RLx}\ s_{RRx}]^T$. Then a Sliding Mode Slip Controller computes the necessary torques on the rear wheels based on the requested longitudinal slips (Fig. 5.4). When defining the optimal control problem, the cross-weighting matrix M_c is set again to zero, while Q_d and R_d are found again from the continuous time weighting matrices Q_c and R_c, in a way similar to the MPCt strategy (5.5)-(5.6):

$$Q_c = \text{diag}\left\{ q_V \left(\frac{1}{V_{max}(\delta)}\right)^2, \quad \left(\frac{1}{\beta_{max}(\delta)}\right)^2, \quad \left(\frac{1}{\dot{\psi}_{max}(\delta)}\right)^2 \right\}, \tag{5.12}$$

$$R_c = \text{diag}\left\{ \left(\frac{1}{s_{RLx_{max}}(\delta)} \right)^2, \quad \left(\frac{1}{s_{RRx_{max}}(\delta)} \right)^2 \right\}. \tag{5.13}$$

5.4.2.1 State, Input and Torque Constraints

For the MPCs we use the same yaw rate and sideslip angle constraints (5.7)-(5.8) as with the MPCt, while no constraint is set on the vehicle velocity.

Constraints are also set for the input $u = [s_{RLx}\ s_{RRx}]^T$ so that the longitudinal slips on the rear wheels never exceed the maximum allowable slip for safe operation of the vehicle. Using the tyre parameters as found in Table A.1 for the simplified MF (3.7) we set the constraint (Appendix A)

$$|s_{Rjx}| \leq 0.15. \tag{5.14}$$

For the MPCs we can not directly account for the motor limits in the form of its static torque map as was the case with the MPCt. We therefore construct an additional constraint on the state and input in order to avoid excessive torque requests from the two motors. If the maximum torque that can be provided by a motor is T_{Rj}^{max}, then the maximum longitudinal force on the wheel – assuming steady-state conditions – is

$$f_{Rjx}^{max} = T_{Rj}^{max}/R_w, \tag{5.15}$$

and using the reverse MF the torque based limit on the longitudinal slip on the tyre can be computed as

$$s_{Rjx}^{max} \leq \frac{1}{B_{MF}} \tan\left(\frac{1}{C_{MF}} \sin^{-1}\left(\frac{f_{Rjx}^{max}}{D_{MF}\, f_{Rjz}} \right) \right). \tag{5.16}$$

Then, we can compare the two limits (5.14) and (5.16) and set the input constraints at

the beginning of the prediction horizon as

$$|s_{Rjx}| \leq \min(0.15, s_{Rjx}^{max}). \tag{5.17}$$

5.4.2.2 Sliding Mode Slip Controller

The torque demand on the two electric motors according to the longitudinal slip requests are then calculated using a Sliding Mode Slip Controller, constructed in a way similar to [61, 142].

From the longitudinal slip definition (3.3) the slip dynamics are

$$\dot{s}_{ijx} = \frac{\mathrm{d}}{\mathrm{dt}}\left(\frac{V_{ijx} - \omega_{ij}R_w}{\omega_{ij}R_w}\right) = \frac{\dot{V}_{ijx}\omega_{ij}R_w - V_{ijx}\dot{\omega}_{ij}R_w}{\omega_{ij}^2 R_w^2} = \frac{\dot{V}_{ijx}}{\omega_{ij}R_w} - \frac{V_{ijx}\dot{\omega}_{ij}}{\omega_{ij}^2 R_w},$$

and using (3.3) and (3.2d),

$$\dot{s}_{ijx} = (s_{ijx}+1)\frac{\dot{V}_{ijx}}{V_{ijx}} - (s_{ijx}+1)^2\frac{R_w}{I_w V_{ijx}}(T_{ij} - f_{ijx}R_w).$$

Setting the sliding surface as $e = s_{ijx} - s_{ijx}^{des}$ and using $\mathscr{V} = (1/2)e^2$ as a Lyapunov function candidate with $\dot{e} = \dot{s}_{ijx}$ (assuming that s_{ijx}^{des} remains constant), we have [77]

$$\begin{aligned}\frac{\mathrm{d}\mathscr{V}}{\mathrm{dt}} &= e\dot{e} = e\dot{s}_{ijx} = e\left((s_{ijx}+1)\frac{\dot{V}_{ijx}}{V_{ijx}} - (s_{ijx}+1)^2\frac{R_w}{I_w V_{ijx}}(T_{ij} - f_{ijx}R_w)\right)\\ &= e\left((s_{ijx}+1)\frac{\dot{V}_{ijx}}{V_{ijx}} - (s_{ijx}+1)^2\frac{R_w}{I_w V_{ijx}}T_{ij} + (s_{ijx}+1)^2\frac{R_w}{I_w V_{ijx}}f_{ijx}R_w)\right),\end{aligned}$$

and taking

$$\begin{aligned}T_{ij} &= -\frac{I_w V_{ijx}}{(s_{ijx}+1)^2 R_w}\left(-(s_{ijx}+1)\frac{\dot{V}_{ijx}}{V_{ijx}} - (s_{ijx}+1)^2\frac{R_w}{I_w V_{ijx}}f_{ijx}R_w - \zeta\,\mathrm{sgn}(e)\right)\\ &= \frac{I_w\dot{V}_{ijx}}{(s_{ijx}+1)R_w} + R_w f_{ijx} + \frac{I_w V_{ijx}}{(s_{ijx}+1)^2 R_w}\zeta\,\mathrm{sgn}(e),\end{aligned}$$

with ζ a small positive number yields

$$\frac{\mathrm{d}\mathscr{V}}{\mathrm{dt}} = -e\zeta\,\mathrm{sgn}(e) = -\zeta|e| < 0.$$

Then defining $\kappa = \dfrac{I_w V_{ijx}}{(s_{ijx}+1)^2 R_w}\zeta$, the control law is

$$T_{ij} = \frac{I_w \dot{V}_{ijx}}{(s_{ijx}+1)^2 R_w} + R_w f_{ijx} + \kappa\,\mathrm{sgn}(e),$$

or to reduce chattering we can use instead

$$T_{ij} = \frac{I_w \dot{V}_{ijx}}{(s_{ijx}+1)^2 R_w} + R_w f_{ijx} + \kappa\,\mathrm{sat}\left(\frac{e}{\Delta}\right),$$

where $\mathrm{sat}(\cdot)$ the saturation function

$$\mathrm{sat}(y) = \begin{cases} y, & \text{if } |y| \leq 1 \\ \mathrm{sgn}(y), & \text{if } |y| > 1 \end{cases}$$

and Δ a positive constant [77].

5.5 Sampling Time and Horizon Selection

After choosing the internal model for the MPC problem (5.4), two of the most important parameters affecting both the performance and computational burden for an MPC formulation are the sampling time T_s and the horizon N. These two parameters are directly connected to the construction of the discrete-time finite-horizon cost function (5.4a) and the discrete-time dynamics (5.4c), and their choice must satisfy the minimum require-

ment for the MPCt and MPCs: both strategies should perform similar to an unconstrained continuous-time optimal strategy when no inequality violations occur.

For the evaluation of the performance of the two MPC strategies we use the closed-loop cost, defined as the summation of the running cost

$$J_{cl} = \sum_{k=0}^{\left\lceil \frac{T_{sim}-T_s}{T_s} \right\rceil} (x_k - r)^T Q_d (x_k - r) + (u_k - l)^T R_d (u_k - l) + 2 (x_k - r)^T M_d (u_k - l),$$

where T_{sim} is the chosen simulation time and $\lceil \cdot \rceil$ is the ceiling function, which maps a real number to the smallest following integer. The above expression is the summation of the weighted square of the state error and the control effort for the duration of the simulation, hence the cost that the MPC tries to minimise at the first place, and can be therefore used as a metric of the controller's performance. For the evaluation of the computational effort, the total computational time $T_{comp} = T_{constr} + T_{sol}$ required to construct and solve the MPC problem employing the `quadprog` solver in MATLAB is used.

First we investigate the effect of varying the sampling time T_s by comparing the two MPC strategies with an unconstrained continuous-time optimal strategy for a range of sampling times and a horizon equal to 8s. A set of simple simulation scenarios is used, whereas the vehicle is going straight and a step steer input is applied after 2s for the duration of 8s. For each simulation, the initial vehicle velocity is chosen so that it is 1m/s higher from the maximum velocity allowable for the applied step steering input V_{max} hence both the MPC strategies will regulate the velocity, sideslip angle and yaw rate of the vehicle according to the reference values, as discussed in section 3.3. It is assumed at this point that there are no acceleration or braking requests from the driver.

5.5.1 Impact of Varying the Sampling Time in the MPCt

For the MPCt, using a sampling time above 0.035s results in a controller that cannot be stabilising anymore. This is the direct result of including the fast wheel speed dynamics (3.2d) in the internal model, and reveals the main disadvantage of this strategy: consideration of the wheel speed dynamics in the MPC problem not only increases the number of optimization variables but at the same time calls for faster sampling times.

Using the set of test scenarios described above, Fig. 5.5a shows the closed-loop cost for a range of step steering inputs and sampling times between 0.01-0.035s. No major variations are noticed for this range of sampling times. On the other hand, in Fig. 5.5b we observe that for sampling times below 0.02s, the time needed to solve the QP problem increases exponentially. The pareto frontiers in Fig. 5.5c show a similar trend, with computational times increasing rapidly with only small gains in the closed-loop cost.

Fig 5.6 shows the velocity and sideslip angle time histories for a step steering input of 6deg and sampling times of 0.01s and 0.035s. As we can see, only a small degradation in performance can be seen for a sampling time of 0.035s. Based on the above analysis we therefore set the sampling time for the MPCt strategy to T_s =0.035s.

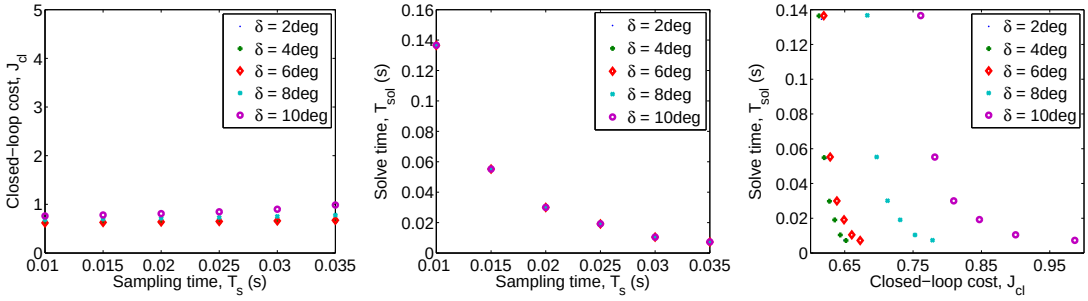

(a) (b) (c)

Figure 5.5: Variation of closed-loop cost and computational time with sampling time for a range of step steering inputs in the MPCt strategy.

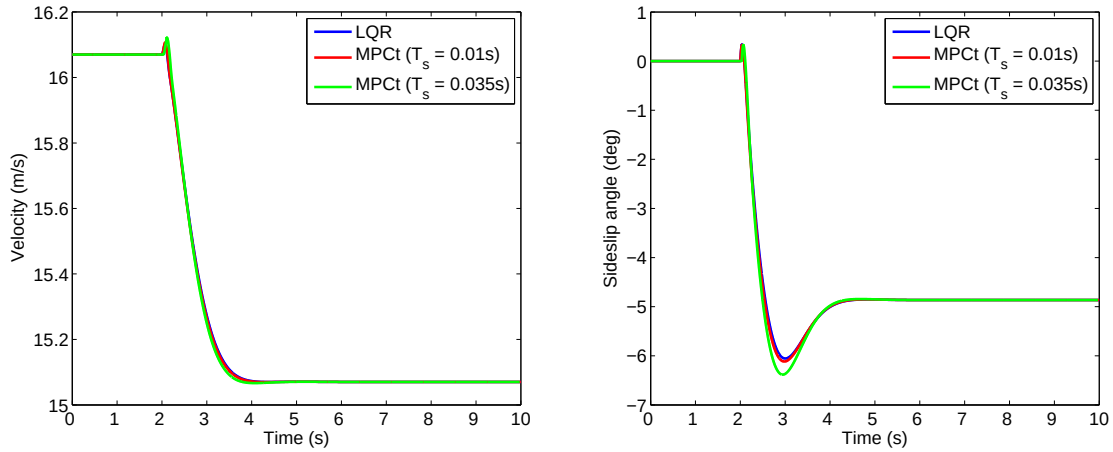

(a) Velocity (b) Sideslip angle

Figure 5.6: Velocity and sideslip angle time histories for a step steering input of 6deg, a horizon of 8s and different sampling times in the MPCt.

5.5.2 Impact of Varying the Sampling Time in the MPCs

Using the same set of test scenarios as in the case of the MPCt, Fig. 5.7a shows the variation of the closed-loop cost with sampling time for a range of step steer inputs for the MPCs. No considerable changes in performance for sampling times below 0.1s can be noticed. On the other hand, in Fig. 5.7b we observe that the solve time increases rapidly for sampling times below 0.05s, so there is a clear trade-off between closed-loop cost and

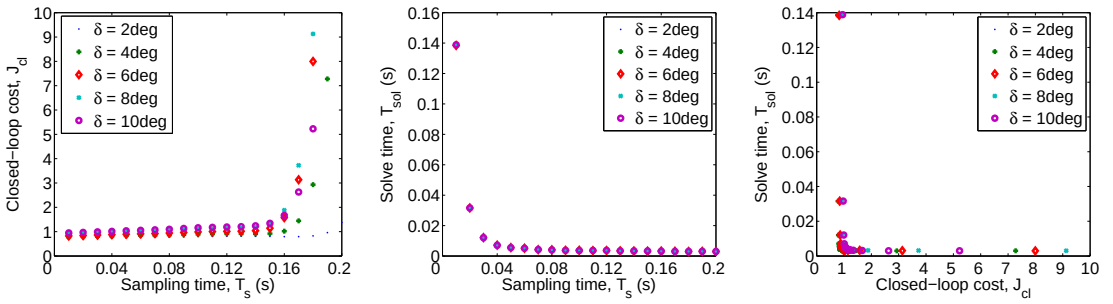

(a) (b) (c)

Figure 5.7: Variation of closed-loop cost and computational time with sampling time for a range of step steering inputs in the MPCs strategy.

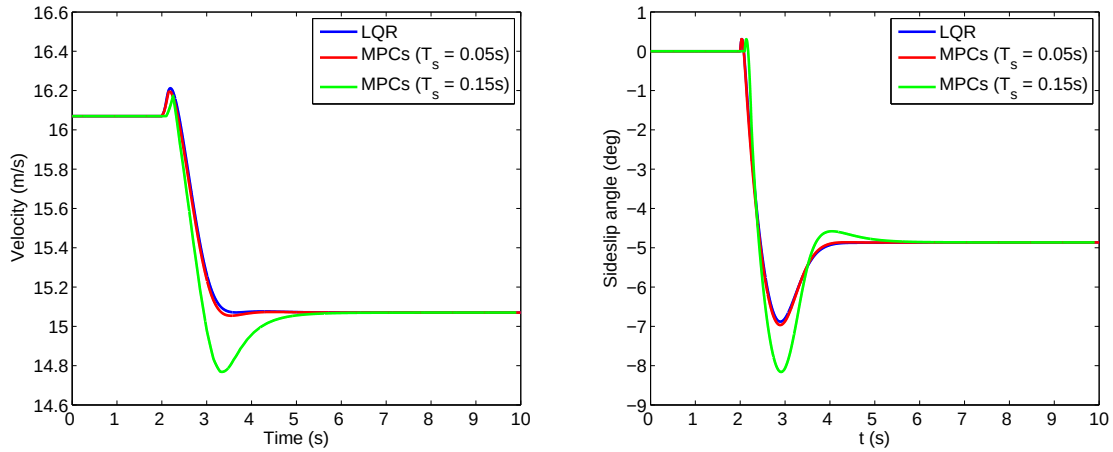

(a) Velocity (b) Sideslip angle

Figure 5.8: Velocity and sideslip angle histories for a step steering input of 6deg, a horizon of 8s and different sampling times in the MPCs.

solve time with changes in the sampling time, while a similar increase in the solve time can be noticed for small reductions in the closed-loop cost below 1 (Fig. 5.7c).

The difference in the system response for a step steering input of 6deg and sampling times of 0.05s and 0.15s can be seen in Fig. 5.8. It can be confirmed that for shorter sampling times the response of the system using the MPCs strategy is close to the one with the LQR, while it differs considerably as we increase the sampling time to 0.15s. Based on the above analysis we therefore set the sampling time for the MPCs strategy to T_s =0.05s.

5.5.3 Impact of Varying the Horizon

The long horizon length in combination with the short sampling times used in the above sections resulted in long computational times, a large portion of which was spend in constructing the matrices for the dense MPC problem. The increase in construction time with longer horizons in the MPCt and MPCs can be seen in Fig. 5.9. We also note that the

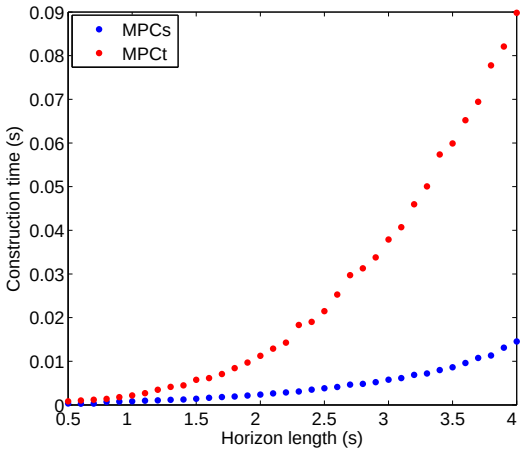

Figure 5.9: Construction time versus sampling time for the two MPC strategies.

relevant increase in construction time for the MPCs is lower than the one for the MPCt, a result of the smaller number of optimization variables used in the MPCs. However, in both strategies the construction time drops to values as low as 2ms for horizons less than 1s, so we set the horizon for both strategies to N =1s. It is also interesting to note here that the impact of a shorter horizon length on the closed-loop cost was observed to be minimal for the simple step steering input scenario used in this section.

5.5.4 Impact of Varying the Control Horizon

Having established the correct combination of sampling time and horizon for the two MPC strategies, we next examine the effect of shortening the control horizon N_u while keeping the prediction horizon fixed at N_p =1s so that the computational time is always below the sampling time in the presence of state and input inequality constraints. For this, we use a extreme manoeuvre in CarMaker, whereas the vehicle is going straight and a step steering input of -160deg is applied on the steering wheel at t =1s followed by a countersteer input of 260deg at t =2s, with the initial velocity of which is 3m/s higher

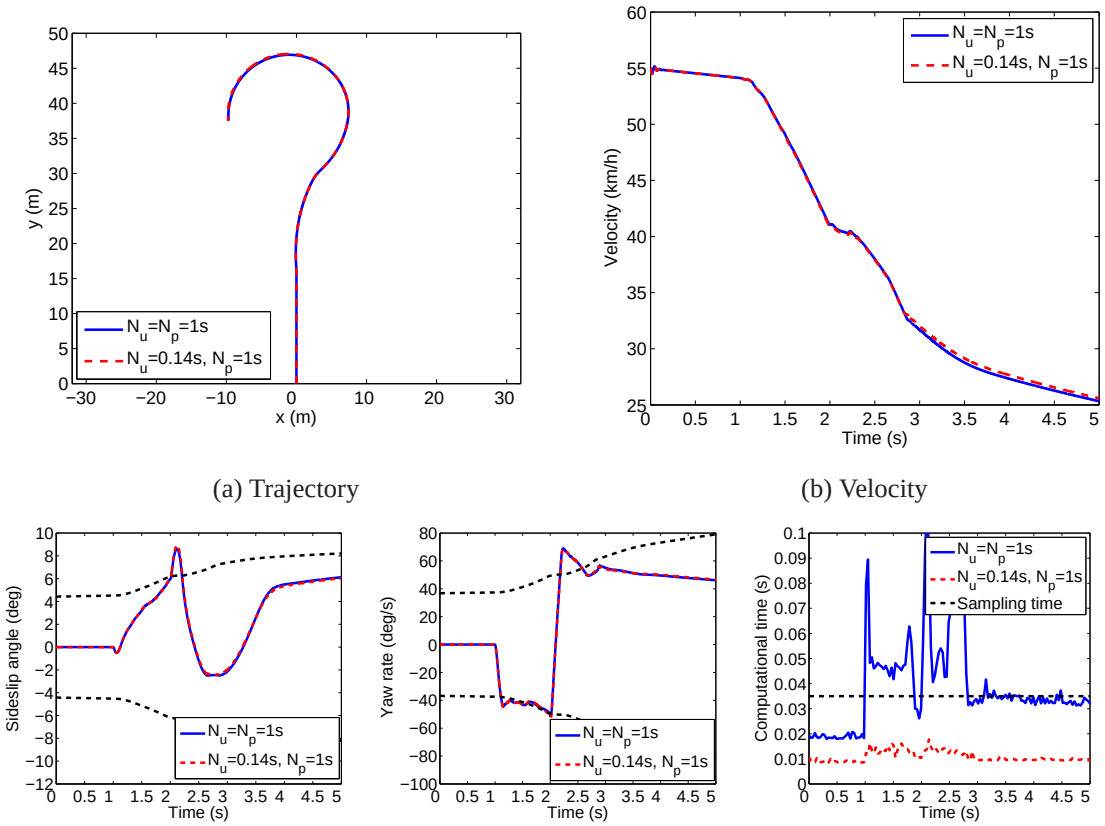

(a) Trajectory (b) Velocity

(c) Sideslip angle (d) Yaw rate (e) Comp. time

Figure 5.10: Impact of using a shorter control horizon in the MPCt.

than V_{max} for the first steering input.

As we can see from Fig. 5.10, in order to drop the computational time at levels below the sampling time of T_s =0.035s the control horizon needs to be reduced to N_u =0.14s (Fig. 5.10e), however no difference can be noticed in the vehicle trajectory (Fig. 5.10a) with the smaller control horizon. The small impact in performance can also be confirmed by the velocity, sideslip angle and yaw rate time histories (Fig. 5.10b-5.10d) which show no major differences when the shorter control horizon is used (constraints shown only for the shorter horizon case).

In the case of the MPCs, the relatively higher sampling time of $T_s = 0.05$s allows for a longer control horizon. Fig. 5.11e shows that reducing the control horizon to $N_u = 0.5$s

reduces the computational time without affecting the vehicle trajectory (Fig. 5.11a). No impact in the controller performance with the shorter control horizon can be noticed, as also evidenced in the velocity, sideslip angle and yaw rate time histories in Figs. 5.11b-5.11d (constraints shown only for the shorter horizon case). From Fig. 5.11e it is also interesting to note that, apart from two spikes at around 2.5s, the computational time is already lower than the sampling time even without the shorter control horizon.

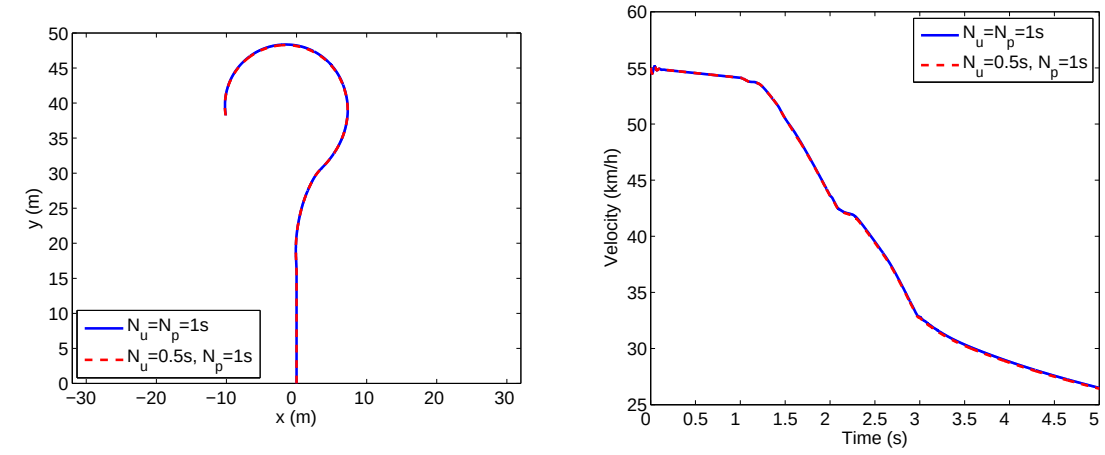

(a) Trajectory (b) Velocity

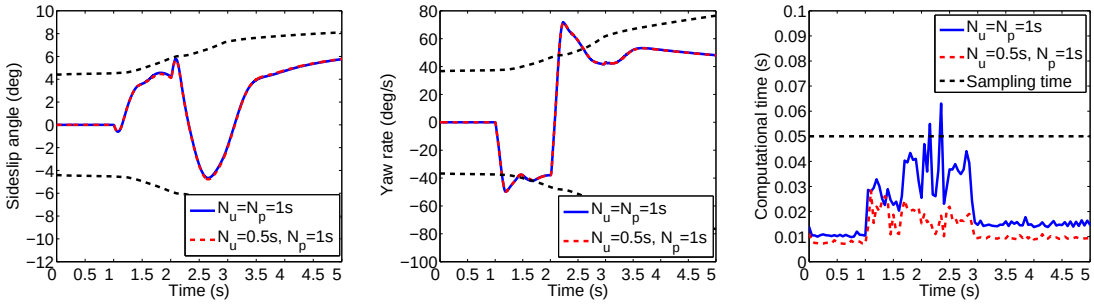

(c) Sideslip angle (d) Yaw rate (e) Comp. time

Figure 5.11: Impact of using a shorter control horizon in the MPCs.

5.6 Evaluation of the two MPC strategies

In the following section we compare the two MPC strategies against the LQR strategy from chapter 4 and a baseline vehicle with no active control in CarMaker environment. The first scenario under consideration examines the terminal understeer mitigation capabilities of the two MPC strategies and how these compare against the LQR intervention, while the second scenario tests the three optimal control strategies in a fast double lane change manoeuvre. The purpose of the two test scenarios is therefore to assess the relative advantages of using a constrained optimal control strategy against an unconstrained one under two limit handling manoeuvres. Note that we assume that no acceleration or deceleration commands come from the driver for the duration of the two manoeuvres while the actual torques applied on the rear wheels will be saturated according to the static torque map (Fig. A.1).

5.6.1 U-turn scenario

For the first simulation scenario, we use the same U-turn manoeuvre as the one used for the evaluation of the LQR strategy in section 4.4, whereas the driver model available in CarMaker is used to steer the vehicle around a U-turn on a dry road (μ_{max} =1) and the velocity error penalty in (4.8) and both (5.5) and (5.12) is set to q_V =150 as before in chapter 4.

Fig. 5.12a shows the trajectory of the vehicle using the MPCs in blue, the vehicle using the MPCt in purple, the vehicle using the LQR in red and the uncontrolled vehicle in green. The vehicles using the MPCt, MPCs and LQR strategies follow a similar trajectory in Fig. 5.12a, but looking at the state histories as seen in Figs. 5.12b-5.12e reveals some distinctive differences between the three controllers. While the velocity drop from the MPCt, MPCs and LQR is similar (Fig. 5.12c), the two MPC strategies manage to keep

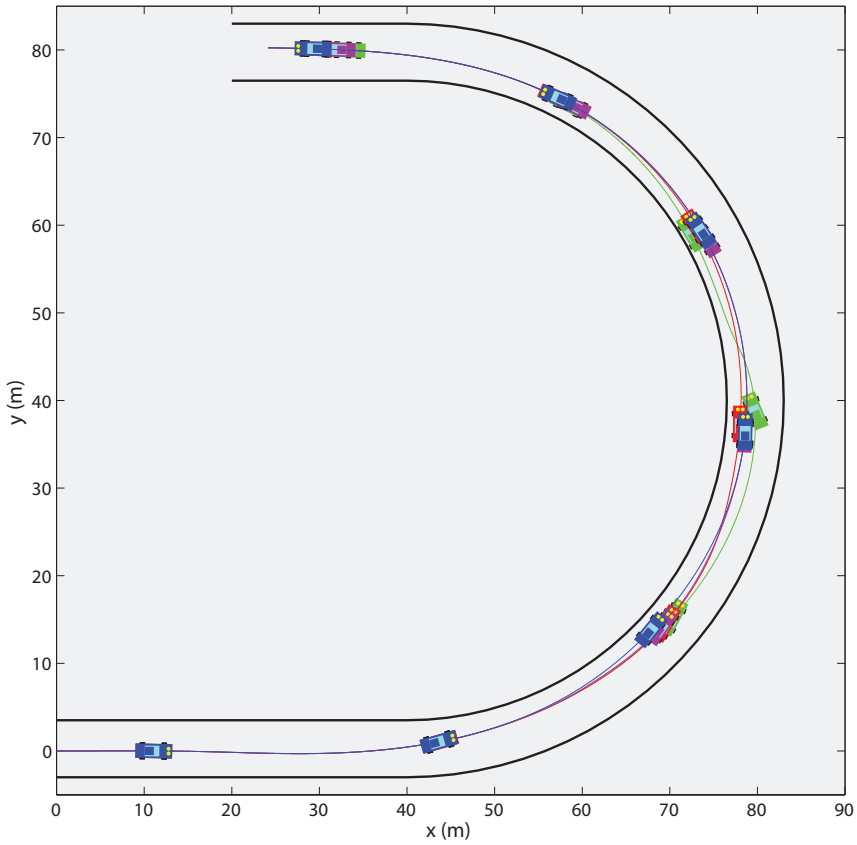

(a) Trajectory

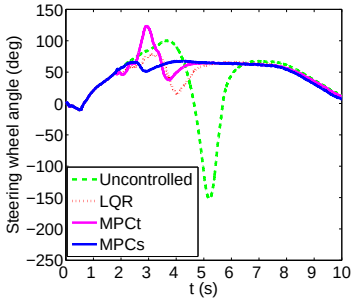

(b) Steering wheel angle

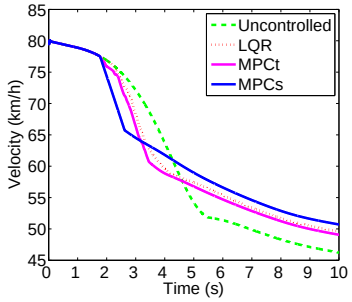

(c) Velocity

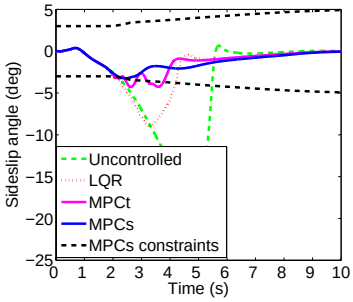

(d) Sideslip angle

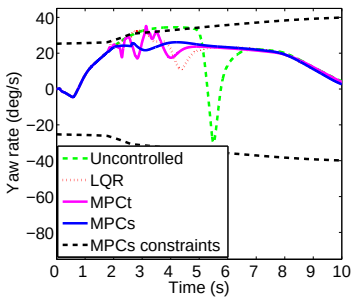

(e) Yaw rate

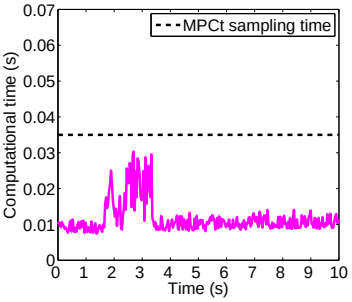

(f) MPCt comp. time

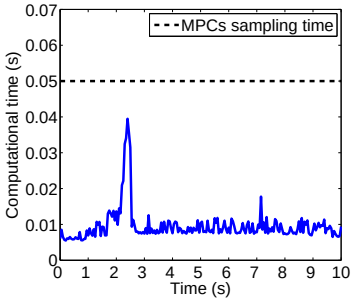

(g) MPCs comp. time

Figure 5.12: Comparison of the vehicle with the LQR (in red), the vehicle with the MPCt (in purple) and the vehicle with the MPCs (in blue) in the U-turn scenario.

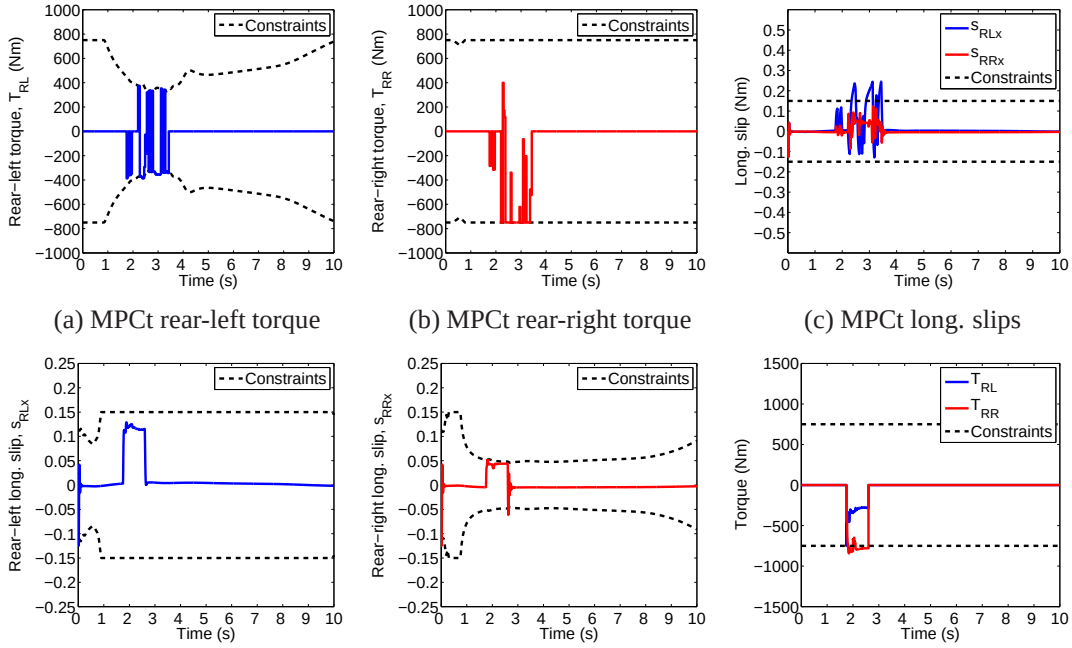

(a) MPCt rear-left torque (b) MPCt rear-right torque (c) MPCt long. slips

(d) MPCs rear-left long. slip (e) MPCs rear-right long. slip (f) MPCs torques

Figure 5.13: Torque (requested) and longitudinal slip (actual) time histories for the MPCt and the MPCs in the U-turn scenario.

the yaw rate and especially the sideslip angle (Figs. 5.12d-5.12e) of the vehicle at lower levels by enforcing the inequality constraints (5.7)-(5.8). It is also important to note at this point that these results have been achieved by the two MPC strategies while remaining within the corresponding sampling times (Figs 5.12f-5.12g).

Fig. 5.13 shows the rear wheel torque commands and the actual rear wheel longitudinal slips from the MPCt and the MPCs strategy. From Fig. 5.13a we can see that for the MPCt strategy the rear wheels' torque commands always remain within the input constraint for this strategy (5.11), however the rear-left wheel torque command is also constrained to lower values according to (5.11) whenever the longitudinal slip of the less loaded rear-left wheel exceeds the linear region of the operation of the tyre (Fig. 5.13c). For the MPCs strategy on the other hand (Figs. 5.13d-5.13f), it is the longitudinal slip of the rear-right that is constrained to lower values (Fig. 5.13e) according to (5.16) due to

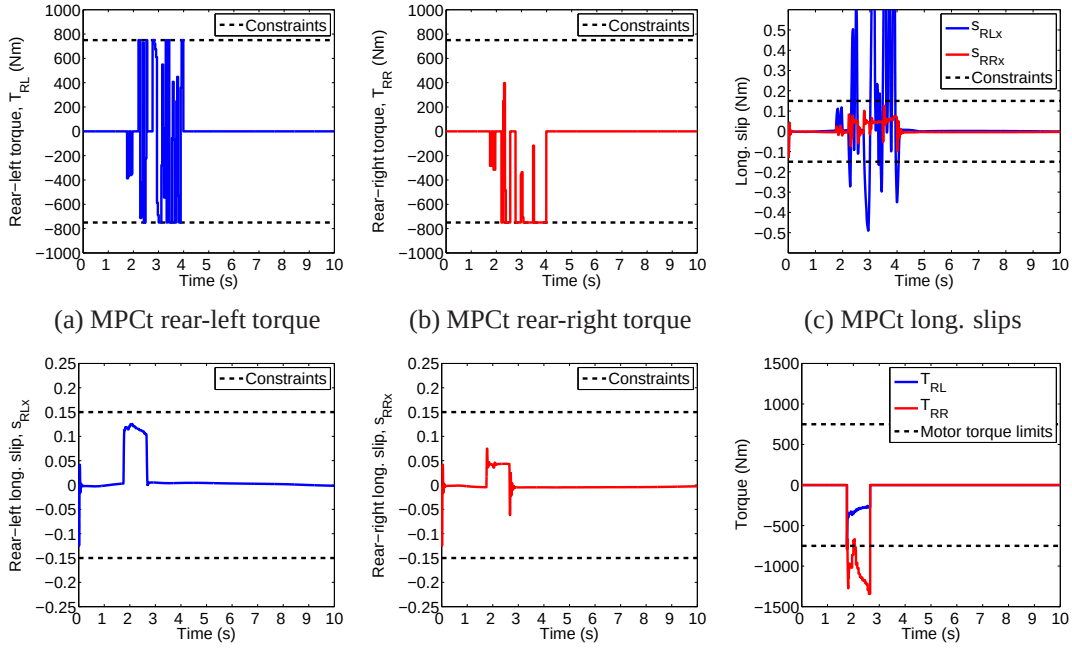

(a) MPCt rear-left torque (b) MPCt rear-right torque (c) MPCt long. slips

(d) MPCs rear-left long. slip (e) MPCs rear-right long. slip (f) MPCs torques

Figure 5.14: Torque (requested) and longitudinal slip (actual) time histories for the MPCt and the MPCs in the absence of constraints (5.11) and (5.16) respectively in the U-turn scenario.

the motor torque on this wheel reaching its limit (Fig. 5.13f). Another interesting point to note in Fig. 5.13 is the difference in the torque commands between the two MPC strategies, with the MPCt showing large oscillations for the rear-left torque (Fig. 5.13a) when compared to the smoother torque commands from the MPCs strategy (Fig. 5.13f).

In Fig. 5.14 we see what the rear wheel torque commands and the actual rear wheel longitudinal slips from the MPCt and the MPCs strategy would be in the absence of constraints (5.11) and (5.16) respectively. We remind that in the case of the MPCt the extra slip-based torque constraint is used for stability reasons, while in the case of the MPCs the extra torque-based slip constraint is used to account for the motor limits as imposed by its torque map. From Fig. 5.13 it is obvious that neglecting the extra input constraints would result in larger commands to the two electric motors from both MPC

strategies. In the case of the MPCt (Figs. 5.14a-5.14c) the absence of the slip-based torque constraint (5.11) results in large torque commands on the rear-left wheel (Fig. 5.13a), which also cause large longitudinal slip values on the rear-left tyre (Fig. 5.13c), while in the case of the MPCs (Figs. 5.14d-5.14f) the absence of the torque-based longitudinal slip constraint (5.16) results in large torque commands on the rear-right wheel (Fig. 5.13a) which far exceed the motor torque limits. We can conclude that the inclusion of the extra constraints (5.11) and (5.16) allows for both the tyre and electric motor limitations to be taken into account by the two MPC strategies, thus giving better knowledge of the complete system to the two controllers and resulting in more effective control actions.

From the U-turn scenario as analysed above, one could say that the MPCs and the MPCt strategies give a similar response to the simpler LQR. However the yaw rate regulation and most importantly the smaller sideslip angle values observed in the case of the MPCt and MPCs show that the same performance can be achieved without having to compromise the stability of the vehicle, a point that becomes important in a fast manoeuvre as the double-lane change presented next.

5.6.2 Double-Lane Change scenario

For the double-lane change scenario we use again the driver model available in CarMaker, but this time to follow a predefined path corresponding to a double-lane change manoeuvre as denoted by a dashed line in Fig. 5.15a. The road is assumed dry (μ_{max} =1) while the entry speed is set to the high value of 140km/h and the velocity error penalty in (4.8), (5.5) and (5.12) to q_V =150 as before. Note that no acceleration or deceleration commands come from the driver for the duration of the manoeuvre while the actual torques applied on the rear wheels are again saturated according to the static torque map (Fig. A.1).

Fig. 5.15a shows the trajectory of the vehicle using the MPCs in blue, the vehicle

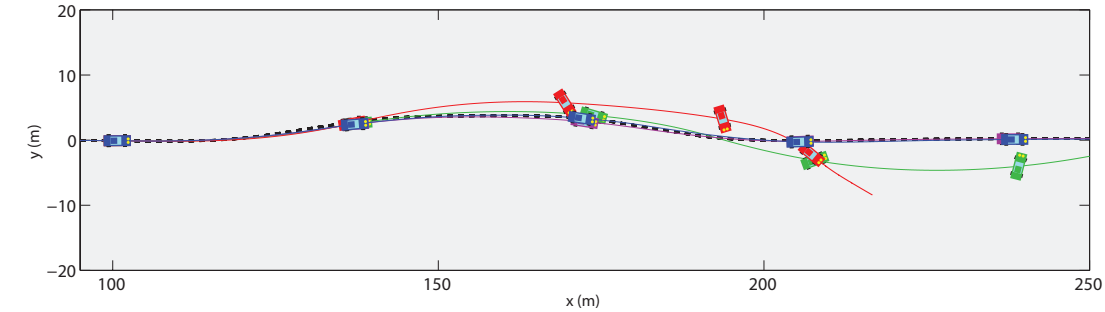

(a) Trajectory

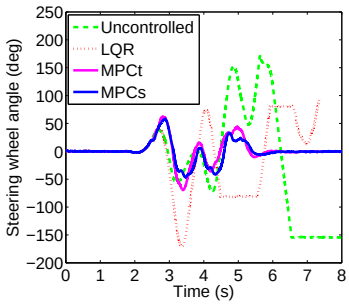

(b) Steering wheel angle

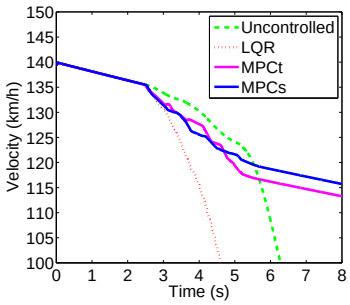

(c) Velocity

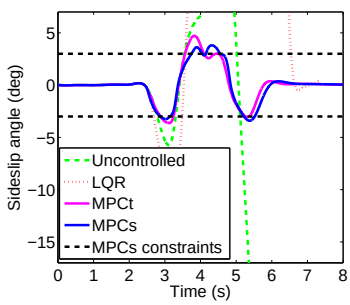

(d) Sideslip angle

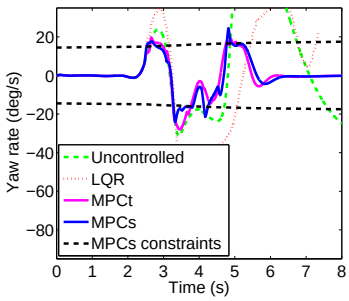

(e) Yaw rate

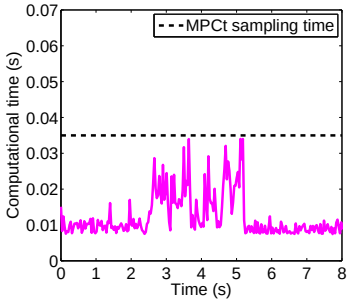

(f) MPCt comp. time

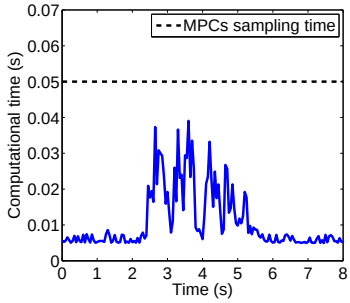

(g) MPCs comp. time

Figure 5.15: Comparison of the uncontrolled vehicle (in green), the vehicle with the LQR (in red), the vehicle with the MPCt (in purple) and the vehicle with the MPCs (in blue) in the double-lane change scenario.

using the MPCt in purple, the vehicle using the LQR in red and the uncontrolled vehicle in green. Both the uncontrolled vehicle and the vehicle with the LQR become unstable in this scenario and spin out of control, while the two MPC strategies successfully complete the test with minimal off-tracking from the predefined path. This is achieved by regulating the vehicle velocity as seen in Fig. 5.15c, while successfully constraining the sideslip angle and yaw rate of the vehicle (Figs. 5.15d-5.15e). Finally Fig. 5.15f and Fig. 5.15g show the computational times for the two MPC strategies, both remaining within the corresponding sampling times.

Fig. 5.16 shows the rear wheel torque commands and the actual rear wheel longitudinal slips from the MPCt and the MPCs strategy. Similarly to the U-turn scenario, for the MPCt strategy (Figs. 5.16a-5.16c) the rear torque commands are constrained according to (5.9), along with (5.11) and the changes in the maximum achievable longitudinal force

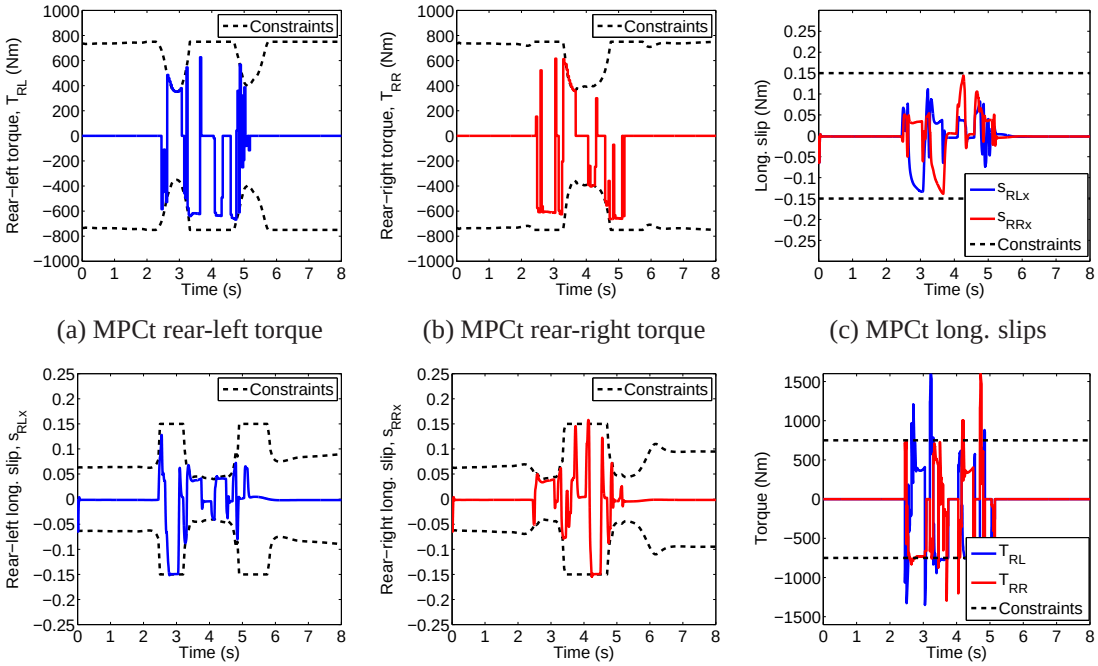

(a) MPCt rear-left torque (b) MPCt rear-right torque (c) MPCt long. slips

(d) MPCs rear-left long. slip (e) MPCs rear-right long. slip (f) MPCs torques

Figure 5.16: Torque (requested) and longitudinal slip (actual) time histories for the MPCt and the MPCs in the double-lane change scenario.

on the rear tyres due to lateral load transfers occurring throughout the double-lane change manoeuvre. For the MPCs strategy (Figs. 5.16d-5.16f) both the rear wheel longitudinal slips are constrained according to (5.17) which takes into account violation of the motor torque limits (Fig. 5.13f). Despite the spikes observed (Fig. 5.13f) for the MPCs case, the effectiveness of the two extra constraints can be again confirmed.

From the double-lane change scenario as analysed above, we see that both the MPCt and the MPCs strategies can stabilise the vehicle under a fast double-lane change manoeuvre. The uncontrolled vehicle does not complete the test successfully while the use of the LQR results in an equally unstable behaviour due to the excessive yaw rate and sideslip angle values.

5.7 Summary

Two MPC strategies of different complexity for combined yaw, sideslip and velocity regulation have been presented in this chapter. The first strategy, called MPCt, uses an internal model that includes both the vehicle dynamics and the much faster wheel speed dynamics as the state and the torque on the rear wheels as the input. The second strategy, called MPCs, neglects the wheel speed dynamics, hence uses only the vehicle dynamics as the state and the longitudinal slip on the rear wheels as the input for the internal model, with a Sliding Mode Slip Controller then calculating the necessary torques on the rear wheels. An analysis of the relative trade-off in closed-loop performance and computational cost for the two MPC strategies shows that inclusion of the fast wheel speed dynamics in the MPC formulation results not only in a bigger optimization problem but also requires faster sampling times.

Simulations in a high fidelity environment confirmed the effectiveness of the MPCt and MPCs in correcting terminal understeer behaviour and the importance of constraining

both the state and the input of the system for improved stability. While similar trajectories were followed from both the MPC strategies and a simpler LQR strategy in the case of a U-turn scenario, the MPC strategies achieve this with much lower sideslip angle and yaw rate values. Another point to notice here is that including both the longitudinal slip constraints and the torque constraints in the MPC formulation (something that was implemented in one way or another in both MPC strategies) gives a better knowledge of the system to the controllers and results in more effective control actions. The importance of accounting for the system constraints became crucial in the case of a double-lane change scenario, where the MPCt and MPCs kept the vehicle stable by enforcing the state and input constraints, while the vehicle with the LQR became unstable shortly after the beginning of the manoeuvre. Finally, both scenarios showed that the MPC strategies are real-time implementable even when a generic QP solver is used.

Chapter 6

Nonlinear Constrained Optimal Control Strategy

6.1 Introduction

In this chapter we explore recent developments in the area of fast linear MPC and NMPC and their application on the problem of controlling an EV at the limits of handling using combined longitudinal and lateral dynamics control, as established in chapters 4 and 5. To this end, we employ the general structure of the more promising MPCs strategy from chapter 5 and

1. replace the generic `quadprog` solver from MATLAB with a specialised QP solver as available in FORCES Pro [36] as our preferred linear MPC solver,

2. construct an NMPC strategy that employs the RTI scheme [35],

3. construct an NMPC strategy that employs the Primal-Dual Interior Point (PDIP) method as available in FORCES Pro [36].

All three MPC strategies are based on simplified versions of the same nonlinear optimisation problem: the goal is again to minimise the state and input error from a given reference along the simulation time, subject to the initial condition, the nonlinear system dynamics and the nonlinear state and input constraints. At the same time, by solving the original nonlinear optimisation problem offline we can also obtain the optimal solution and use it as a 'benchmark' against which the three MPC strategies can be compared.

The structure of this chapter is as follows: after detailing the original nonlinear optimization problem to solve and the assumptions used in the construction of the three MPC strategies, we compare the MPC strategies against each other and against the optimal solution in a series of simple step steering case studies. Then, after analysing the relative trade-offs in terms of closed-loop performance and computational cost we validate the most promising solution in CarMaker environment under two limit-handling manoeuvres, similar to the ones used in chapter 5.

6.2 NonLinear Program Problem and MPC Strategies

In this section, we compare three MPC strategies of different levels of complexity in a series of simple step steering case studies designed so that both the advantages and disadvantages of each strategy can be observed. We first obtain the optimal solution of the associated NonLinear Program (NLP) problem for each case and use it as a benchmark to compare the three solutions from two points of view: closed-loop performance and computational complexity. The section is therefore comprised by two parts, the first one presenting the optimal control problem under consideration and how this can be solved offline, and the second one showing how the problem can be simplified and solved online.

6.2.1 NonLinear Program Problem: the Optimal Solution

For the nonlinear continuous-time system with state and input x and u respectively

$$\dot{x} = f_c(x,u), \tag{6.1}$$

the discrete optimal control problem under consideration in this chapter is

$$\min_{x,u} \quad \sum_{k=0}^{N-1} (x_k - r)^T Q_n (x_k - r) + (u_k - l)^T R_n (u_k - l), \tag{6.2a}$$

$$\text{s.t.} \quad x_0 = x_{in}, \tag{6.2b}$$

$$x_{k+1} = f_d(x_k, u_k), \quad k = 0, ..., N-1, \tag{6.2c}$$

$$h(x_k, u_k) \leq 0, \qquad k = 0, ..., N-1. \tag{6.2d}$$

The aim is to minimise the state and input error from a given state reference r and input reference l respectively (6.2a) along the simulation time $T_{sim} = NT_s$, subject to the initial condition (6.2b), the discretised system dynamics (6.2c) and the state and input constraints (6.2d). The resulting NLP problem can then be solved offline using one of the popular optimization methods: we employ the Sequential Quadratic Program (SQP) algorithm with an active set method to solve it, as available in the ACADO Toolkit [60]. In this way, given that the system stabilises to the steady state reference within the chosen simulation time, the optimal solution is obtained which can then be used as the benchmark against which the three online MPC strategies will be compared.

Note in the above equations that we no longer need to include a terminal penalty and that the weighting matrices Q_n and R_n are not found anymore using an exact discretisation of the original continuous time problem (4.7) as was the case in chapter 5, where we were directly comparing the two linear MPC strategies against the LQR from chapter 4. Here

we rather set:

$$Q_n = T_s Q_c, \qquad R_n = T_s R_c,$$

which not only simplifies the calculation but was also found to be a good approximation for the small sampling time of T_s =0.05s used here.

6.2.2 MPC Strategies

For the MPC strategies, the problem to solve is

$$\min_{x,u} \quad \sum_{k=0}^{M-1} (x_k - r)^T Q_n (x_k - r) + (u_k - l)^T R_n (u_k - l), \tag{6.3a}$$

$$\text{s.t.} \quad x_0 = x_{in}, \tag{6.3b}$$

$$x_{k+1} = f(x_k, u_k), \quad k = 0, \ldots, M-1, \tag{6.3c}$$

$$u_k^l \leq x_k \leq u_k^h, \qquad k = 0, \ldots, M-1, \tag{6.3d}$$

$$x_k^l \leq u_k \leq x_k^h, \qquad k = 0, \ldots, M-1, \tag{6.3e}$$

where $M \leq N$ is the prediction horizon and the nonlinear constraints on state and input (6.2d) are replaced by simpler box constraints (6.3d)-(6.3e) for fairness of comparison between the simpler linear MPC strategy and the two NMPC strategies.

Then, the three formulations investigated here are:

- A linear MPC strategy, where the nonlinear system dynamics (6.1) are linearised and discretised with the resulting QP problem solved using the PDIP nethod as available in FORCES Pro [36].
- An NMPC strategy that applies only the first SQP iteration on problem (6.3) according to the RTI scheme [35] as available in the ACADO Toolkit [60].

- An NMPC strategy that applies the PDIP method as available in FORCES Pro [36] to (6.3) until convergence to the optimal solution.

6.2.2.1 Linear MPC

From (6.3) and the short description of the MPC strategies above we can see that the main difference in the problem definition between the linear MPC and the rest of the strategies is how the discrete system dynamics are defined. Similarly to chapter 5, linearising the continuous system dynamics (6.1) about the equilibrium point $(x^{\text{ss}}, u^{\text{ss}})$ gives

$$\dot{x} = A^{\text{ss}}x + B^{\text{ss}}u - (A^{\text{ss}}x^{\text{ss}} + B^{\text{ss}}u^{\text{ss}}),$$

where $(Ax^{\text{ss}} + Bu^{\text{ss}})$ is a constant. Then discretising the above affine system we get

$$x_{k+1} = Ax_k + Bu_k + c,$$

where

$$c = -\int_0^{T_s} e^{A^{\text{ss}}\eta} \mathrm{d}\eta (\mathrm{A}^{\text{ss}}\mathrm{x}^{\text{ss}} + \mathrm{B}^{\text{ss}}\mathrm{u}^{\text{ss}}),$$

like before. The resulting QP can then be solved using the PDIP method as available in FORCES Pro [36].

6.2.2.2 NMPC: RTI scheme and PDIP method

For the two NMPC strategies we use one step of the explicit Runge-Kutta 4th order method to derive the nonlinear discrete dynamics (6.3c) from the continuous dynamics (6.1): the specific method was found to give a good approximation of the continuous dy-

namics for our system at the chosen sampling time of T_s =0.05s. The resulting NMPC can then be solved using the RTI scheme or the PDIP method:

- NMPC-RTI

  In the case of a real-time application like the one considered here, the RTI scheme can be used for fast solutions of problem (6.3): this scheme, in its simplest form, has the benefit of producing fast but suboptimal solutions by precomputing the necessary sensitivities and performing only one SQP iteration [35, 60]. This approach can quickly lead to convergence if the solution does not change much from one time step to the next but can also diverge.

- NMPC-PDIP

  We can also try to solve (6.3) using the PDIP method, as available in the Forces Pro NLP solver [36], until convergence. This approach attempts to solve the NMPC problem in a relatively short time by employing the Broyden-Fletcher-Goldfarb-Shanno (BFGS) algorithm for the computation of the Hessian of the Lagrangian and can give solutions that are very close to the optimal.

6.3 Comparison of the Three MPC Strategies

In this section we compare the linear MPC, NMPC-RTI and NMPC-PDIP strategies as presented in section 6.2.2 against the optimal solution from section 6.2.1 for a range of simple simulation studies. We will neglect the fast wheel speed dynamics (3.2d), so we set for both the simulation model and the internal model for the MPC strategies $x = [V\ \beta\ \dot{\psi}]^T$ and $u = [s_{RLx}\ s_{RRx}]^T$. The input constraints are set similarly to section 5.4.2.1 to

$$|s_{Rjx}| \leq 0.15,$$

while we also set a constraint on the product of the vehicle's yaw rate and velocity based on the lateral acceleration limit

$$-\mu_{max} g \leq \dot{\psi} V \leq \mu_{max} g, \tag{6.4}$$

which for the MPC strategies is simplified to a constraint on the yaw rate only as a function of the velocity at the beginning of the prediction horizon as in (5.7):

$$|\dot{\psi}| \leq \mu_{max} g / V_{in}.$$

In the test scenarios considered here, the vehicle is initially moving on a straight line and at time $t = 0$s we apply a step steering input for the duration of $T = 10$s [1], with the initial speed chosen so that it is greater than the corresponding V_{max} for that steering input. Each controller will then aim to stabilise the vehicle to the steady-state reference $x_{ref} = [V^{ss} \ \beta^{ss} \ \dot{\psi}^{ss}]^T$, $u_{ref} = [s^{ss}_{RLx} \ s^{ss}_{RRx}]^T$ by minimising (6.3a) subject to (6.3b)-(6.3e). Following the analysis for the MPCs strategy in section 5.5, the sampling time and the horizon for the MPC strategies to T_s =0.05s and M =20steps respectively, while for the evaluation of the performance of the MPC strategies we use again the closed-loop cost (5.18).

Table 6.1 shows the average and maximum computational times along with the minimum and maximum closed-loop costs (expressed as percentage difference from the optimal) for the three MPC strategies for a range of step steering inputs from 2 to 10deg and different initial velocities, ranging from 1m/s to 4m/s above the V_{max} for that steering input[2]. Looking at the computational times in Table 6.1, we can see that they scale accord-

[1] the simulation time chosen long enough so that the states always converge to the steady-state reference before the end of each test.

[2] the range of initial velocities chosen so that the original NLP problem (6.2) is always feasible for the given drivetrain topology and actuator limits

	Avg comp. time (ms)	Max comp. time (ms)	Min per. penalty (%)	Max per. penalty (%)
Linear MPC	1.1	5.3	28.08	109.85
NMPC-RTI	3.0	14.9	2.01	$5.91 \cdot 10^5$
NMPC-PDIP	3.6	29.5	0.79	28.23

Table 6.1: Comp. times and performance results from the three MPC strategies

ing to the problem complexity, with the linear MPC being the fastest and the NMPC-PDIP the slowest across all results. Another interesting point is the maximum observed time for the NMPC-PDIP which is much higher than the two other strategies: this happens when the NMPC-PDIP reaches the maximum number of iterations allowed (which in our tests is set to 200 iterations) without fully converging, at which point it gives the last computed sub-optimal solution. Looking at the performance penalty for the three strategies on the last two columns of Table 6.1, we observe that the linear MPC is consistently above 28.08% difference from the optimal, but does not go above 110%, while the NMPC-PDIP only reaches a maximum of 28.23%. The NMPC-RTI strategy on the other hand reaches high maximum closed-loop cost values due to infeasibility problems, a result that shows the main disadvantage of performing only one SQP iteration at each time step.

Fig. 6.1 shows the computational time versus performance penalty plots for the set of simulation tests from Table 6.1. It can be confirmed that the linear MPC strategy (in red, with the red circle showing the average for each test) performs almost the same across all the tests and, apart from only a few occasions when more iterations of the PDIP method are used to find a solution, it returns a solution in less than 5ms. On the other hand, the NMPC-PDIP strategy (in blue, with the blue asterisk showing the average for each test) performs closer to the optimal across all tests and mostly drops in performance when the initial velocity is further away from the reference velocity V_{max}. However this is done at the expense of longer computational times since in quite a few tests the maximum number

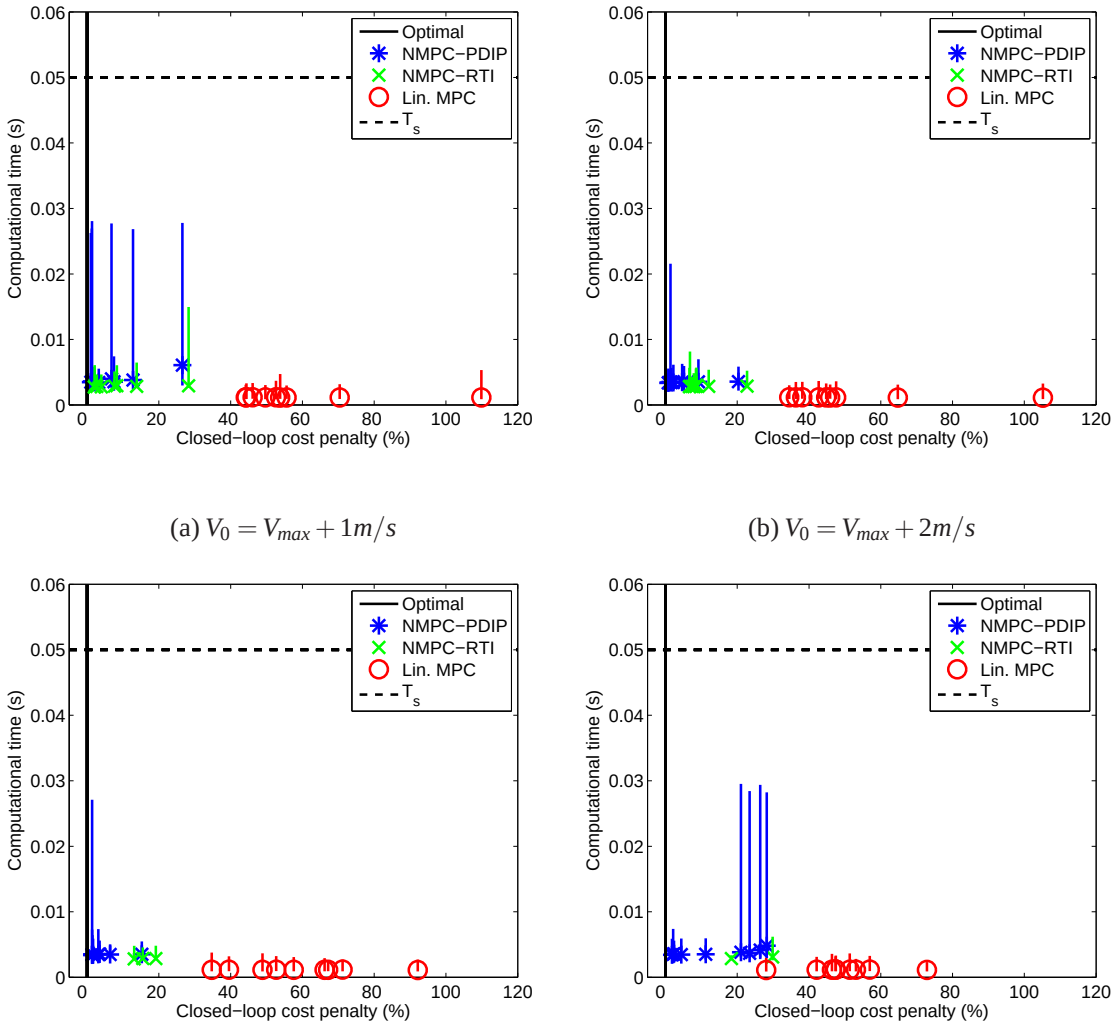

(a) $V_0 = V_{max} + 1m/s$

(b) $V_0 = V_{max} + 2m/s$

(c) $V_0 = V_{max} + 3m/s$

(d) $V_0 = V_{max} + 4m/s$

Figure 6.1: Computational times versus performance penalty from the optimal solution for a range of step steering inputs from 2 to 10deg and different initial velocities.

of iterations is reached at least once, hence the much larger maximum times observed in some of the results. Finally, the NMPC-RTI strategy (in green, with the green x showing the average for each test), shows excellent performance with low computational times when the initial state is close to the target, but quickly drifts to higher closed-loop penalty values for higher initial state errors, showing the main disadvantage of using this strategy

as already observed in the analysis of Table 6.1 above.

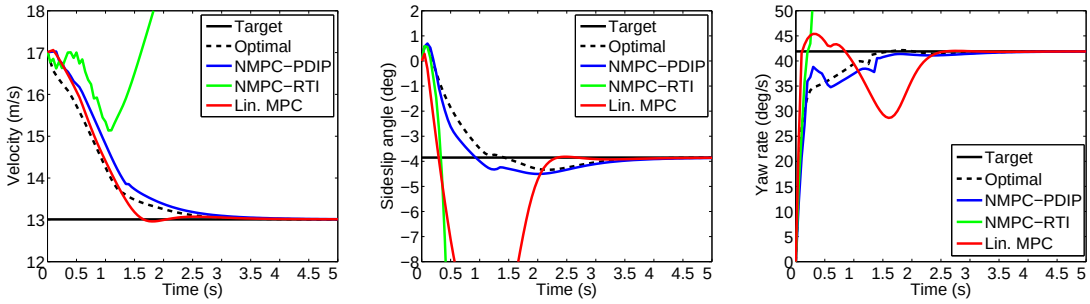

(a) Velocity

(b) Sideslip angle

(c) Yaw rate

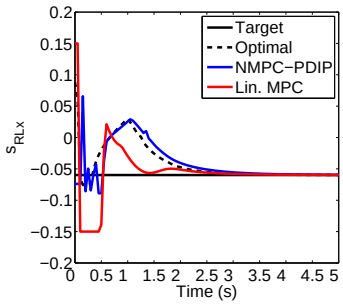

(d) Rear-left long. slip

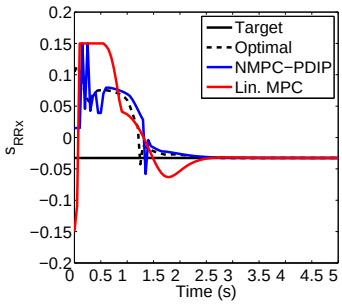

(e) Rear-right long. slip

Figure 6.2: Velocity, sideslip angle, yaw rate and longitudinal slip histories for a step steering input of 8deg and an initial velocity difference from V_{max} of 4m/s for the three MPC strategies (note that for clarity reasons, the highly oscillatory longitudinal slip results for the NMPC-RTI have been omitted).

An example of the difference in state regulation from the optimal for the three MPC strategies in one of the test scenarios presented in Fig. 6.1 above can be seen in Fig. 6.2 where we find the velocity, sideslip angle, yaw rate and longitudinal slip time histories for a step steering input of 8deg and an initial velocity which is 4m/s higher than V_{max} for this steering input. While the velocity time histories for the linear MPC and the NMPC-PDIP strategies are similar and both close to the optimal trajectory (Fig. 6.2a), the yaw rate and especially the sideslip angle time histories are quite different. While the linear MPC strategy exhibits large oscillations in both the sideslip angle and yaw rate, the NMPC-PDIP strategy remains close to the optimal solution (Figs. 6.2b-6.2c), with only a small overshot at the yaw rate, which is directly connected to the oscillations observed from

the NMPC-PDIP strategy in the longitudinal slip time histories (Figs. 6.2d-6.2e) and is the result of the NMPC-PDIP strategy finding it difficult to cope with the hard yaw rate constraint. Despite this, the NMPC-PDIP strategy shows excellent response with results very close to the optimal solution and demonstrates the importance of accounting for the nonlinear system dynamics in the form of the equality constraint (6.3c) rather than linearising the system dynamics as is the case with the linear MPC strategy. Finally, for this test scenario the vehicle with the NMPC-RTI strategy quickly becomes unstable due to the high initial state error from the reference.

While the NMPC-RTI convergence problems with higher initial state errors, as explained above, could be possibly addressed using a shorter sampling time and/or more SQP iterations, the fact remains that the NMPC-PDIP strategy shows more promising results, the main problem been the longer computational times. One way to help the PDIP solver achieve convergence faster while avoiding infeasibility problems is by soft constraining the state, which can be done by introducing slack variables into the cost function (6.3a) and relaxing the state constraints (6.3e):

$$\min_{x,u} \quad \sum_{k=0}^{M-1} (x_k - r)^T Q_n (x_k - r) + (u_k - l)^T R_n (u_k - l) + \rho_\varepsilon \varepsilon_k, \tag{6.5a}$$

$$\text{s.t.} \quad x_0 = x_{in}, \tag{6.5b}$$

$$x_{k+1} = f(x_k, u_k), \qquad k = 0, \ldots, M-1, \tag{6.5c}$$

$$u_k^l \leq u_k \leq u_k^h, \qquad k = 0, \ldots, M-1, \tag{6.5d}$$

$$x_k^l - \varepsilon_k \leq x_k \leq x_k^h + \varepsilon_k, \quad k = 0, \ldots, M-1, \tag{6.5e}$$

$$\varepsilon_k \geq 0, \qquad k = 0, \ldots, M-1, \tag{6.5f}$$

where $\varepsilon_k \in \mathbb{R}^+$ $(k = 0, \ldots, M-1)$ and ρ_ε are the slack variables and their weight respectively.

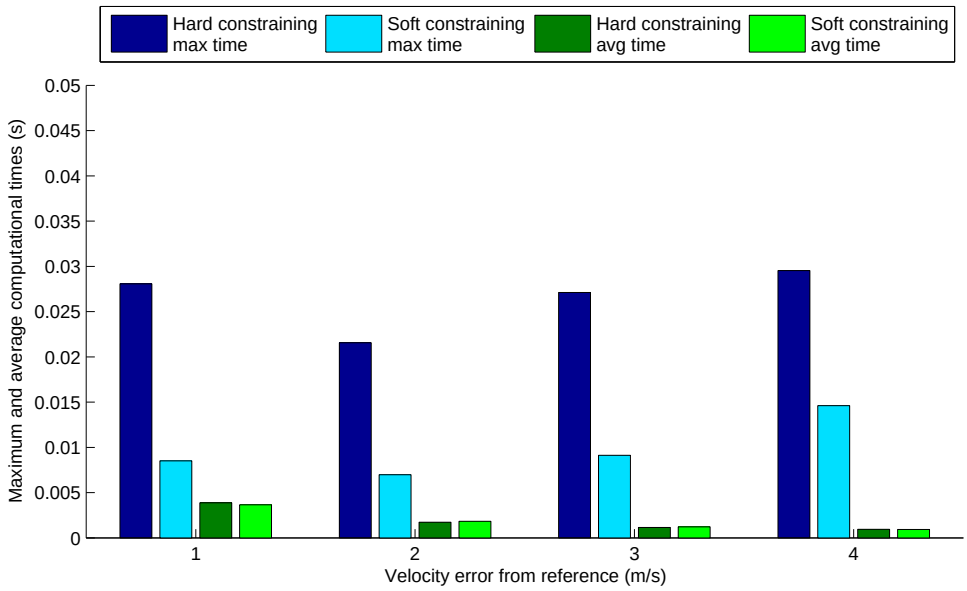

Figure 6.3: Comparison of maximum (blue bars) and average (green bars) computational times for the NMPC-PDIP (in dark blue and green) and the NMPC-PDIP with soft constraints (in light blue and green) for the range of test scenarios considered in this section, starting from different initial velocities.

Fig. 6.3 shows the change in average and maximum computational times for the NMPC-PDIP strategy after softening the yaw rate constraint (5.7). The maximum time has decreased to less than half in all cases, while the average times show no major differences from the hard constrained NMPC-PDIP strategy despite the fact that the inclusion of the slack variables has increased the number of optimisation variables. It is worth noting here also that no infeasibility problems have been observed after softening the yaw rate constraint and that the maximum number of 200 iterations was never reached across all cases. These results confirm that soft constraining not only removes infeasibility problems in the solution of the optimisation problem at hand but also helps in reaching a solution faster.

Returning to the example scenario examined in Fig. 6.2, in Fig. 6.4 we see the differ-

ence in response from the vehicle with the NMPC-PDIP strategy after softening the yaw rate constraint. While the velocity time histories are similar (Fig. 6.4a), the sideslip angle for the soft constrained NMPC-PDIP is much closer to the optimal solution (Fig. 6.4b). The main difference is however found in the yaw rate time histories (Fig. 6.4c) where we can see that the yaw rate overshot has disappeared in the soft constrained NMPC-PDIP case, a result also linked to the smoother longitudinal slip inputs from this strategy, as evidenced in Figs. 6.4d-6.4e.

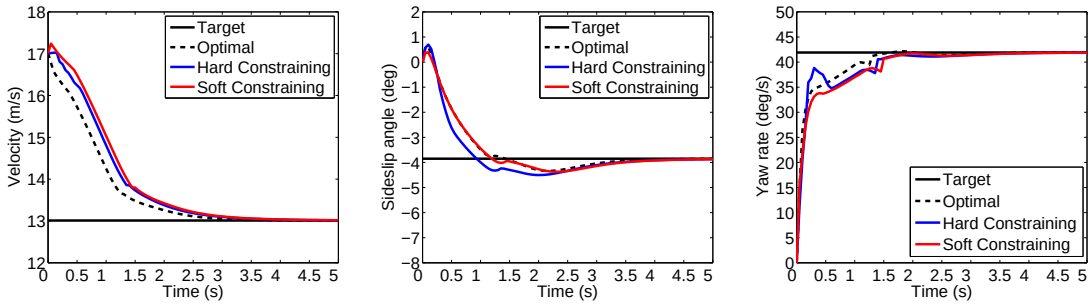

(a) Velocity

(b) Sideslip angle

(c) Yaw rate

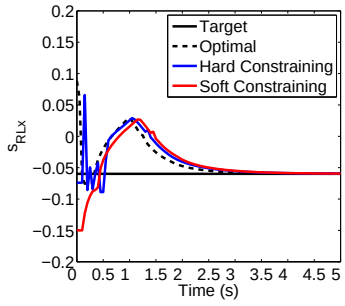

(d) Rear-left long. slip

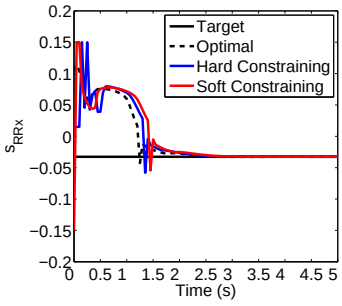

(e) Rear-right long. slip

Figure 6.4: Velocity, sideslip angle, yaw rate and longitudinal slip histories for a step steering input of 8deg and an initial velocity error of 4m/s for the hard constrained and the soft constrained NMPC-PDIP strategy.

6.4 dSPACE Deployment

The soft constrained NMPC-PDIP strategy as presented above was then deployed on a dSPACE DS1005 board (PowerPC 750GX at 1.00GHz with 128MB global main memory). The limited processing power of such platform means that it was necessary to limit the maximum number of iterations that the solver can perform before returning a (sub-)optimal solution to 25. However, since each iteration takes a fixed time to run, this also means that we can guarantee that the solver will always return a solution within the given sampling time.

In order to test the soft-constrained NMPC-PDIP strategy in real-time, we connected it as in the previous section 6.3 with a simulation model that neglects the fast wheel speed dynamics (3.2d) and deployed the complete closed-loop control system on the dSPACE DS1005 board. This involved deploying the source code for the soft constrained NMPC-PDIP solver and the simulation model as one closed-loop model, along with linking any additional files needed by the solver. Then, to record the computational times for the solver the dSPACE Profiler was used: this application runs on the host machine and, by receiving time-stamped events, can provide information on the timing of a defined task (such as the time to run the solver per call).

Fig. 6.5 shows the average and maximum computational times when the same series of case studies as before is performed on the DS1005. We notice that the maximum computational time across all case studies is around 43ms which corresponds to the set maximum number of 25 iterations per call of the solver, while the relative increase in computational effort can also be seen in the average times. However, the loss in performance due to the cap in the maximum number of iterations is less than someone would expect: as we can see from Fig. 6.6 for a characteristic example of a scenario where the maximum number of iterations is reached multiple times, the velocity, yaw rate and longitudinal slip

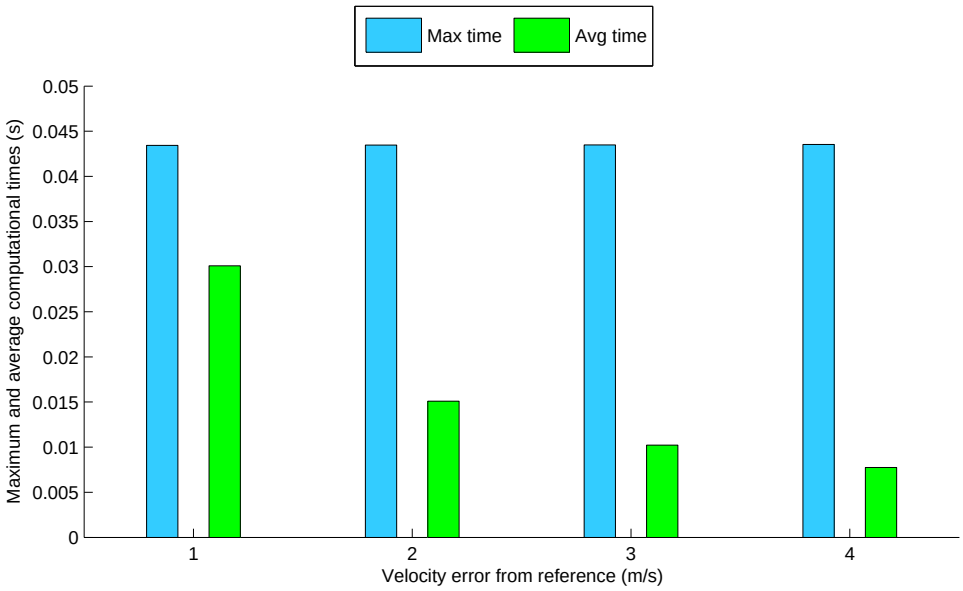

Figure 6.5: Maximum (blue bars) and average (green bars) computational times for the soft constrained NMPC-PDIP after deployment on the DS1005.

trajectories for the deployed controller remain close to the trajectories obtained from the desktop machine (where the maximum number of iterations is never reached).

From the above analysis it is obvious that NMPC solutions are in general very demanding in terms of required computational power. However, after careful consideration of the required steps to obtain real-time feasibility like setting a limit on the maximum number of iterations, it is possible to deploy such solutions on real-time hardware: as we have seen here, the proposed soft constrained NMPC-PDIP strategy can be successfully deployed on a rapid prototyping platform with minimal performance loss, even for the extreme step steering input cases considered so far.

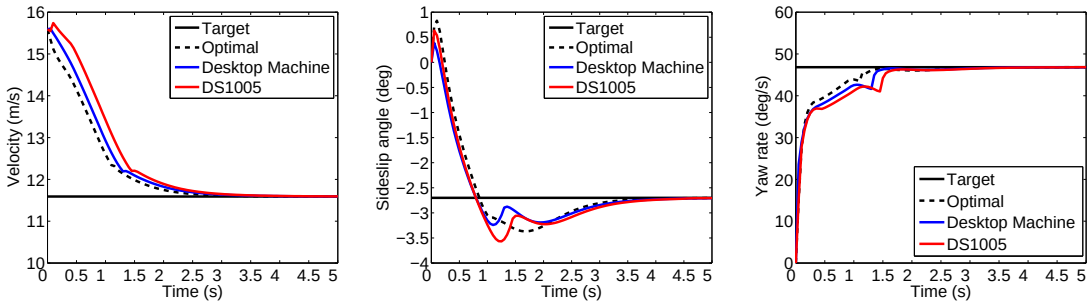

(a) Velocity (b) Sideslip angle (c) Yaw rate

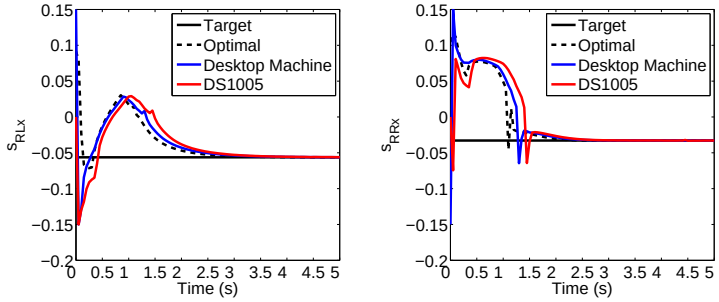

(d) Rear-left long. slip (e) Rear-right long. slip

Figure 6.6: Velocity, sideslip angle, yaw rate and longitudinal slip histories for a step steering input of 10deg and an initial velocity error of 4m/s for the soft constrained NMPC-PDIP strategy on the desktop machine and the DS1005.

6.5 Evaluation of the NMPC-PDIP strategy

In order to test the soft constrained NMPC-PDIP strategy (6.5) in CarMaker environment, we first cascade it with a Sliding Mode Slip Controller in a way similar to the MPCs control structure from section 5.4.2, with the complete control structure seen in Fig. 6.7. We also reinstate the two extra inequality constraints (5.8) and (5.16) due to implementation reasons, the first one restricting the sideslip angle of the vehicle for subjective feel and the second one considering the electric motor limits in the form of its static torque map.

We can then compare the complete solution in CarMaker environment against a baseline vehicle with no active control and one that applies a linear MPC controller instead on problem (6.5) with the same input and state constraints in two limit-handling scenarios: (i) the U-turn manoeuvre from sections 4.4 and 5.6.1, but this time setting a higher initial

speed and (ii) an obstacle avoidance manoeuvre according to ISO 3888-2:2011 [23]. The purpose of the two tests is to show how the velocity regulation combined with the lateral dynamics control – while respecting the system constraints – from the two MPC strategies manage to keep the vehicle stable and what are the advantages of using an NMPC strategy against the faster but sub-optimal linear MPC strategy in real world critical situations.

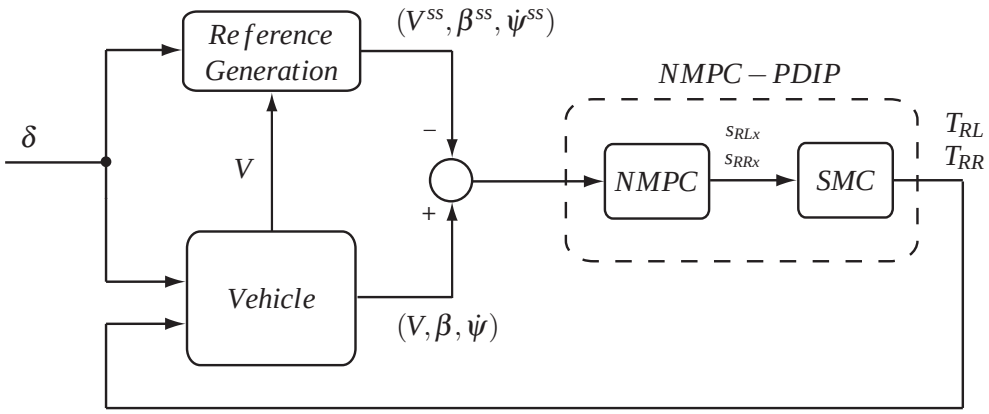

Figure 6.7: NMPC-PDIP control structure.

6.5.1 U-turn Scenario

For the U-turn scenario, we use the driver model in CarMaker to steer the vehicle through a turn of 40m radius like before in sections 4.4 and 5.6.1. The road is assumed dry (μ_{max} =1) the entry speed is set at the higher velocity of 85km/h in order to better emphasise the difference in response from the three vehicles, while we assume again that no acceleration or braking commands come from the driver. Note that this time the velocity error penalty is set higher to q_V =500.

As we can see from Fig. 6.8a, this time the uncontrolled vehicle loses control due to high entry speed and eventually leaves the road. The two MPC strategies on the other hand keep the vehicle on the road, but with a small difference: looking more closely especially to the first half of the turn, we can see that the NMPC-PDIP manages a much

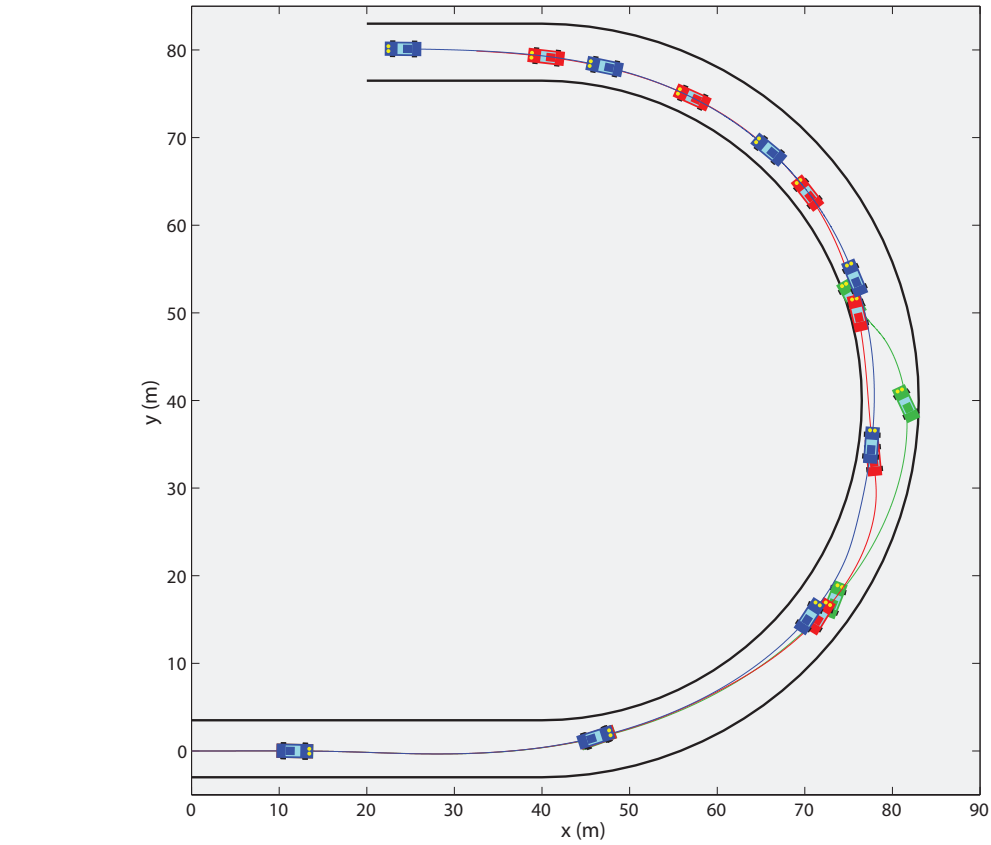

(a) Trajectory

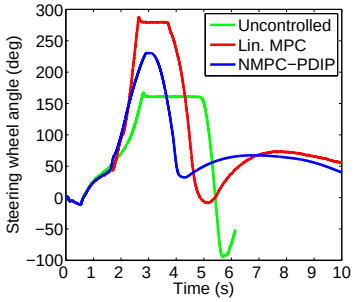

(b) Steering wheel angle

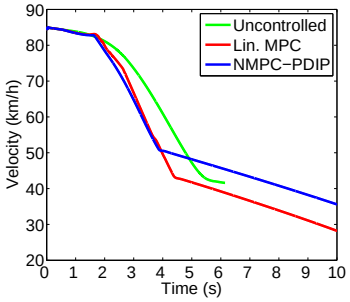

(c) Velocity

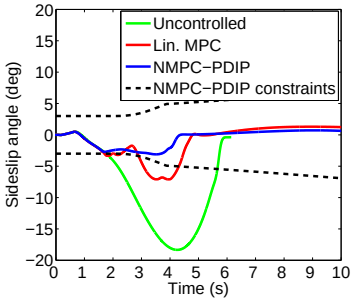

(d) Sideslip angle

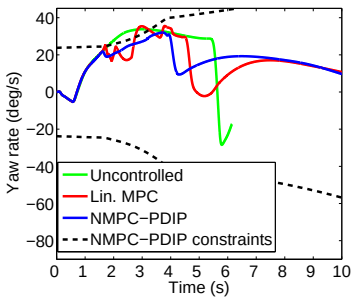

(e) Yaw rate

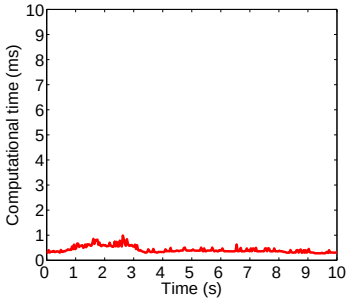

(f) Lin. MPC comp. time

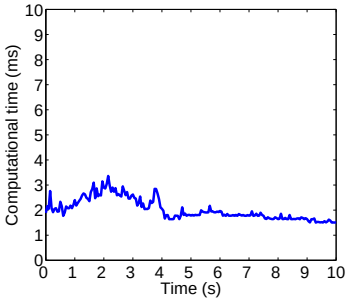

(g) NMPC-PDIP comp. time

Figure 6.8: Comparison of the uncontrolled vehicle (in green), the vehicle with the linear MPC (in red) and the vehicle with the NMPC-PDIP (in blue) in the U-turn scenario.

smoother trajectory compared to the linear MPC.

The above observation on the difference between the trajectories of the vehicle with the NMPC-PDIP strategy against the one with the linear MPC is directly connected to how the two strategies regulate the state as seen in Fig. 6.8. While the velocity regulation from the two strategies is, apart from the exit speed, mostly the same (Fig. 6.8c), the sideslip angle and yaw rate time histories (Figs. 6.8d-6.8e) show oscillations for the linear MPC strategy due to the simpler linear internal model used in this case which can not predict as effectively the state violations.

The difference in response between the two strategies is also apparent in the longitudinal slip and torque time histories as found in Fig. 6.9, where we observe excessive oscillations in the longitudinal slip demands from the linear MPC (Figs. 6.9a-6.9b), es-

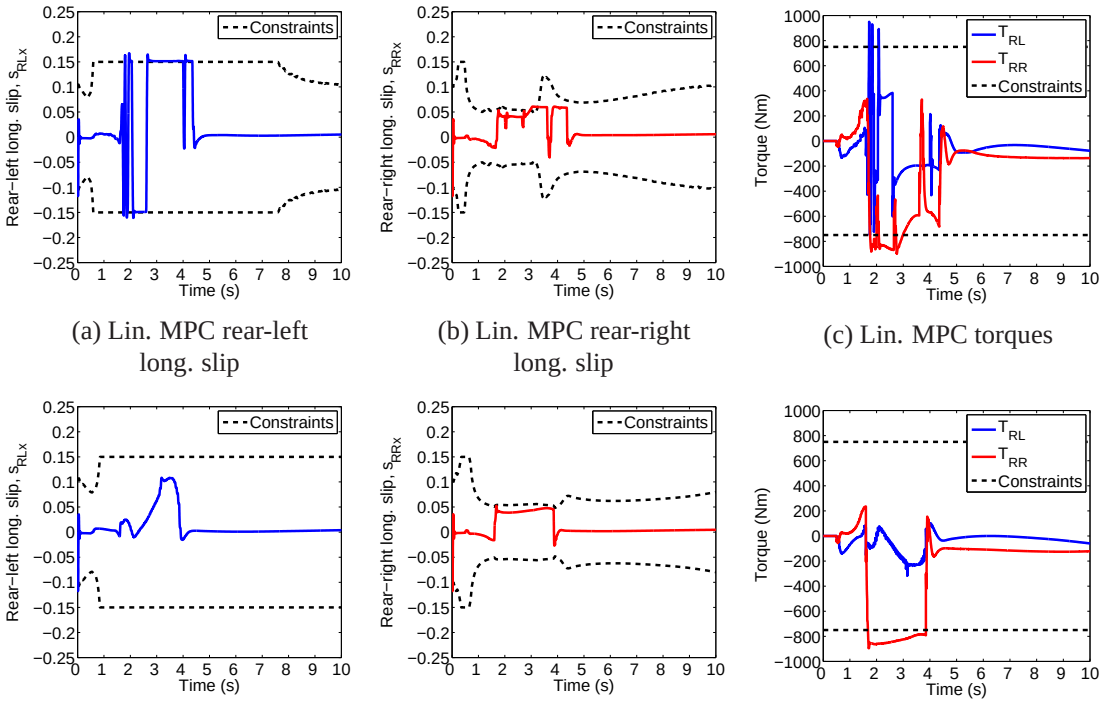

(a) Lin. MPC rear-left long. slip

(b) Lin. MPC rear-right long. slip

(c) Lin. MPC torques

(d) NMPC-PDIP rear-left long. slip

(e) NMPC-PDIP rear-right long. slip

(f) NMPC-PDIP torques

Figure 6.9: Longitudinal slip (actual) and torque (requested) time histories for the linear MPC and the NMPC-PDIP strategies in the U-turn scenario.

pecially in the case of the less loaded rear left wheel, which also translate into violent torque commands (Fig. 6.9c). The NMPC-PDIP strategy on the other hand shows much smoother torque commands and a more efficient longitudinal slip regulation. Note that the torque limit violations as seen in Figs. 6.9c-6.9f occur due to the fact that the two MPC strategies are constructed in a way similar to the MPCs strategy from chapter 5, thus do not directly control the torque on the wheels. However, as already analysed in section 5.6.1 for the MPCs stategy, removing them would result in much higher demanded torques.

Finally, looking at the computational times for the two strategies, the linear MPC returned an average and a maximum time of 0.42ms and 0.98ms respectively, while for the NMPC-PDIP the corresponding times were 1.9ms and 3.4ms, which are much lower than the sampling time of 50ms for the two strategies.

6.5.2 Obstacle Avoidance Scenario

For the obstacle avoidance scenario we use again the driver model available in CarMaker, but this time to navigate through a double-lane change, as defined by three valleys of cones according to the specifications of ISO 3888-2:2011 [23] and the given vehicle parameters (more details on the test specifications can be found in Appendix F). The road is assumed again dry ($\mu_{max} = 1$), the entry speed is set to 75km/h, while no acceleration or braking commands come from the driver. Note that the velocity error penalty is again set to q_V =500 as in the U-turn scenario of the previous section.

Fig. 6.10a shows the trajectories for the three vehicles. We can see that the uncontrolled vehicle spins out of control towards the end of the manoeuvre, while the two MPC strategies manage to keep the vehicle stable. However, only the vehicle with the NMPC-PDIP strategy manages to successfully complete the test since the linear MPC fails to pass

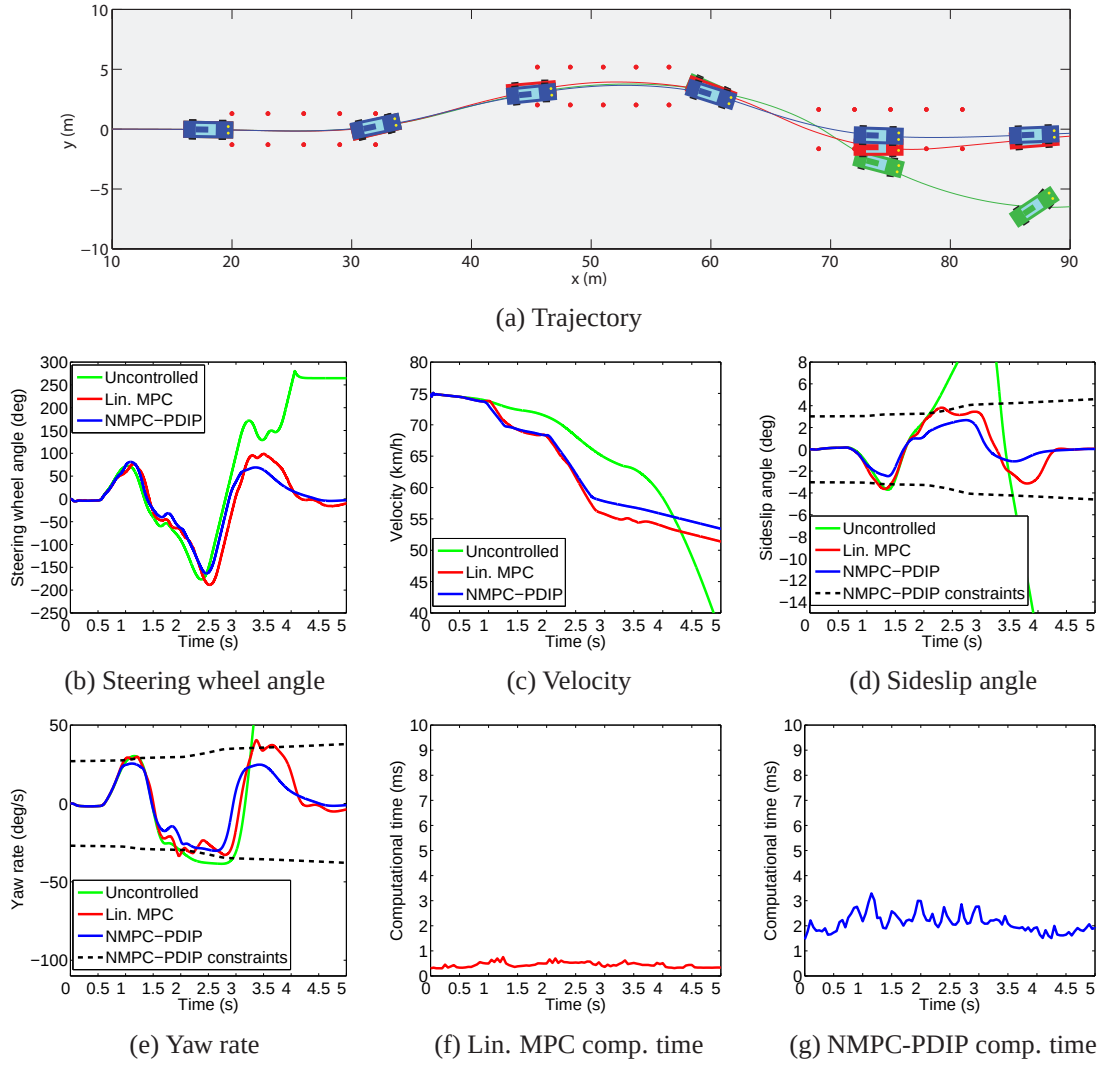

(a) Trajectory

(b) Steering wheel angle

(c) Velocity

(d) Sideslip angle

(e) Yaw rate

(f) Lin. MPC comp. time

(g) NMPC-PDIP comp. time

Figure 6.10: Comparison of the uncontrolled vehicle (in green), the vehicle with the linear MPC (in red) and the vehicle with the NMPC-PDIP (in blue) in the obstacle avoidance scenario.

through the last valley of cones without hitting them (Fig. 6.10a).

This slight difference between the trajectories of the two MPC strategies is again related, as in the U-turn scenario above, to the way they handle the system constraints. As observed in Fig. 6.10, while the velocity time histories are almost identical between the linear MPC and the NMPC-PDIP (Fig. 6.10c), the sideslip angle and yaw rate histories are quite different, with the linear MPC showing higher values and more oscillations in Figs. 6.10d-6.10e caused again by the simpler linear internal model used in this case.

Looking at Fig. 6.11, excessive oscillations are again observed in the longitudinal slip time histories from the linear MPC (Figs. 6.11a-6.11b) and violent torque commands (Fig. 6.11c) which are in strong contrast to the subtle regulation from the NMPC-PDIP (Figs. 6.11d-6.11d). Note that the torque limit violations (Figs.6.11c and 6.11f) occur

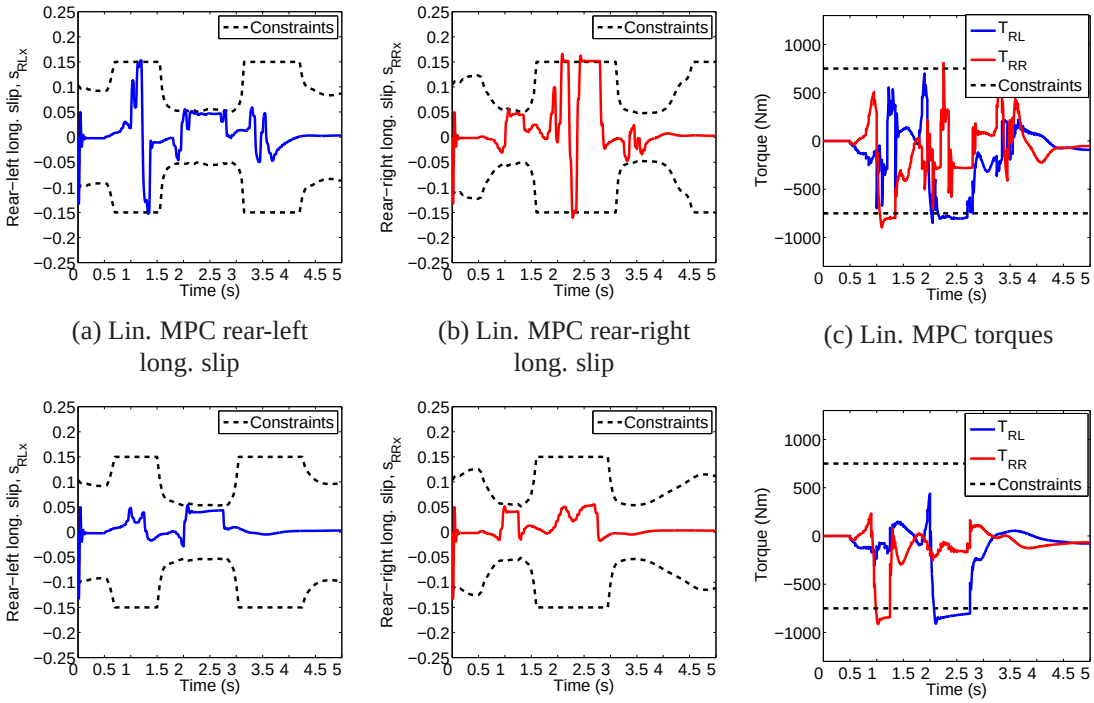

(a) Lin. MPC rear-left long. slip

(b) Lin. MPC rear-right long. slip

(c) Lin. MPC torques

(d) NMPC-PDIP rear-left long. slip

(e) NMPC-PDIP rear-right long. slip

(f) NMPC-PDIP torques

Figure 6.11: Longitudinal slip (actual) and torque (requested) time histories for the linear MPC and the NMPC-PDIP strategies in the obstacle avoidance scenario.

again due to the fact that the two MPC strategies do not directly control the torque on the wheels.

Finally, for the double-lane change scenario the average and maximum computational times for the linear MPC were 0.44ms and 0.75ms respectively, while for the NMPC-PDIP the corresponding times were 2.1ms and 3.3ms, times similar to the ones found for the U-turn scenario.

6.6 Conclusions

In this chapter we have presented three fast MPC strategies for stabilisation of the vehicle at the limits of handling. The first strategy (simply called 'linear MPC') is using a linear MPC formulation and employs the PDIP method [36] to solve the subsequent QP problem, the second strategy (called 'NMPC-RTI') is using a NMPC formulation and employs the RTI scheme [35], while the third strategy (called 'NMPC-PDIP') is using again an NMPC formulation but employs the PDIP method instead [36] to solve the resulting NLP problem.

After comparing the three strategies against each other and against the optimal solution in terms of closed-loop performance and computational cost using hard state and input constraints in a series of case studies it was shown that while a linear MPC remains the fastest strategy, it also returns suboptimal solutions that can greatly deviate from the optimal solution. The NMPC-RTI strategy on the other hand returned excellent performance and low computational times for small initial state errors, but quickly encountered infeasibility issues for larger initial state errors due to the intrinsic methodology of the RTI scheme, which applies only the first SQP iteration on the NLP problem. The best method was found to be the NMPC-PDIP which remained consistently close to the optimal solution across the range of the case studies and, after softening the state constraint,

also showed a substantial decrease in the computational cost.

The importance of using a nonlinear system dynamics representation in the MPC formulation was also confirmed in two limit-handling manoeuvres: a U-turn scenario with excessive entry speed and a double-lane change in accordance to ISO 3888-2:2011 [23]. While both the NMPC-PDIP and the linear MPC kept the vehicle stable contrary to the uncontrolled vehicle which became unstable in both test scenarios, the NMPC-PDIP strategy exhibited a better state regulation and much smoother torque commands which resulted in being the only strategy to successfully complete the ISO 3888-2:2011 test.

Chapter 7

NMPC with State Estimation for Output Feedback

7.1 Introduction

Up to this point it was assumed that exact measurements of the vehicle state were available for control. In this chapter we investigate the use of an optimal estimation strategy to provide the variables of interest. In order to keep the implementation complexity to a minimum, for the estimation we focus only on the higher vehicle dynamics level, namely the velocity, sideslip angle and yaw rate of the vehicle, while we also assume that the only measurements available come from inexpensive sensors usually fitted on a standard vehicle, namely an Inertial Measurement Unit (IMU), the steering wheel angle sensor and the four wheel speed sensors.

The structure of this chapter is as follows: after reviewing some of the most interesting

solutions on the subject of vehicle dynamics estimation in the literature and analysing the relative advantages (and disadvantages) of the different methods proposed so far, we introduce the nonlinear optimal estimator used in this work and check its performance under two simulation scenarios:

- The first test validates the derived estimator on a race circuit, whereas the driver model in CarMaker is used to drive the vehicle around a track. No active control is assumed to be in place for this test.

- The second test couples the derived estimator with the NMPC-PDIP strategy from chapter 6 and evaluates the complete solution in the obstacle avoidance scenario of section 6.5.2 in accordance to ISO 3888-2:2011 [23]. It therefore checks how the controller performance changes in the presence of uncertainties and noise in the provided state information.

7.2 Review of KF Strategies for Vehicle Dynamics Estimation

The reason for estimating arises from the fact that typically in a real system not all variables of interest are easily obtainable: in a vehicle dynamics context for example, while sensors to directly measure the sideslip angle of the vehicle do exist these are typically expensive. For this reason, a number of optimal estimation strategies can be found in the literature ranging from simple Kalman Filters (KF) to Receding Horizon Estimation (RHE) strategies, with most of them based on the assumption that the only available measurements come from an IMU and/or a Global Positioning System (GPS), each of the systems with its distinct advantages and disadvantages:

- The GPS can be used to directly measure variables of interest like the vehicles vector velocity, but it is usually slow with frequencies ranging from 1 to 10Hz and is sensitive to surroundings blocking the GPS antenna signal.

- The IMU is usually faster with a frequency of around 100 to 1000Hz and can be used to indirectly find the variables of interest from the accelerometers measurements, but these are contaminated with noise and bias.

For these reasons, despite the fact that the GPS and IMU measurements could be potentially used directly, a large part of the literature is dedicated into using the GPS and/or IMU measurements in an estimation strategy in either a kinematic or a model-based form, the term kinematic coming from the fact that in this type of estimation the model used is based solely on the kinematic relationships between the sensors.

A kinematic Extended KF (EKF) to estimate the vehicles sideslip angle is presented in [17]. Here the vehicle heading along with the yaw rate gyroscope which is modelled as a random walk are first found, with the yaw rate as measured from the gyroscope set as the input of the system. Then, during straight line driving the observation matrix is set to $[1\ 0]$ so that the yaw rate gyroscope bias can be found from the GPS course measurement, while during turning the observation matrix is set to $[0\ 0]$ in order to estimate the vehicle heading through integration of the yaw rate gyroscope. Then the sideslip angle can be found as the difference between the GPS course angle and the estimated vehicle heading. The proposed solution gives a good match against experimental data but has drawbacks: apart from the sensor drift and scale factors problems which are inherent to kinematic methods, the slow GPS and the faster IMU signals need to be also correctly aligned. For these reasons the authors in [17] also propose a second formulation, which uses a dual GPS antenna arrangement to completely eliminate heading and synchronization errors by measuring the vehicle heading from the two GPS antennas and from this directly estimate the sideslip angle.

In [19] we find another kinematic EKF strategy to estimate the vehicles sideslip angle, this time using a kinematic model based on the lateral velocity along with the lateral accelerometer bias as states, the accelerometers as input and the GPS velocity as measurement. Then, in a similar fashion to [17], between GPS measurements the EKF simply integrates the accelerometer measurements to find the lateral vehicle velocity and when the GPS signal becomes available again the velocity measurements are used to estimate the accelerometer bias. The vehicles sideslip angle can then be found as the inverse tangent of the lateral to longitudinal velocity fraction. Another interesting point in [19] is the short study on the GPS latency due to the low sampling time and the extra time needed to process and transmit the receiver data, and how this needs to be accounted for in the estimator. Experimental results show that indeed the integration of GPS with IMU measurements gives a better estimation of the sideslip angle, with less noise and no drifting.

The importance of pitch and roll compensation in the estimation of the vehicle dynamics is investigated in [64], where the work presented in [17, 19] is extended by including the estimation of the longitudinal velocity of the vehicle along with extra terms for the effect of pitch and roll in the kinematic EKF formulation from [19]. A separate estimation strategy is then used to find the roll of the vehicle using a kinematic EKF which is similarly structured to the yaw angle EKF from [17]. Experimental results on a graded road show that accounting for the road grade and the vehicle roll has a positive impact in both the longitudinal velocity and sideslip angle estimation under such conditions. The effect of the total roll angle (suspension movement plus road bank angle) on the vehicle is further examined in [18]. Here a kinematic EKF is constructed to estimate the lateral and roll dynamics of the vehicle using a dual-antenna GPS configuration mounted laterally, along with IMU measurements like before. Experimental results against a kinematic EKF using a single GPS antenna to estimate the lateral vehicle dynamics only show that, while the effects of the roll of the vehicle are somewhat taken into account in the lateral

accelerometer bias in the single GPS antenna case, the advantages of using the two GPS antennas configuration to estimate the vehicle roll are apparent with better sideslip angle and tyre slip angles estimation.

One of the earliest examples of a model-based estimator can be found in the two papers from Ray [116, 117], which present an Extended Kalman-Bucy Filter (EKBF) to estimate the tyre forces use a single and a two track vehicle model. In order to avoid reliance on knowledge of the tyre/road road coefficient, the vehicle model is augmented by the tyre forces in the state vector modelled as random walks. Then an EKBF is constructed to estimate the tyre forces using the wheel steering angle and the brake torques as inputs and the IMU measurements as output. A tyre/road friction coefficient estimation strategy is also presented in [117]: after constructing a nominal tyre model from estimated vehicle state data, μ_{max} is found recursively by statistically comparing the forces estimated by the EKBF to those that result from the tyre force model for a particular μ_{max}. Experimental results using field test data and a sampling time of 10 to 30ms for the EKBF show good tyre forces estimation and that the effectiveness of tyre/road friction coefficient estimation depends on the magnitude of the estimated tyre forces since small tyre forces are nearly independent of μ_{max}.

A range of model-based KFs for estimation of the vehicle dynamics is proposed in [92]. Here a KF, an EKF and an adaptive EKF are presented, all based on a modified bicycle model that includes roll dynamics and has the wheel steering angle and the wheel speeds as inputs, with the adaptive EKF also including the tyre stiffness in the state vector. The authors also assume that the measurement and process noises affect each other by setting the cross-correlation matrix to non-zero. High fidelity simulation results with no longitudinal acceleration show that inclusion of the cross-correlation matrix improves slightly the estimation in the higher frequencies and that the adaptive EKF strategy is the most promising. However, as the authors themselves mention, the greater source of

discrepancy is the oversimplification of the tyre behaviour in the estimator model.

A closer study on the choice of the tyre model in the performance of a model-based estimator can be found in [9]. Here an EKF is constructed using a single track vehicle model which ignores the longitudinal vehicle (and tyre) dynamics combined with either a linear tyre model, the Burckhardt model, the MF or a linear adaptive tyre model that employs a local linearisation of the tyre curve on each time step. From the high fidelity simulation results we can see that the solution that employs the linear tyre model fails to track both the sideslip angle and the lateral tyre forces for higher speeds on a slippery road and that the best overall results are achieved when the adaptive tyre model is used. However, all proposed solutions fail when the vehicle brakes are applied: this is expected since the zero longitudinal dynamics assumption is not valid anymore. Experimental results on the other hand are similar for all tyre models used, with only the solution that employs the linear tyre model showing big deviations from the true sideslip angle value.

A comparison of a model-based EKF and a model-based UKF for vehicle dynamics estimation can be found in [38]. Both strategies use a four-wheel vehicle model combined with a Dugoff tyre model to estimate the lateral tyre forces and the sideslip angle of the vehicle. An interesting point in the vehicle model formulation is the use of the vertical forces of the tyres as inputs: these are estimated separately by an EKF employing suspension sensors that measure the distance between the individual wheels and the car body [37]. A comparison of the two estimation strategies on an experimental vehicle equipped with suspension sensors and wheel transducers to measure tyre forces and wheel torques shows that the UKF shows superior performance when the vehicle is operating close to the limits of handling which, according to the authors, is due to the large linearisation errors in the EKF under such conditions.

Another example from the literature that examines the difference between a model-based EKF and a model-based UKF is presented in [5]. In contrast to [38], the necessary

vertical tyre forces are not assumed known and a quasi-static model is used instead to calculate them as functions of the vehicle states and the wheel steering angle input. Then the two optimal estimation strategies are constructed using a two-track vehicle model with a simplified MF, which is also augmented with the tyre/road friction coefficient as one of the states (modelled as a random walk), with the complete vehicle model discretised using a truncated Lie-Taylor series. Simulation results show that the UKF outperforms the EKF when larger sampling times are used and at lower vehicle speeds due again to linearisation errors. Experimental results using the UKF only show that the proposed solution can successfully estimate the longitudinal and lateral behaviour of the vehicle under different scenarios but also that estimation of the slow varying tyre/road friction coefficient as part of a model-based optimal estimation strategy can be problematic, especially under steady-state conditions.

In [150] we find a model-based MHE strategy for estimation of the vehicle dynamics and the tyre/road friction coefficient. A spatial vehicle dynamics model is combined with with the MF to construct the estimation strategy assuming that the vehicle is equipped with not only an IMU unit but also a GPS and vertical tyre force sensors on the suspension. The resulting optimisation problem is then solved using the RTI scheme as already introduced in chapter 6, and combined with the NMPC strategy for an autonomous vehicle application from [47]. Simulation results using an obstacle avoidance show that the proposed MHE strategy can successfully estimate the vehicle state and position while remaining real-time feasible but also that observability of the tyre/road friction coefficient is lost when no tyre slip occurs, i.e. no torque and steering is applied on the wheels.

From the above we can conclude that:

1. Kinematic-based estimation methods are robust against vehicle parameters uncertainties and changes in the road condition. However, they usually need both IMU

and GPS measurements, are sensitive to sensor bias and errors due to exogenous factors like road bank and inclination angles.

2. Model-based estimation methods are robust against sensor errors and can rely on readily available IMU and Controller Area Network (CAN) bus signals only, but are sensitive to vehicle and especially tyre modelling errors and are dependent on good knowledge of the road condition.

For these reasons, estimation strategies that combine the kinematic and the model-based methods have been also proposed in the literature. An early example of this can be found in [139, 141] which present the attempts of Bosch on the matter, as part of the ESP's continuous development. Here a switching strategy between a kinematic and a model-based sideslip angle estimator is employed: during full braking or heavy cornering (where the assumption of zero pitch and roll used in the kinematic observer are not valid) the model-based method is used whereas during free rolling (where the lateral tyre forces are hard to estimate) the kinematic observer is used instead. While the reasoning behind the switching strategy is sound, no results on the estimation accuracy are presented in [139].

An algorithm that instead of a switching strategy like in [139] employs a combination of a model-based strategy with a kinematic strategy to estimate the sideslip angle is presented in [108]. The model-based estimator is based on a simplified lateral dynamics equation which also includes roll dynamics to find sideslip angle directly from the lateral accelerometer and wheel steering input measurements, while the kinematic estimator uses an integrator to derive the sideslip angle from the kinematic equation for lateral acceleration. Then the two estimations are combined using a low-high pass filter: at low frequencies (which represent close to steady-state manoeuvres) the model-based estimation is mainly used while at higher frequencies (which represent transient manoeuvres) the kinematic estimation dominates instead. Experimental results on high and low

friction surfaces showcase the distinct advantages and disadvantages of each method as already analysed above, with the model-based method following the general trend of the true sideslip angle value well but exhibiting errors due to modelling mismatch, while the kinematic-based method showing significant drift due to the bias error. On the other hand, the proposed algorithm seemed to correct these problems by effectively combining the two methods.

7.3 State Estimation Strategy

In this section, an UKF is formulated to estimate the variables of interest, namely the velocity, sideslip angle and yaw rate of the vehicle. Lets assume we have the continuous-time nonlinear system

$$\dot{x} = f_c(x,u) + w, \tag{7.1a}$$

$$y = g_c(x,u) + v, \tag{7.1b}$$

where $x \in \mathbb{R}^n$ is the state vector, $u \in \mathbb{R}^m$ the input vector, $y \in \mathbb{R}^p$ the output vector, and the process and measurement noises $w \in \mathbb{R}^n$, $v \in \mathbb{R}^p$ are white Gaussian uncorrelated noises with covariance matrices Q_e and R_e respectively. Then, the set of $(2n+1)$ sigma points is

$$\begin{aligned} x^{(0)} &= \xi, \\ x^{(i)} &= \xi + \left[\sqrt{(n+\lambda)L}\right]_i, \; i = 1,...,n, \\ x^{(i)} &= \xi - \left[\sqrt{(n+\lambda)L}\right]_{i-n}, \; i = n+1,...,2n, \end{aligned}$$

where ξ and L are the initial mean value and covariance of x, which in matrix form is [124]

$$X = [\xi \; ... \; \xi] + \sqrt{n+\lambda}\begin{bmatrix} 0_{n\times 1} & \sqrt{L} & -\sqrt{L} \end{bmatrix}.$$

The associated mean and covariance weights are

$$\begin{aligned} W_0^{(mean)} &= \frac{\lambda}{n+\lambda}, \\ W_0^{(cov)} &= \frac{\lambda}{n+\lambda+(1-\alpha_e^2+\beta_e)}, \\ W_i^{(mean)} &= \frac{1}{2(n+\lambda)},\ i=1,...,2n, \\ W_i^{(cov)} &= \frac{1}{2(n+\lambda)},\ i=1,...,2n, \end{aligned}$$

where $\lambda = \alpha_e^2(n+\kappa_e)-n$ is a scaling parameter with α_e, β_e and κ_e as tuning parameters.

Then, assuming also that the input u remains constant for the duration of the sampling time T_e, the two steps for the UKF are [124]:

- *Time update:* The predicted state and measurement means ξ_k^- and ξ_k^y are obtained by propagating the sigma points through the process model (7.2):

$$\begin{aligned} X_{k-1} &= [\xi_{k-1} \dots \xi_{k-1}] + \sqrt{n+\lambda}\left[0 \ \sqrt{L_{k-1}} \ -\sqrt{L_{k-1}}\right], \\ \widehat{X}_k &= f(X_{k-1}, u_{k-1}), \\ \xi_k^- &= \widehat{X}_k w_m, \\ Y_k^- &= g(\widehat{X}_k, u_{k-1}), \\ \xi_k^y &= Y_k^- w_m, \end{aligned}$$

  where the vector w_m is formed from the mean weights

$$w_m = \left[W_0^{(mean)} \dots W_{2n}^{(mean)}\right]^T.$$

  Then the predicted covariance, along with the measurement and cross-covariance

are

$$\begin{aligned} L_k^- &= X_k^- W_k [X_k^-]^T + Q_e, \\ L_k^y &= Y_k^- W_k [Y_k^-]^T + R_k, \\ L_k^{xy} &= X_k^- W_k [Y_k^-]^T, \end{aligned}$$

where $R_k = R_e/T_e$ [46] and the matrix W_k is defined as

$$W_k = \Big(I - [w_m \dots w_m]\Big) \times \text{diag}\Big(W_0^{(cov)} \dots W_{2n}^{(cov)}\Big) \times \Big(I - [w_m \dots w_m]\Big)^T.$$

- *Measurement update:* The filter gain along with the updated state mean and covariance are then

$$\begin{aligned} K_k &= L_k^{xy} [L_k^y]^{-1}, \\ \xi_k &= \xi_k^- + K_k (y_k - \xi_k^y), \\ L_k &= L_k^- - K_k L_k^y K_k^T. \end{aligned}$$

For constructing the UKF, a slightly modified version of the four-wheel vehicle model (3.2) is used: in order to keep the model complexity to a minimum we set the state vector according to the variables of interest, namely the vehicle's velocity, sideslip angle and yaw rate. Assuming that the only available measurements are the longitudinal and lateral acceleration of the vehicle, along with the yaw rate from the IMU unit [1], the wheel speeds and the steering wheel angle from the respective sensors on the wheels and the steering column (measurements commonly found in a production car), we set the input vector to

[1] positioned at a longitudinal and vertical distance of 1.306m and 0.015m respectively from the rear track and with a zero lateral offset

$[\delta \ \omega_{ij}]^T$ and the output vector to $[a_x \ a_y \ \dot{\psi}]^T$. In summary, the continuous-time vehicle model used in the UKF is

$$\begin{aligned} \dot{x} &= f_c(x,u)+w, \\ y &= g_c(x,u)+v, \end{aligned}$$

with state, input and output vectors

$$x=\begin{bmatrix} V \\ \beta \\ \dot{\psi} \end{bmatrix}, \quad u=\begin{bmatrix} \delta \\ \omega_{ij} \end{bmatrix}, \quad y=\begin{bmatrix} a_x \\ a_y \\ \dot{\psi} \end{bmatrix}.$$

Note that by using the wheel speeds as inputs to the estimation model instead of the wheel torques, not only we get a compact formulation for the estimator that allows for faster computations but one that also avoids the requirement for accurate wheel torque measurements. The measurement noise covariance matrix R_e was set according to the noise levels found on typical automotive grade sensors (Table 7.1) while the process noise covariance matrix Q_e which represents parameter uncertainties and unmodeled dynamics was found through extensive simulation studies. Finally, the sampling time is chosen at T_e =5ms, while for the prediction step one step of the explicit Runge-Kutta 4th order integration method is used, the latter giving an excellent approximation of the continuous dynamics for our system at the chosen sampling time.

	a_x	a_y	$\dot{\psi}$	δ	ω_{ij}
Mean	0	0	0	0	0
Variance	$3\cdot10^{-3}$	$6\cdot10^{-3}$	$5\cdot10^{-6}$	$2\cdot10^{-6}$	$5.7\cdot10^{-2}$

Table 7.1: Noise mean and variance values per signal.

7.4 Evaluation of the Estimation Strategy

In this section, we test the above derived estimator in two scenarios, the first one evaluating the UKF when the vehicle is driven around a track without using active control and the second one checking the performance of the complete system, where the UKF is combined with the NMPC-PDIP strategy from chapter 6 in an obstacle avoidance manoeuvre according to ISO 3888-2:2011 [23].

7.4.1 Race Circuit Driving Scenario

In the first scenario the driver model in CarMaker is used to drive the vehicle around the Motodrom section of the Hockenheim race circuit, as available in CarMaker (more details on the track can be found in Appendix F). It is assumed at this point that no active control is in place: the acceleration commands from the driver are translated into a total torque demand which is then split equally between the rear left and rear right electric motors, while the deceleration commands are fulfilled using the four brakes on the four wheels through a standard hydraulic brake system.

Figs. 7.1a-7.1c show how the state estimation from the UKF compares against the true values as obtained by CarMaker. The results are excellent, with only the sideslip angle estimation (Fig. 7.1b) showing some small deviation from the true value. Note that the large spike in the beginning of the sideslip angle estimation (Fig. 7.1b) is the direct result of initialising the estimator far away from the true value, with the initial estimated velocity value set to 5m/s however the UKF quickly converges to the true state values which shows that it is also robust to initialization errors. Finally, from Fig. 7.2 we can see that the computational time for the UKF remains around 0.2ms for the duration of this scenario and never exceeds the 1ms.

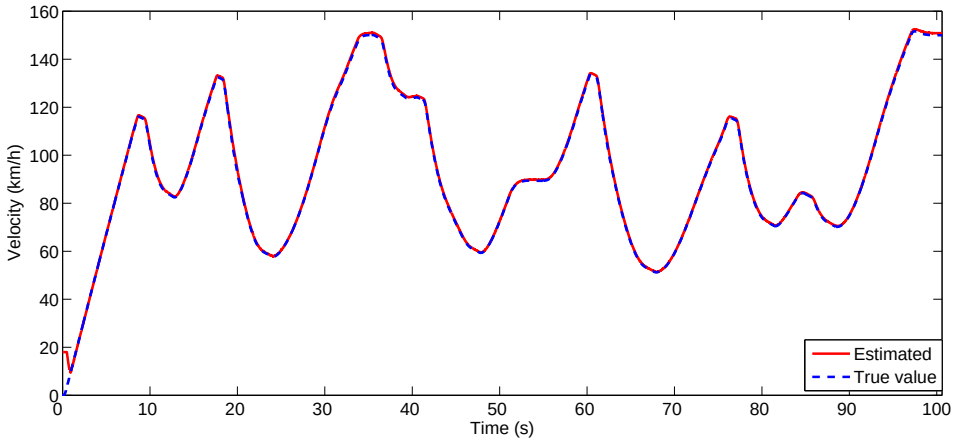

(a) Velocity

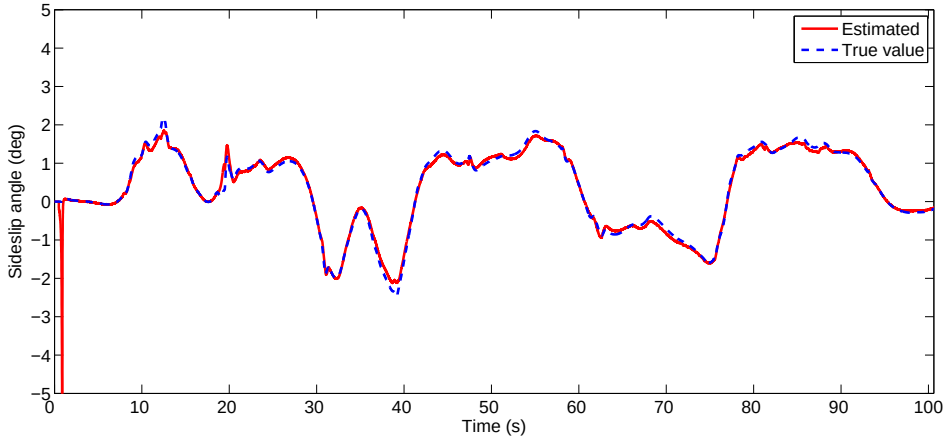

(b) Sideslip angle

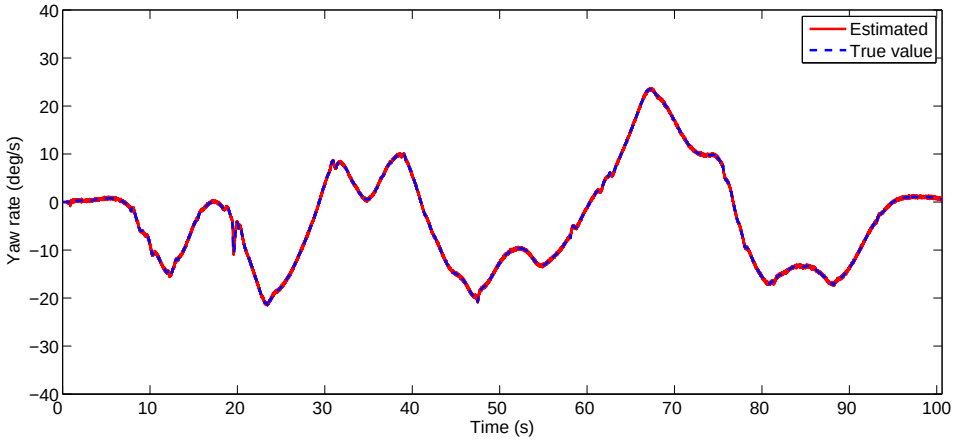

(c) Yaw rate

Figure 7.1: Comparison of the true value (in blue) and the estimated one (in red) for the velocity, sideslip angle and yaw rate of the vehicle in the race circuit driving scenario.

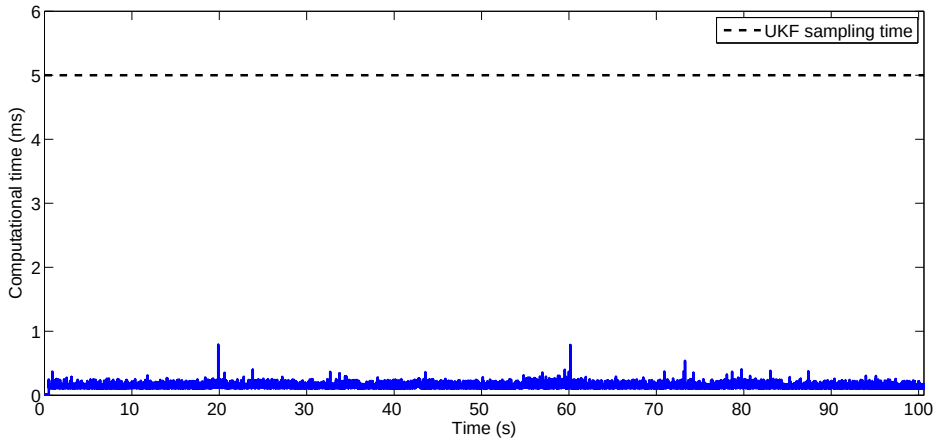

Figure 7.2: Computational time for the UKF in the race circuit driving scenario.

7.4.2 Obstacle Avoidance Scenario

For the obstacle avoidance scenario we return to the double-lane change – as defined by the ISO 3888-2:2011 [23] – of section 6.5.2 and test the complete solution by combining the NMPC-PDIP strategy from the beginning of section 6.5 with the UKF as presented in this chapter. In order to properly quantify the effect of using an estimator in the controller performance, we compare the response of the vehicle with the complete solution against a vehicle that uses the NMPC-PDIP strategy but assumes that the true state values are available instead. Note that the road is assumed again dry ($\mu_{max} = 1$), the entry speed is set to 75km/h, while no acceleration or braking commands come from the driver. Note that the velocity error weight is set to q_V =500 as before in chapter 6.

Figs. 7.3a-7.3b show the trajectory of the vehicle using the NMPC-PDIP in blue and the vehicle using the NMPC-PDIP with the UKF in red. Application of the UKF for estimation of the vehicle states seems to have a small effect on the trajectory of the vehicle, with only a slight deviation towards the end of the manoeuvre where the vehicle using the UKF comes closer to the right-hand side cones. Looking at Figs 7.3d-7.3f, we can see

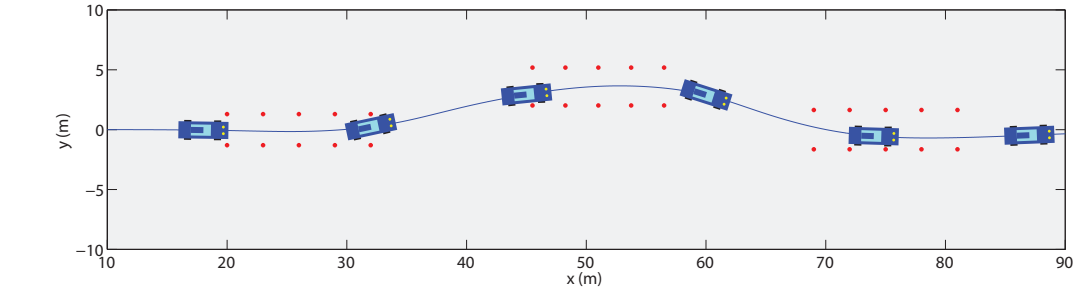

(a) NMPC-PDIP trajectory

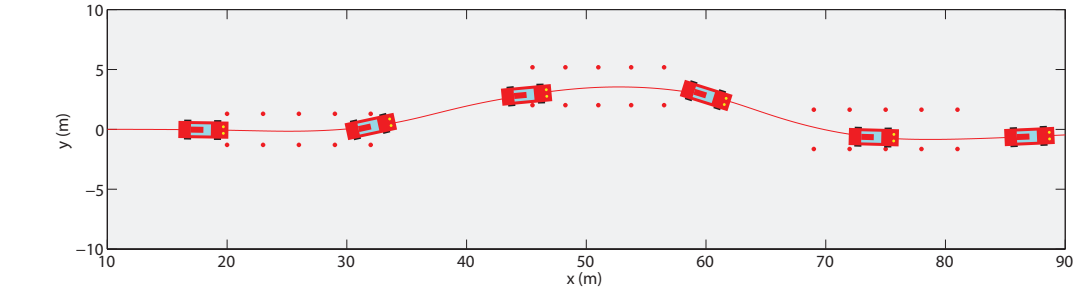

(b) NMPC-PDIP with UKF trajectory

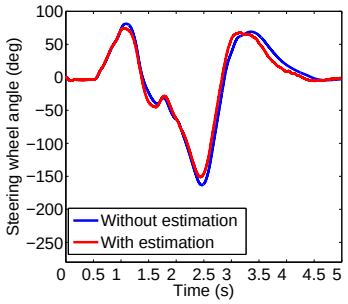

(c) Steering wheel angle

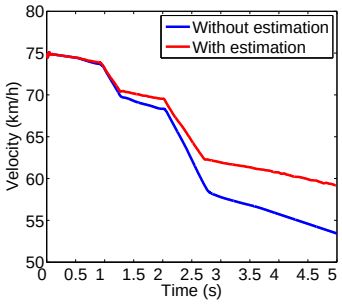

(d) Velocity

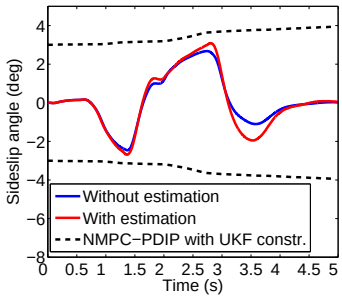

(e) Sideslip angle

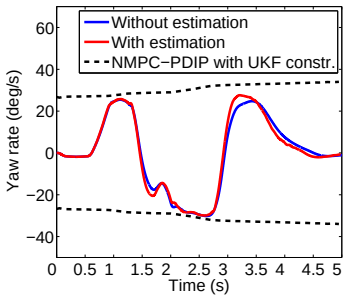

(f) Yaw rate

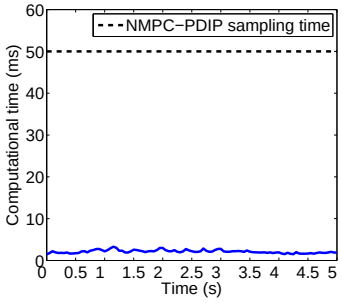

(g) NMPC-PDIP comp. time

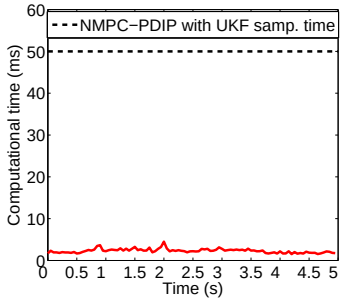

(h) NMPC-PDIP UKF comp. time

Figure 7.3: Comparison of the vehicle using the estimated state from the UKF (in red) and the vehicle using the true state values (in blue) in the obstacle avoidance scenario.

that the velocity, sideslip angle and yaw rate response of the two vehicles is similar, with only noticeable difference the larger velocity for the vehicle with the UKF. Finally, using the UKF to provide the state information seems to have no effect on the computational time of the NMPC-PDIP strategy, as seen in Figs 7.3g-7.3h.

In Figs. 7.6a-7.4f we see the (actual) longitudinal slip and the (commanded) torque on the two rear wheels for the two vehicles. The most noticeable difference from application of the UKF is the introduction of high frequency noise into the system. This is particularly apparent in the case of the commanded torques on the wheels from the low level Sliding Mode Slip Controller (Fig. 7.4f), which in turn introduces the high frequency noise on the longitudinal slip as evidenced in Figs. 7.4d-7.4e. It is important to note at this point

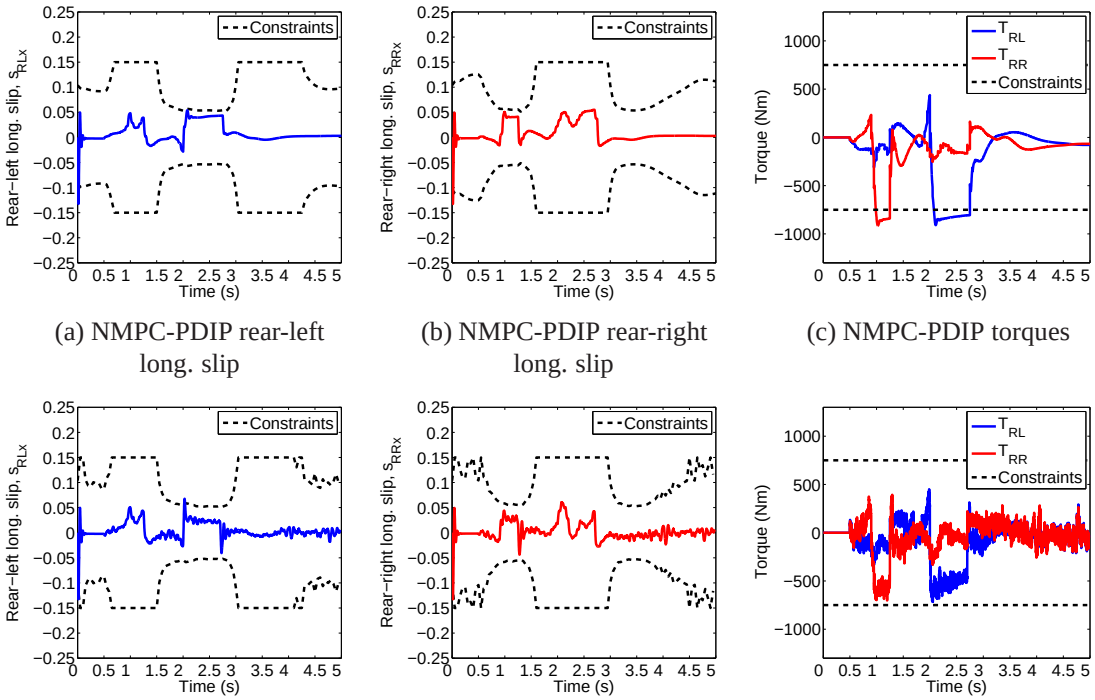

(a) NMPC-PDIP rear-left long. slip

(b) NMPC-PDIP rear-right long. slip

(c) NMPC-PDIP torques

(d) NMPC-PDIP UKF rear-left long. slip

(e) NMPC-PDIP UKF rear-right long. slip

(f) NMPC-PDIP UKF torques

Figure 7.4: Longitudinal slip (actual) and torque (requested) time histories for the vehicle using the estimated state from the UKF and the vehicle using the true state values in the obstacle avoidance scenario.

that according to its definition (5.18) the Sliding Mode Slip Controller requires estimates of the longitudinal slips and forces along with the longitudinal velocity rates on the rear tyres: using the available measurements on the steering angle and wheel speeds along with the estimated velocity, sideslip angle and yaw rate values from the UKF, the longitudinal slips and forces on the tyres can be found using definitions (3.3) and (3.10), while the longitudinal velocity rates $\dot{V}_{RLx}$ and $\dot{V}_{RRx}$ can be found by differentiating the V_{RLx} and V_{RRx} expressions from section 3.2.1:

$$\left.\begin{aligned} V_{RLx} &= V\cos\beta - \dot{\psi}\ell_{RL}\sin\gamma_{RL} \\ V_{RRx} &= V\cos\beta + \dot{\psi}\ell_{RR}\sin\gamma_{RR} \end{aligned}\right\} \quad \left.\begin{aligned} \dot{V}_{RLx} &= \dot{V}\cos\beta - V\dot{\beta}\sin\beta - \ddot{\psi}\ell_{RL}\sin\gamma_{RL} \\ \dot{V}_{RRx} &= \dot{V}\cos\beta - V\dot{\beta}\sin\beta + \ddot{\psi}\ell_{RR}\sin\gamma_{RR} \end{aligned}\right\}$$

Looking past the noise contamination on Figs. 7.4d-7.4f, using the UKF does not affect the general response of the vehicle on the tyre level and the time histories look similar, with the main difference found on the smaller negative torque peaks of Fig.7.4f. These are directly related to the smaller rear-left and rear-right longitudinal slip peaks at 2-2.5s and 1-1.5s respectively (Figs. 7.4d-7.4e) and consequently result to the smaller reduction in the vehicle velocity throughout the manoeuvre as already evidenced in Fig. 7.3d.

The high frequency noise observed in the commanded torques from the Sliding Mode Slip Controller in Figs. 7.4d-7.4f is not related to the velocity, sideslip angle and yaw rate estimation from the UKF: as we can see from Figs. 7.5a-7.5c the state estimation values from the UKF remain close to the true values and show no high frequency oscillations. Looking at the longitudinal slip estimation on the rear wheels in Figs 7.6a-7.6b however, we can immediately observe that the estimated values exhibit a high frequency noise similar to the one we first encountered in Figs. 7.4d-7.4f. It turns out that setting the wheel speeds as the input to the UKF internal model, passes the high frequency wheel speed sensor noise directly into the longitudinal slip calculation (3.3), a problem that could

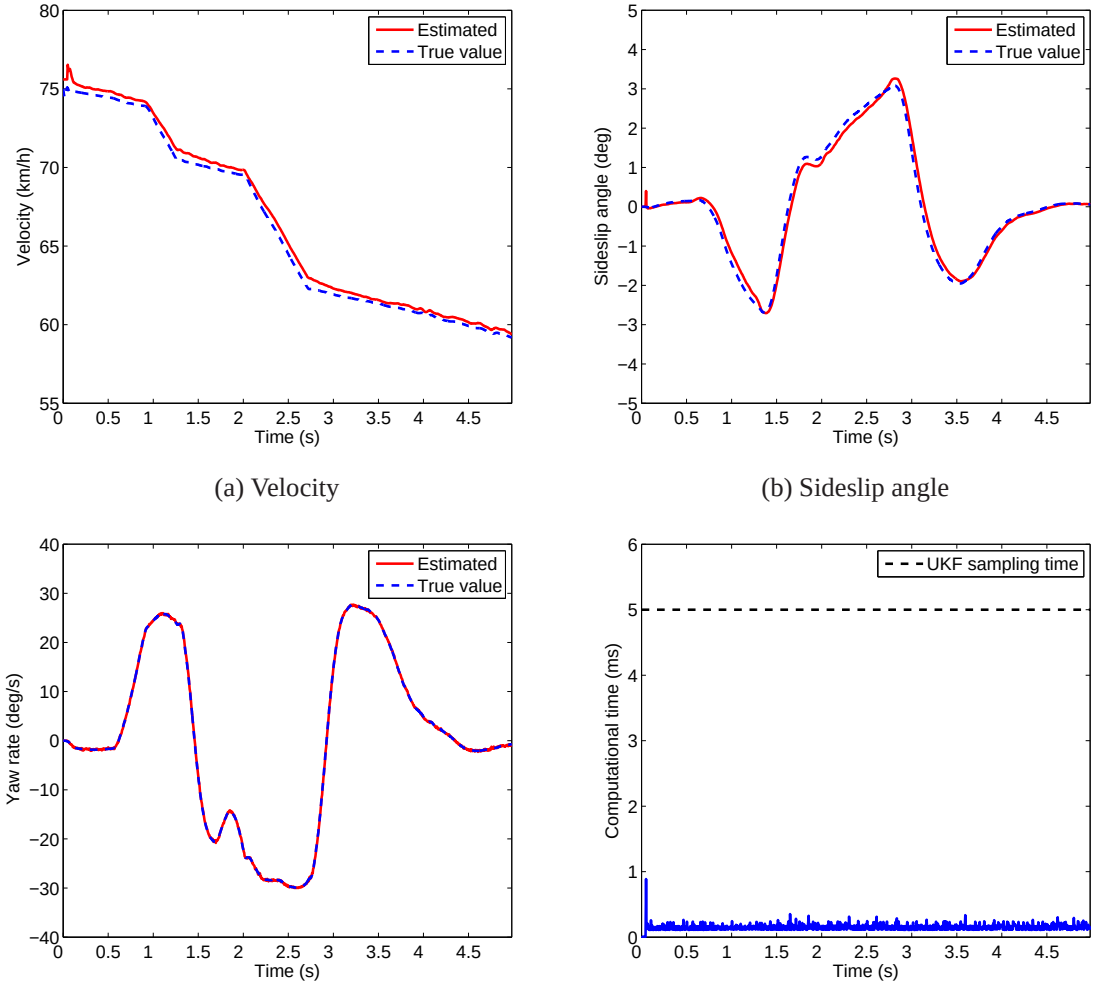

(a) Velocity

(b) Sideslip angle

(c) Yaw rate

(d) UKF comp. time

Figure 7.5: Comparison of the true value (in blue) and the estimated one (in red) for the velocity, sideslip angle and yaw rate of the vehicle along with the computational time for the UKF in the obstacle avoidance scenario.

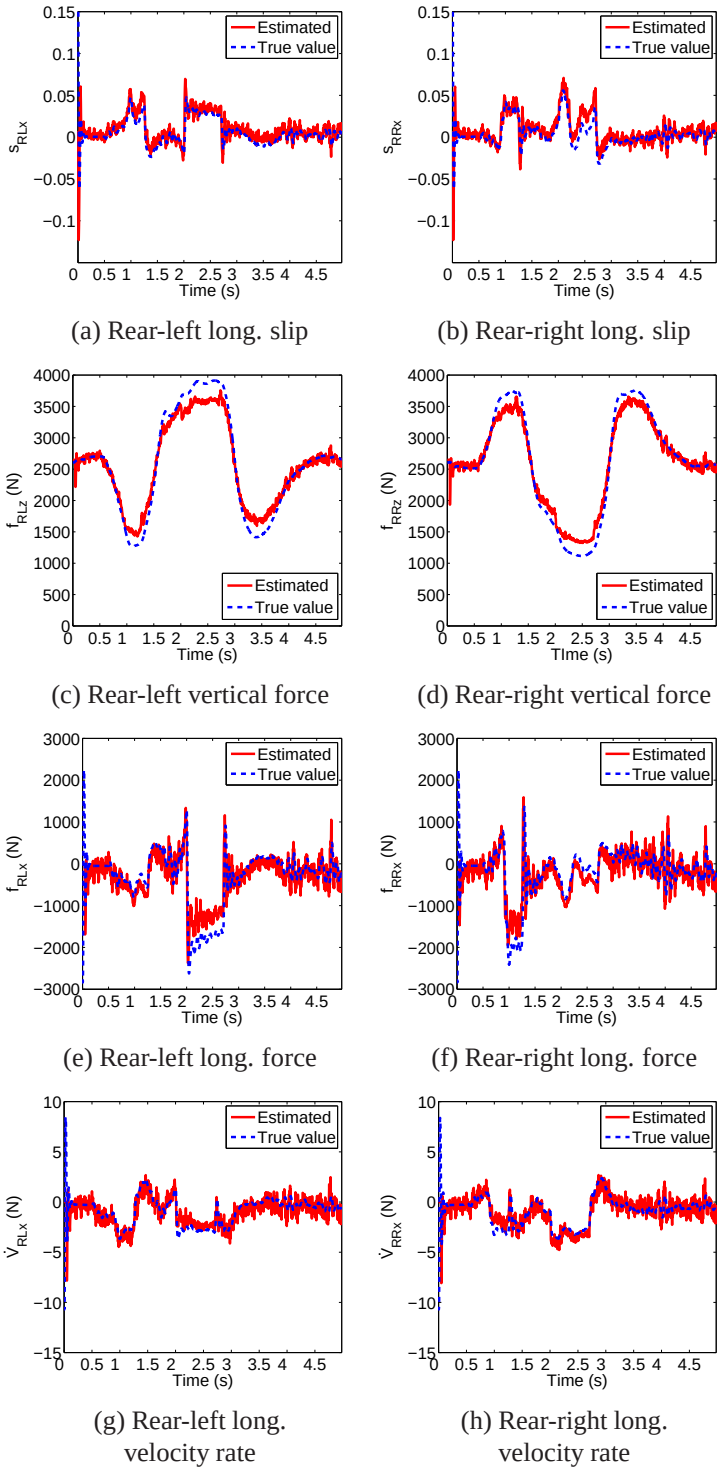

(a) Rear-left long. slip

(b) Rear-right long. slip

(c) Rear-left vertical force

(d) Rear-right vertical force

(e) Rear-left long. force

(f) Rear-right long. force

(g) Rear-left long. velocity rate

(h) Rear-right long. velocity rate

Figure 7.6: Comparison of the true value (in blue) and the estimated one (in red) for the longitudinal slips, vertical and longitudinal forces and longitudinal velocity rates on the rear-left and rear-right tyres in the obstacle avoidance scenario.

be possibly reduced by separately filtering the wheel speed sensors' signals using for example a low-pass frequency filter but at the expense of added delay into the calculation.

The noisy longitudinal slip estimates result in noisy longitudinal force estimates (Figs. 7.6e-7.6f) and ultimately to noisy torque commands from the Sliding Mode Slip Controller, as originally seen in Fig. 7.4f. Note that the estimation errors observed at around 2-2.5s for the rear-left longitudinal force and 1-1.5s for the rear-right longitudinal force are due to underestimation of the rear-left and rear-right vertical forces at this point (Figs. 7.6c-7.6d), something that is connected to the fact that we have not integrated any suspension dynamics to the internal model for the UKF. Finally the estimation of longitudinal velocity rates as required by the Sliding Mode Slip Controller and seen in Figs. 7.6g-7.6h is accurate but again noisy.

From the above analysis we can see that using an UKF in the obstacle avoidance scenario results in degradation of the overall performance of the vehicle, which is mostly related to the low level Sliding Mode Slip Controller requiring accurate longitudinal force estimates: the use of the unfiltered wheel speed sensor signals in the longitudinal slip calculation and the omission of the suspension dynamics from the internal model for the UKF had a negative effect on the longitudinal forces estimation. However, it is important to note that the performance degradation is small and the vehicle using the NMPC-PDIP strategy with the UKF still manages to pass the obstacle avoidance test successfully.

7.5 Summary

A nonlinear optimal estimator for estimating the vehicle dynamics was presented in this chapter. The use of a small internal model for the UKF which also assumed that the only measurements available come from inexpensive sensors usually fitted on a standard vehicle resulted in a compact formulation that did not depend on accurate wheel torque

measurements.

Simulation tests on a track without any active control in place showed that the derived UKF can estimate the velocity, sideslip angle and yaw rate of the vehicle fast and effectively. A second simulation test coupling the UKF with the NMPC-PDIP strategy from the previous chapter in the obstacle avoidance scenario from section 6.5.2 showed that use of the UKF to provide the state information to the controller resulted in only a small change in the overall performance, with the vehicle equipped with the complete solution successfully completing the ISO 3888-2:2011 [23] test.

Chapter 8

Conclusions

8.1 Concluding Remarks

This project presented the application of optimal control strategies for stabilisation of an RWD EV at the limits of handling using combined longitudinal and lateral dynamics control. While the necessity to regulate the vehicle velocity especially in cases of terminal understeer behaviour has been shown before, to the best of the author's knowledge all solutions so far presented do not consider nonlinear tyre characteristics and coupled longitudinal and lateral vehicle dynamics and tyre forces: this simplifies the problem but ultimately asks for more tuning effort. Furthermore, all the developed optimal controllers are implementable in real-time. To this end, computational times on a standard desktop machine (i7-2600k at 3.40GHz with 16GB of memory) were reported throughout the work presented, while the final solution was also deployed on a dSPACE DS1005 board (PowerPC 750GX at 1.00GHz with 128MB of memory).

After reviewing the most important contributions in the active control of the vehicle dynamics with a particular focus on the limit handling solutions, the four-wheel vehicle model and the nonlinear tyre model used in the control design and the reference generation was presented. Use of the nonlinear vehicle model ensures that the computed references, which are specific to the given drivetrain topology, are always feasible.

Use of an unconstrained optimal control strategy in the form of an LQR showed that terminal understeer can be eliminated by appropriately controlling both the longitudinal and lateral vehicle dynamics so that the driver's intended path is followed. However, it also showed that accounting for the system constraints is important in limit handling conditions.

The importance of constraining both the vehicle state and the control inputs in limit handling cases has been demonstrated through the development and application of two linear MPC strategies. The use of a smaller vehicle model by disregarding the fast wheel speed dynamics has been explored, with results showing that excluding them results not only in a smaller optimization problem that is easier to solve, but also allows for relaxed sampling times. A systematic way was then used to define the tuning parameters for the two MPC strategies, with the prediction and control horizon, along with the sampling time all chosen through an analysis of the relative trade-off in closed-loop performance and computational cost. Testing the two MPC strategies under two different test scenarios, one using a U-turn and another one an obstacle avoidance manoeuvre showed that the vehicle can be successfully stabilised in critical conditions by regulating both the longitudinal and lateral dynamics of the vehicle while respecting the state and input constraints in order to follow the intended path from the driver.

The use of an NMPC formulation have been presented next, along with the use of a specialised solver to dramatically reduce the computational cost of the QP problem used in the linear MPC case as presented before. Comparing the strategies against the optimal

solution in terms of closed-loop performance and computational cost in a series of case studies has revealed that while the linear MPC remains the fastest strategy it also returns suboptimal solutions that can greatly deviate from the optimal solution. Deployment of the NMPC strategy on a dSPACE board has also showed that the final solution can be potentially tested on a real vehicle with minimal performance penalty. The importance of using a nonlinear system dynamics representation as found in an NMPC strategy was also confirmed in two limit handling manoeuvres: using a U-turn scenario with excessive entry speed and a obstacle avoidance manoeuvre like before it was shown that the NMPC strategy achieves a better state regulation while also commanding smoother torque inputs.

Lastly, the effect of noise and uncertainties in the state information provided to the NMPC strategy has been examined. For this, an UKF for estimating the dynamics of the vehicle has been developed, assuming that the only measurements available come from inexpensive sensors usually fitted on a standard vehicle. After validating the proposed estimation strategy on a test track without any active control in place, coupling it with the NMPC strategy in the obstacle avoidance scenario showed that the complete solution can still successfully stabilise the vehicle in an optimal way.

8.2 Future Work

The work presented in this thesis can be extended in the near future to:

- Test the proposed strategies in Hardware-In-the-Loop (HIL) simulation and on a test vehicle: when developing the optimal control strategies, real-time applicability was always one of the main concerns. For this reason computational times were always recorded as to make sure that the proposed solutions can be implemented in real-time, while an estimation strategy was also used to check how noise and uncertainties in the provided state information can affect the controller's response.

However, it would be interesting to see how the most promising of the proposed optimal control strategies perform on a real system where problems such as CAN delays can have a deteriorating effect on the controller's performance.

- Explore different low level slip control solutions: the Sliding Mode Slip Controller used in the MPC and NMPC strategies has provided a good, fast response to changing longitudinal slip targets. However, it requires information about not only the vehicle velocity, sideslip angle and yaw rate but also the longitudinal tyre forces and the longitudinal velocity rates on the rear wheels, which makes its application on a real vehicle rather difficult. Initial investigations on a low level slip control strategy using the NMPC framework have revealed that indeed a simpler low level slip control strategy which requires only information on the vehicle velocity, sideslip angle and yaw rate along with the wheel speeds can be devised.

- Examine different drivetrain topologies: the developed optimal control strategies applied an RWD EV can be easily compared against similar solutions on different drivetrain topologies like the ones found on an FWD or an AWD vehicle. Especially in the case of an AWD vehicle which results in an inherently overactuated system, the inclusion of secondary objectives in the cost function would also allow to take into account other performance criteria like energy consumption or electric motor degradation, with initial investigations on the subject using a simple LQR strategy showing promising results [73].

- Integrate with a brake-by-wire system: control of the individual wheel brake torques through a brake-by-wire system would greatly enhance the authority of the proposed strategies, which currently rely on the two electric motors on the rear axle of the vehicle to control both its longitudinal and lateral dynamics. While that would demand for a blending strategy between the friction brake torque and the electric

motor torque on each of the rear wheels, initial investigations on the subject using the NMPC framework [14] have shown that this can be achieved in an optimal way.

- Introduce acceleration/deceleration commands from the driver: this project examined how the vehicle can be optimally stabilised in limits handling cases, assuming that the driver provides the intended vehicle path through the steering wheel but does not use the acceleration or brake pedals. It would be therefore interesting to examine how the proposed solutions can be extended to take into account such commands from the driver: the resulting solution would operate in both sub-limit and limit handling conditions by continuously providing the necessary torques on the wheels based on all the inputs from the driver while making sure that the vehicle always remains stable.

- Include estimation of the tyre/road friction coefficient: while an UKF was developed in this project to provide the variables of interest as part of the controller's validation, information on the tyre/road friction coefficient was assumed known. An initial analysis on this topic by incorporating estimation of μ_{max} to the developed UKF have produced results similar to the ones found in the literature [5, 150], with estimation of μ_{max} quickly deviating from its true value when the system is not excited. Possible solutions to this would be to use a switching strategy that would apply estimation of μ_{max} only when the system is excited enough or use a constrained optimal estimator which would limit the value of μ_{max} in the range of its possible values. No matter the approach chosen, it is important to address how the necessary information of the road condition can be provided if any of the proposed strategies is to be tested on a real vehicle.

Appendix A

Vehicle and Tyre Parameters

The vehicle considered in this work is a small electric sports car with two independent electric motors on the rear axle, each motor able to deliver a continuous power of 75kW and having a speed-torque characteristic curve as seen in Fig. A.1. A list of the vehicle and tyre parameters for both the CarMaker model and the simplified vehicle model found in chapter 3 and used for the controllers' synthesis in this work can be found in Table A.1. Note that in the case of the CarMaker model, a full MF5.2 tyre model of a Bridgestone Potenza RE50A 205/45R17 tyre has been used.

A comparison of the tyre curves under pure longitudinal and lateral slip at the nominal tyre load of 5500N for the tyre model used in CarMaker and the simplified MF used in this work is shown in Fig. A.2: it can been seen that the simplified MF is a good approximation of the tyre's force generation in the longitudinal and lateral directions. In the same Fig. A.2 we can also see that the maximum normalised force is achieved at a slip value of around 0.15.

A comparison of the simplified vehicle model as introduced in chapter 3 with the high fidelity CarMaker model can be seen in Fig. A.3, where the vehicle is initially moving straight with a velocity of 16m/s and a steering wheel input of 90deg (corresponding

Parameter	Value	Parameter	Value
m (kg)	1137	k_F (N/m)	48300
I_x (kgm^2)	191	k_R (N/m)	48300
I_y (kgm^2)	1058	c_F (Ns/m)	3000
I_z (kgm^2)	1174	c_R (Ns/m)	3000
ℓ_{veh} (m)	4.15	k_{aF} (Nm/rad)	777
w_{veh} (m)	1.623	k_{aR} (Nm/rad)	0
h_{veh} (m)	1.226	m_w (kg)	14
δ_{ratio}	0.787	I_w (kgm^2)	1.04
w_L (m)	2.5	R_w (m)	0.298
w_R (m)	1.374	B_{MF}	11.24
ℓ_F (m)	1.187	C_{MF}	1.45
ℓ_R (m)	1.313	D_{MF}	1
h (m)	0.317	c_{aero}	0.27

Table A.1: Vehicle and tyre parameters.

to around 5.6deg on the front wheels) is applied at t =3s after a transitional time of 1s (Fig. A.3a). Note that the initial vehicle velocity corresponds to the maximum feasible velocity for the chosen steering angle according to the analysis of section 3.3. Fig. A.3b shows the difference in the vehicle velocity between the simplified and the CarMaker vehicle model (in the case of the CarMaker model the initial vehicle velocity is adjusted so that it is approximately equal to the simplified vehicle model velocity at t =3s): the slower velocity drop in the case of the simplified vehicle model can be attributed to the absence of resistive forces such as the aerodynamic force and tyre rolling resistances from this model. Figs. A.3c-A.3d show that the sideslip angle and yaw rate time histories for the simplified and the Carmaker model. While the general pattern for both the sideslip angle and the yaw rate is similar between the two models, the simplified vehicle model exhibits slightly larger values (maximum difference from the CarMaker model of 0.44deg and 3.17deg/s respectively), which can be connected to the slower velocity drop for this model. From the above analysis, the simplified vehicle model of chapter 3 is deemed appropriate for designing the controllers presented in this project.

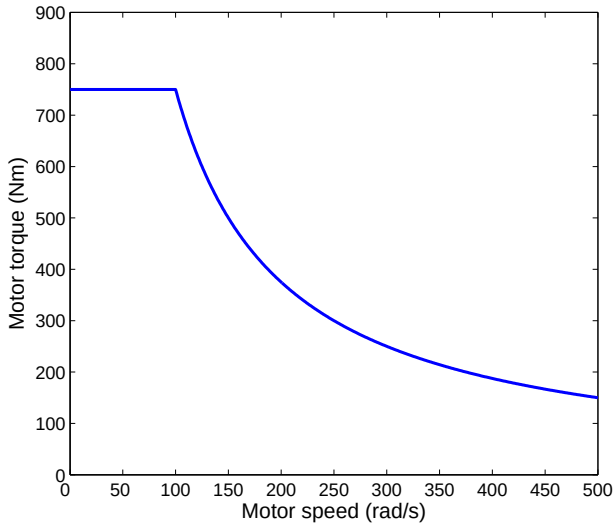

Figure A.1: Static torque map of YASA-750 motor.

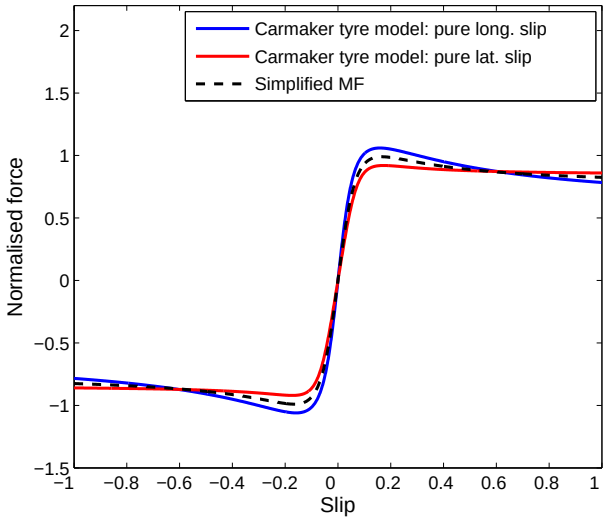

Figure A.2: CarMaker's tyre model versus simplified MF.

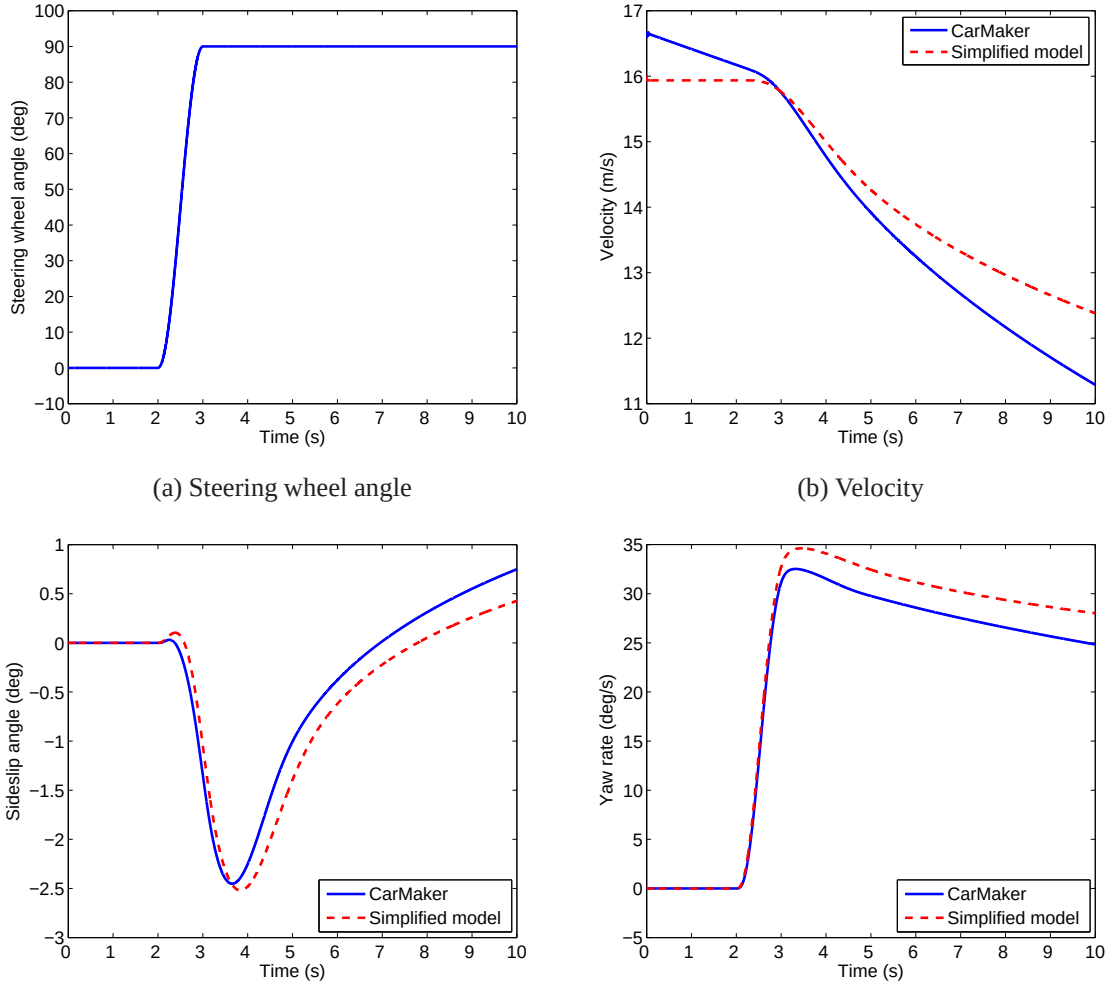

(a) Steering wheel angle

(b) Velocity

(c) Sideslip angle

(d) Yaw rate

Figure A.3: CarMaker model versus simplified vehicle model.

Appendix B

Direct Yaw Control Strategy

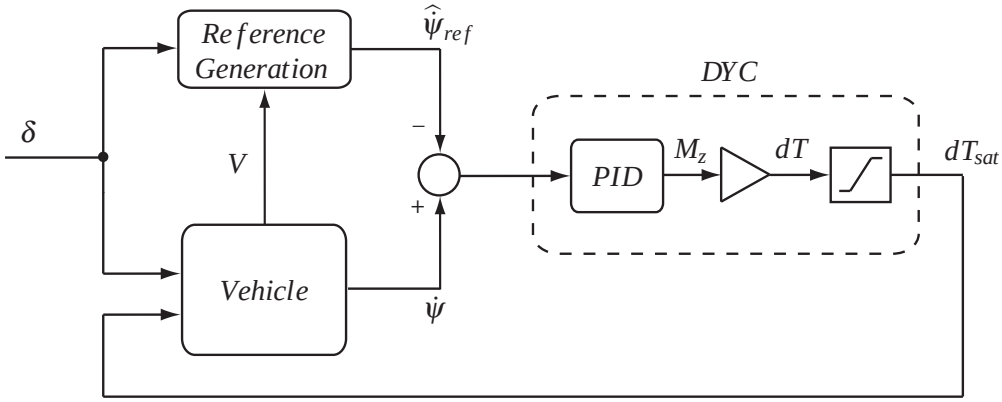

Figure B.1: DYC structure.

The Direct Yaw Control strategy used in the U-turn scenario of section 4.4 is detailed here. As we can see from Fig. B.1, the DYC takes the error between the actual vehicle yaw rate and the requested yaw rate from the driver through the steering angle and tries to correct it by applying a torque of equal magnitude and opposite sign on the two rear wheels.

The yaw rate reference $\dot{\psi}_{ref}$ is set under steady state cornering conditions as a function

of the current vehicle velocity V and steering angle δ:

$$\dot{\psi}_{ref} = \frac{V}{R_{kin}} = \frac{\delta V}{\ell_F + \ell_R}, \tag{B.1}$$

where R_{kin} has been replaced by $\frac{\ell_F+\ell_R}{\delta}$ according to (3.12), assuming δ is small enough so that the small angle approximation assumption is valid.

The reference yaw rate is saturated according to the available tyre/road friction coefficient μ_{max}, in the same way to (5.7):

$$|\dot{\psi}_{ref}| \leq \mu_{max}\frac{g}{V}. \tag{B.2}$$

Combining Equations (B.1) and (B.2) it follows that the saturated reference yaw rate can be defined as:

$$\widehat{\dot{\psi}}_{ref} = \begin{cases} \dot{\psi}_{ref}, & \text{if} \quad |\dot{\psi}_{ref}| \leq \mu_{max}\frac{g}{V} \\ \mu_{max}\frac{g}{V}\text{sign}(\dot{\psi}_{ref}), & \text{if} \quad |\dot{\psi}_{ref}| > \mu_{max}\frac{g}{V} \end{cases} \tag{B.3}$$

where the multiplication with sign$(\dot{\psi}_{ref})$ accounts for a negative steering input (right turn) on the vehicle.

Having obtained the desired yaw rate reference, the necessary M_z request is then calculated using a gain scheduled PID, where the proportional, integral and derivative gains are set as functions of the current velocity. Finally the M_z request is converted into a torque request of equal magnitude and opposite sign on the two rear wheels through the simple relationship:

$$dT = \frac{R_w}{w_R + w_L}M_z. \tag{B.4}$$

The above dT request is limited according to the motor map limits (Fig. A.1) to give the saturated value dT_{sat} to be applied on the two electric motors on the rear axle.

Appendix C

Linear MPC in Dense Form

For the nonlinear continuous-time dynamical system

$$\dot{x} = f_c(x,u), \tag{C.1}$$

we can linearise about the equilibrium point $(x^{\mathrm{ss}}, u^{\mathrm{ss}})$ to get

$$\dot{x} = Ax + Bu - (Ax^{\mathrm{ss}} + Bu^{\mathrm{ss}}), \tag{C.2}$$

with $(Ax^{\mathrm{ss}} + Bu^{\mathrm{ss}})$ a constant which can be treated as a disturbance. Assuming also that the input is modelled as a zero-order hold, discretising the above affine system gives [46]

$$x_{k+1} = A_d x_k + B_d u_k + c, \tag{C.3}$$

with

$$A_d = e^{AT_s}, \qquad B_d = \int_0^{T_s} e^{A\eta}\mathrm{d}\eta\mathrm{B}, \qquad \mathrm{c} = -\int_0^{\mathrm{T_s}} \mathrm{e}^{\mathrm{A}\eta}\mathrm{d}\eta(\mathrm{Ax}^{\mathrm{ss}} + \mathrm{Bu}^{\mathrm{ss}}).$$

Then the general linear MPC problem with prediction horizon N is

$$\min_{x,u} \quad (x_N - r)^T S_d (x_N - r) + \sum_{k=0}^{N-1} \Big[(x_k - r)^T Q_d (x_k - r) + (u_k - l)^T R_d (u_k - l) + 2 (x_k - r)^T M_d (u_k - l) \Big], \tag{C.4a}$$

$$\text{subject to} \quad x_0 = x_{in}, \tag{C.4b}$$

$$x_{k+1} = A x_k + B u_k + c, \quad k = 0, 1, ..., N-1, \tag{C.4c}$$

$$u_k^l \leq u_k \leq u_k^h, \quad k = 0, 1, ..., N-1, \tag{C.4d}$$

$$x_k^l \leq x_k \leq x_k^h, \quad k = 1, 2, ..., N, \tag{C.4e}$$

where (C.4a) is the cost to minimise with r and l the state and input references respectively, (C.4b) sets the initial state x_0 equal to the current one, (C.4c) are the affine discrete system dynamics and (C.4d)-(C.4e) are the state and input inequality constraints. The positive (semi-)definite matrix Q_d and positive definite matrix R_d are the weighting matrices on the state error and control effort respectively, and the positive definite matrix M_d is the cross-weighting matrix. A terminal penalty $(x_N - r)^T S_d (x_N - r)$ is also included, with the matrix S_d selected as the solution of the DARE

$$S_d = A^T S_d A + Q_d (B^T S_d A + M_d^T)^T (R_d + B^T S_d B)^{-1} (B^T S_d A + M_d^T).$$

For the dense MPC formulation the system dynamics (C.4c) are used to eliminate the state from both the cost function (C.4a) and the inequality constraints (C.4d)-(C.4e) [93, 128]. This results in an optimization problem with only the input sequence as the optimization variable, but also one that involves computing powers of the state matrix A, hence the possibility of an ill-conditioned problem when a long prediction horizon is used [93].

Expressing the discrete system dynamics (C.4c) in terms of the initial state x_{in}:

$$\bar{x} = \Phi x_{in} + \Gamma \bar{u} + Kc, \tag{C.5}$$

where

$$\bar{x} = [x_1^T \; x_2^T \; ... \; x_N^T]^T, \qquad \bar{u} = [u_0^T \; u_1^T \; ... \; u_{N-1}^T]^T, \tag{C.6}$$

and

$$\Phi = \begin{bmatrix} A \\ A^2 \\ . \\ . \\ A^N \end{bmatrix}, \qquad \Gamma = \begin{bmatrix} B & 0 & ... & 0 \\ AB & B & ... & 0 \\ . & . & ... & . \\ . & . & ... & . \\ A^{N-1}B & . & ... & B \end{bmatrix}, \qquad K = \begin{bmatrix} I \\ A+I \\ . \\ . \\ A^{N-1}+...+I \end{bmatrix}. \tag{C.7}$$

We can then use (C.5) to eliminate the state entries from both the cost function (C.4a) and the inequality constraints (C.4d)-(C.4e), as detailed in the subsequent sections.

C.1 Inequality Constraints

The state and input inequality constraints (C.4d)-(C.4e) in matrix form are

$$\begin{bmatrix} 0 \\ 0 \\ I \\ -I \end{bmatrix} x_i + \begin{bmatrix} I \\ -I \\ 0 \\ 0 \end{bmatrix} u_i \leq \begin{bmatrix} u_i^h \\ -u_i^l \\ x_i^h \\ -x_i^l \end{bmatrix}, \qquad i = 0, 1, ..., N,$$

which can be also compactly written as

$$W_i x_i + E_i u_i \leq d_i, \qquad i = 0, 1, ..., N.$$

Introducing the slack variable $\varepsilon \in \mathbb{R}^+$ on the state inequality constraints gives

$$W_i x_i + E_i u_i + W_{\varepsilon i} \varepsilon \leq d_i, \qquad i = 0, 1, ..., N,$$

with $W_{\varepsilon i} = \begin{bmatrix} 0 & 0 & -1^{1\times n} & -1^{1\times n} \end{bmatrix}^T$.

Then, using (C.6) and (C.4b) the above set of inequalities becomes

$$W\bar{x} + E\bar{u} + W_\varepsilon \varepsilon \leq d, \tag{C.8}$$

where

$$W = \begin{bmatrix} 0 & 0 & ... & 0 \\ W_1 & 0 & ... & 0 \\ 0 & W_2 & ... & 0 \\ . & . & ... & . \\ 0 & . & ... & W_N \end{bmatrix}, E = \begin{bmatrix} E_0 & 0 & ... & 0 \\ 0 & E_1 & ... & 0 \\ . & . & ... & . \\ 0 & 0 & ... & E_{N-1} \\ 0 & 0 & ... & 0 \end{bmatrix}, W_\varepsilon = \begin{bmatrix} 0 \\ W_{\varepsilon 1} \\ . \\ . \\ W_{\varepsilon N} \end{bmatrix}, \tag{C.9}$$

and $d = [(d_0 - W_0 x_{in}) \;\; d_1 \;\; ... \;\; d_N]^T$, and replacing $\bar{x}$ according to (C.5) we get

$$(W\Gamma + E)\bar{u} + W_\varepsilon \varepsilon \leq d - W\Phi x_{in} - WKc. \tag{C.10}$$

Finally, since the slack variable ε needs to be always greater than or equal to zero, the above matrix equality becomes

$$G\begin{bmatrix} \bar{u} \\ \varepsilon \end{bmatrix} \leq g(x_{in}), \tag{C.11}$$

where

$$G = \begin{bmatrix} W\Gamma + E & W_\varepsilon \\ 0 & -1 \end{bmatrix}, \qquad g(x_{in}) = \begin{bmatrix} d - W\Phi x_{in} - WKc \\ 0 \end{bmatrix}.$$

C.2 Cost Function

For $\bar{r} = [r \ldots r]^T$, $\bar{l} = [l \ldots l]^T$, and $\bar{x}$, $\bar{u}$ according to (C.6), the cost to minimise is equal to

$$\begin{aligned} J(\bar{x},\bar{u}) &= {x_{in}}^T Q_d x_{in} - {x_{in}}^T (Q_d - Q_d^T) r + r^T Q_d r + 2(x_{in} - r)^T M u_0 \\ &\quad + \bar{x}^T \Omega \bar{x} - \bar{x}^T (\Omega + \Omega^T) \bar{r} + \bar{r}^T \Omega \bar{r} + \bar{u}^T \Psi \bar{u} - \bar{u}^T (\Psi + \Psi^T) \bar{l} \\ &\quad + \bar{l}^T \Psi \bar{l} - 2(x_{in} - r) M l_0 + 2\bar{x}^T \Pi \bar{u} - 2\bar{r}^T \Pi \bar{u} - 2\bar{x}^T \Pi \bar{l} + 2\bar{r}^T \Pi \bar{l}, \end{aligned} \tag{C.12}$$

where x_0 has been replaced by x_{in} according to (5.4b) and [128]

$$\Omega = \begin{bmatrix} Q_d & 0 & \ldots & 0 \\ 0 & Q_d & \ldots & 0 \\ . & . & \ldots & . \\ 0 & . & \ldots & S_d \end{bmatrix}, \quad \Psi = \begin{bmatrix} R & 0 & \ldots & 0 \\ 0 & R & \ldots & 0 \\ . & . & \ldots & . \\ 0 & . & \ldots & R \end{bmatrix}, \quad \Pi = \begin{bmatrix} 0 & M & 0 & \ldots & 0 \\ 0 & 0 & M & \ldots & 0 \\ . & . & . & \ldots & . \\ 0 & 0 & 0 & \ldots & M \\ 0 & 0 & 0 & \ldots & 0 \end{bmatrix}.$$

Then, using (C.5)-(C.7) we can rewrite (C.12) as function of the input sequence $\bar{u}$ only

$$J(\bar{u}) = \frac{1}{2}\bar{u}^T H\bar{u} + \bar{u}^T Dx_{in} + b(x_{in}), \tag{C.13}$$

where

$$\begin{aligned} H &= 2(\Psi + \Gamma^T \Omega \Gamma + 2\Pi^T \Gamma), \\ D &= 2\overline{M}(x_{in} - r) + [\Gamma^T(\Omega + \Omega^T) + 2\Pi^T]\Phi x_{in} - [\Gamma^T(\Omega + \Omega^T) + 2\Pi^T]\bar{r} \\ &\quad - [(\Psi + \Psi^T) + 2\Gamma^T \Pi]\bar{l} + [\Gamma^T(\Omega + \Omega^T) + 2\Pi^T]Kc, \end{aligned}$$

with $\overline{M} = [M\ 0\ \ldots\ 0]$ and $b(x_{in})$ a constant term throughout the horizon N which is a function of the given initial state only.

Dropping the constant term $b(x_{in})$ and also introducing the necessary penalization of the slack variable ε, the cost function to minimise is then

$$J(\bar{u}, \varepsilon) = \frac{1}{2}\bar{u}^T H\bar{u} + \bar{u}^T Dx_{in} + b(x_{in}) + \rho_\varepsilon \varepsilon. \tag{C.14}$$

C.3 The QP Problem

From (C.11) and (C.14) the dense soft-constrained MPC problem is

$$\text{minimize} \quad J(\bar{u}, \varepsilon), \tag{C.15a}$$

$$\text{subject to} \quad G \begin{bmatrix} \bar{u} \\ \varepsilon \end{bmatrix} \leq g(x_{in}). \tag{C.15b}$$

This is a standard QP problem that can be solved using any of the popular QP solvers available in the literature.

Appendix D

Linear MPC using a Specialised Solver

The use of a generic solver for the solution of the linear MPC problem (C.15) can result in slow computational times which, even after the analysis presented in chapter 5, can make a real-time implementation of the resulting linear MPC controller difficult. For this reason, we investigate here the difference in performance between the generic QP solver used in chapter 5 which employed the active set method as available through the `quadprog` solver in MATLAB and a specialised solver FORCES Pro solver [36] which employs the PDIP method.

For the comparison between the two solvers, we return to the U-turn scenario of section 5.6.1 and solve a slightly modified QP problem, whereas the two soft constraints $\varepsilon_{\dot{\psi}}, \varepsilon_{\beta} \in \mathbb{R}^{+}$ throughout the prediction horizon are replaced by one soft constraint $\varepsilon_i \in \mathbb{R}^{+}$ $(i = 1, ..., N)$ on the sideslip angle and yaw rate constraint violations per stage. This modification is necessary if we are to use the sparse FORCES Pro solver – which does not allow for multi-stage optimization variables – but does not diminish the conclusions of the comparison presented here in any way. Then, the QP problem to solve is

$$
\begin{aligned}
\min_{x,u} \quad & (x_N - r)^T S_d (x_N - r) + \sum_{k=0}^{N-1} \Big[(x_k - r)^T Q_d (x_k - r) \\
& + (u_k - l)^T R_d (u_k - l) + 2 (x_k - r)^T M_d (u_k - l) + q_\varepsilon \varepsilon_{i+1} \Big], \\
\text{subject to} \quad & x_0 = x_{in}, \\
& x_{k+1} = A x_k + B u_k + c, \quad k = 0, 1, ..., N-1, \\
& u_k^l \leq u_k \leq u_k^h, \quad k = 0, 1, ..., N-1, \\
& x_k^l - \varepsilon_k \leq x_k \leq x_k^h + \varepsilon_k, \quad k = 1, 2, ..., N, \\
& \varepsilon_k \geq 0, \quad k = 1, ..., N.
\end{aligned}
$$

Fig. D.1 shows the velocity, sideslip angle and yaw rate time histories, along with the computational times for the modified optimization problem as presented above using the `quadprog` and FORCES Pro solver in the U-turn scenario from section 5.6.1. As we can see from Fig. D.1 while the state time histories are as expected identical (Figs. D.1a-D.1c), the time to construct and solve the optimization problem is very different for the two solvers (Fig. D.1d), with the FORCES Pro managing to return a solution in less than 2ms in every call. This shows that the use of a specialised QP solver can dramatically reduce the computational time for the MPC problem.

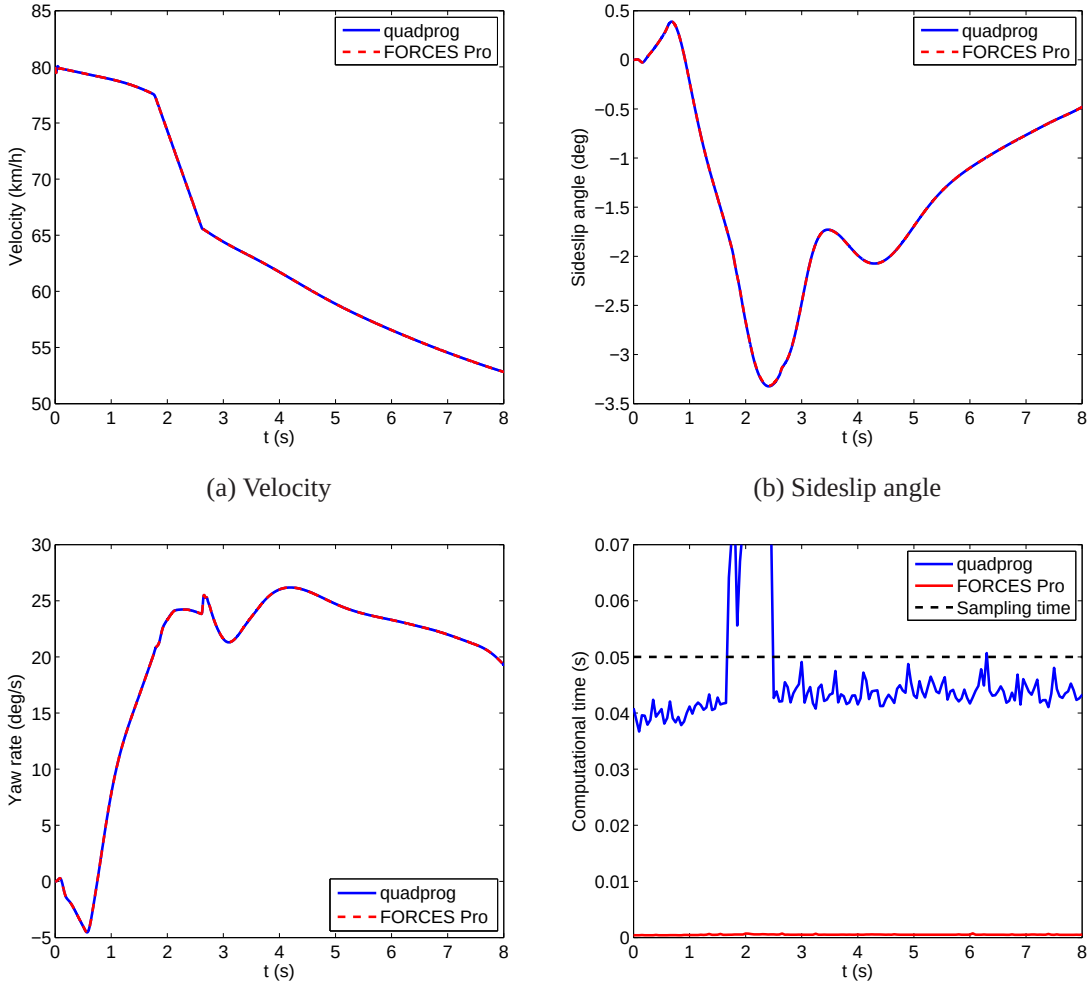

(a) Velocity

(b) Sideslip angle

(c) Yaw rate

(d) Comp. time

Figure D.1: Comparison of `quadprog` and FORCES Pro solver in the U-turn scenario.

Appendix E

Characteristic Speed Calculation

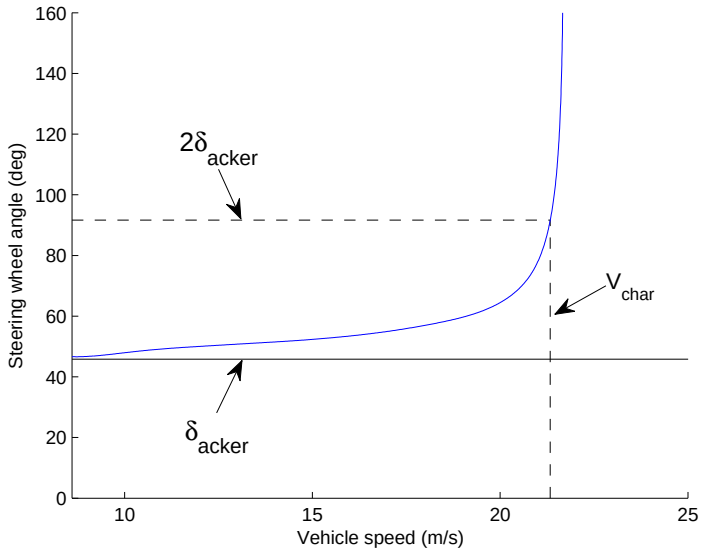

Figure E.1: Wheel steering input change with vehicle speed for the constant radius turn test.

The characteristic speed of a vehicle V_{char} is defined under steady-state cornering conditions as the speed at which a steering angle double the Ackerman angle is required for the vehicle to maintain the same turning radius [50]. For the vehicle considered here the characteristic speed was found using a constant radius test in CarMaker, whereas the

driver model in CarMaker was used to gradually increase the speed of the vehicle while trying to stay on a circular path of 50m radius. Given that the vehicle's wheelbase is 2.5m the Ackerman angle is

$$\delta_{acker} = \frac{L}{R} = 0.05rad, \tag{E.1}$$

which, assuming a steering ratio of 16:1, corresponds to around 45deg on the steering wheel. As we can see from Fig. E.1, the driver needs to keep increasing the steering wheel angle in order to keep the same turning radius as the vehicle's speed increases and reaches a wheel steering angle double the Ackerman angle at V_{char} =21.5m/s.

Appendix F

Tracks Specifications

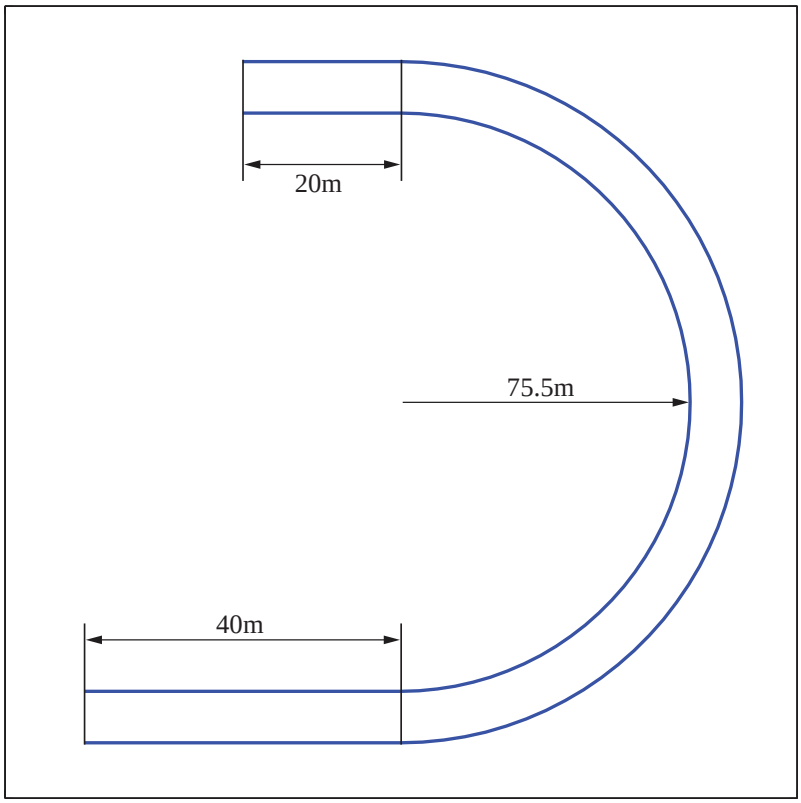

Figure F.1: Road profile for the U-turn scenario in chapters 4-6. The road width is 6.5m.

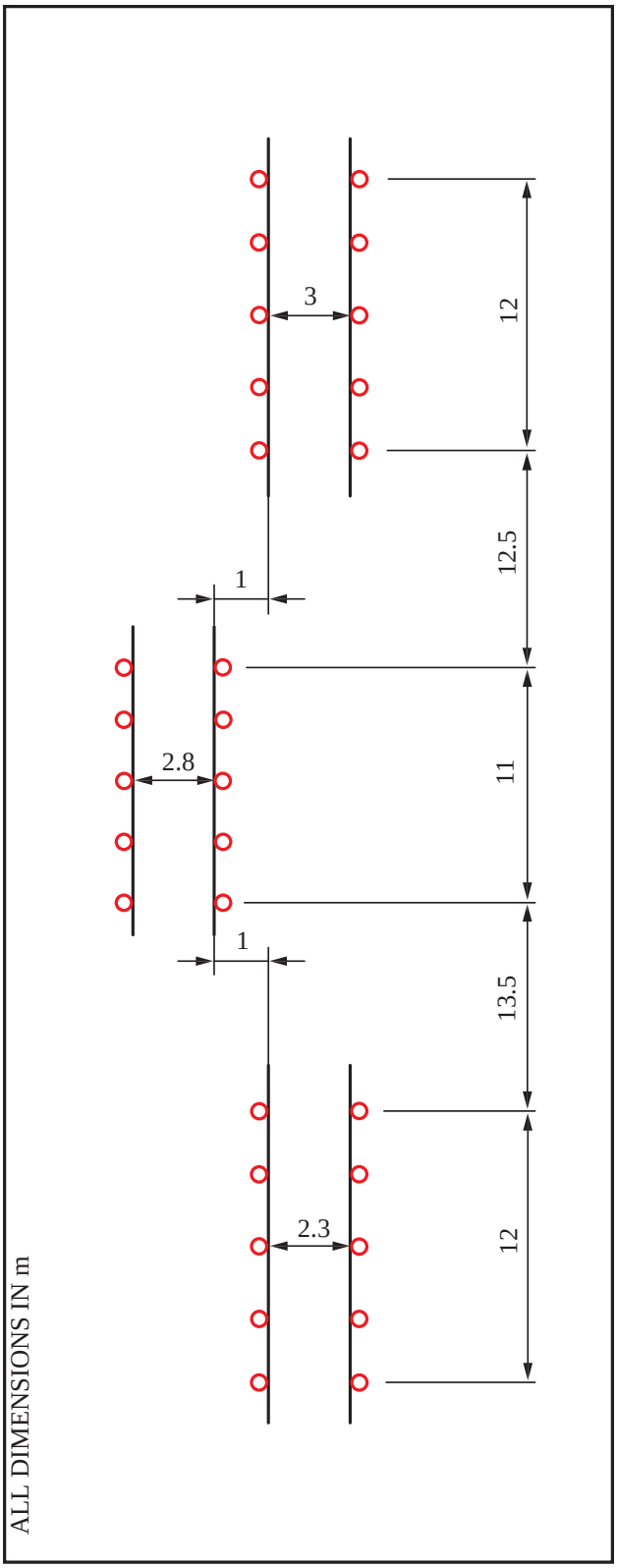

Figure F.2: ISO 3888-2:2011 [23] test specifications according to the vehicle parameters as found in Appendix A.

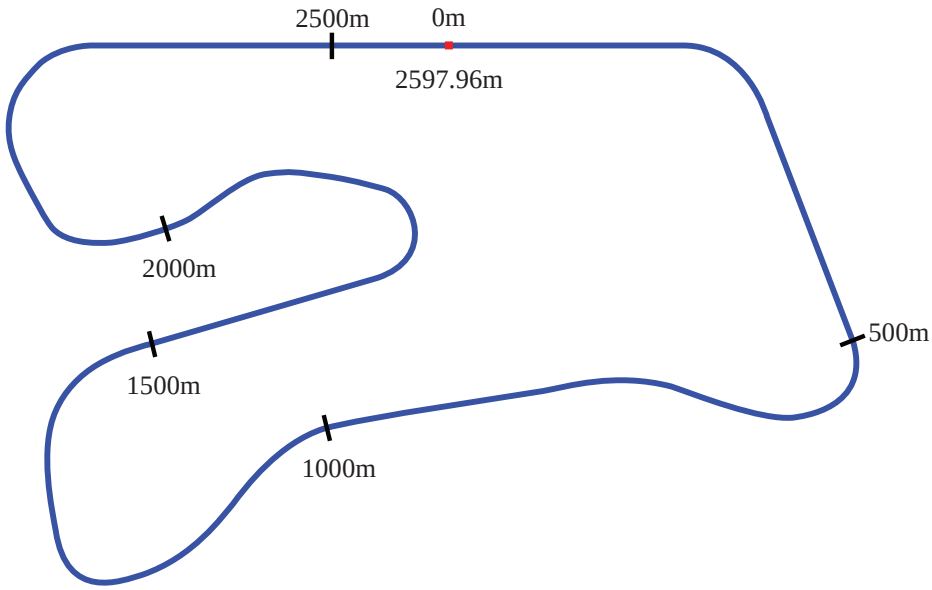

Figure F.3: Motodrom section of the Hockenheim track, as found in CarMaker and used in chapter 7. The track width is 12m.

References

[1] E-VECTOORC project (2011-2014). `http://www.e-vectoorc.eu/`. Last accessed: 2015-03-05.

[2] eFuture project (2010-2013). `http://www.efuture-eu.org/`. Last accessed: 2014-09-12.

[3] J. Ackermann and W. Sienel. Robust yaw damping of cars with front and rear wheel steering. *Control Systems Technology, IEEE Transactions on*, 1(1):15–20, 1993.

[4] M. Ali, P. Falcone, C. Olsson, and J. Sjoberg. Predictive prevention of loss of vehicle control for roadway departure avoidance. *IEEE Transactions on Intelligent Transportation Systems*, 14(1):56–68, March 2013.

[5] S. Antonov, A. Fehn, and A. Kugi. Unscented Kalman Filter for vehicle state estimation. *Vehicle System Dynamics*, 49(9):1497–1520, 2011.

[6] K. Astrom and B. Wittenmark. *Computer-Controlled Systems*. Prentice-Hall, 3rd edition, 1997.

[7] M. A. Athans and P. L. Falb. *Optimal Control*. McGraw-Hill, New York, 1966.

[8] R. Attia, R. Orjuela, and M. Basset. Coupled longitudinal and lateral control strategy improving lateral stability for autonomous vehicle. In *2012 American Control Conference (ACC)*, pages 6509–6514, June 2012.

[9] G. Baffet, A. Charara, and J. Stephant. Sideslip angle, lateral tire force and road friction estimation in simulations and experiments. In *2006 IEEE Conference on Computer Aided Control System Design, 2006 IEEE International Conference on Control Applications, 2006 IEEE International Symposium on Intelligent Control*, pages 903–908, Oct 2006.

[10] E. Bakker, L. Nyborg, and H. B. Pacejka. Tyre modelling for use in vehicle dynamics studies. *SAE Technical Paper 870421*, 1987.

[11] O. Barbarisi, G. Palmieri, S. Scala, and L. Glielmo. LTV-MPC for yaw rate control and side slip control with dynamically constrained differential braking. *European Journal of Control*, 15(34):468 – 479, 2009.

[12] M. Bartels, Qin Liu, G. Kaiser, and H. Werner. LPV torque vectoring for an electric vehicle using parameter-dependent Lyapunov functions. In *American Control Conference (ACC), 2013*, pages 2153–2158, 2013.

[13] S. C. Baslamisli, I. Polat, and I. E. Kose. Gain scheduled active steering control based on a parametric bicycle model. In *Intelligent Vehicles Symposium, 2007 IEEE*, pages 1168–1173, 2007.

[14] M. S. Basrah, E. Siampis, E. Velenis, D. Cao, and S. Longo. Integration of torque blending and slip control using real-time nonlinear model predictive control. In *Proceedings of AVEC 2016*, Munich, Germany, September 2016.

[15] C. E. Beal and J. C. Gerdes. Model Predictive Control for vehicle stabilization at the limits of handling. *Control Systems Technology, IEEE Transactions on*, 21(4):1258–1269, July 2013.

[16] D. Bernardiniy, S. Di Cairanoz, A. Bemporad, and H. E. Tsengz. Drive-by-wire vehicle stabilization and yaw regulation: a hybrid Model Predictive Control design. In *Decision and Control, 2009 held jointly with the 2009 28th Chinese Control Conference. CDC/CCC 2009. Proceedings of the 48th IEEE Conference on*, pages 7621–7626, Dec 2009.

[17] D. M. Bevly, J. C. Gerdes, C. Wilson, and Gengsheng Zhang. The use of GPS based velocity measurements for improved vehicle state estimation. In *American Control Conference, 2000. Proceedings of the 2000*, volume 4, pages 2538–2542 vol.4, 2000.

[18] D. M. Bevly, J. Ryu, and J. C. Gerdes. Integrating INS sensors with GPS measurements for continuous estimation of vehicle sideslip, roll, and tire cornering stiffness. *IEEE Transactions on Intelligent Transportation Systems*, 7(4):483–493, Dec 2006.

[19] D. M. Bevly, R. Sheridan, and J. C. Gerdes. Integrating ins sensors with gps velocity measurements for continuous estimation of vehicle sideslip and tire cornering stiffness. In *American Control Conference, 2001. Proceedings of the 2001*, volume 1, pages 25–30 vol.1, 2001.

[20] D. Bianchi, A. Borri, G. Burgio, M. D. Di Benedetto, and S. Di Gennaro. Adaptive integrated vehicle control using active front steering and rear torque vectoring. In *Decision and Control, 2009 held jointly with the 2009 28th Chinese Control*

Conference. CDC/CCC 2009. Proceedings of the 48th IEEE Conference on, pages 3557–3562, 2009.

[21] F. Borrelli, P. Falcone, T. Keviczky, J. Asgari, and D. Hrovat. MPC-based approach to active steering for autonomous vehicle systems. *International Journal of Vehicle Autonomous Systems*, 3(2-4):265–291, 2005.

[22] Jr. Bryson, A. E. and Y. C. Ho. *Applied Optimal Control*. Blaisdell, Waltham, 1969.

[23] BS ISO 3888-2:2011. Passenger cars – Test track for a severe lane-change manoeuvre Part 2: Obstacle avoidance. Standard, British Standards Institution, London, GB, 2011.

[24] S. Di Cairano. 4th IFAC conference on nonlinear model predictive control, an industry perspective on MPC in large volumes applications: Potential benefits and open challenges. *IFAC Proceedings Volumes*, 45(17):52 – 59, 2012.

[25] S. Di Cairano and H. E. Tseng. Driver-assist steering by active front steering and differential braking: Design, implementation and experimental evaluation of a switched model predictive control approach. In *49th IEEE Conference on Decision and Control (CDC)*, pages 2886–2891, Dec 2010.

[26] M. Canale and L. Fagiano. Vehicle yaw control using a fast NMPC approach. In *Decision and Control, 2008. CDC 2008. 47th IEEE Conference on*, pages 5360–5365, Dec 2008.

[27] M. Canale, M. Milanese, and C. Novara. Semi-active suspension control using fast model-predictive techniques. *Control Systems Technology, IEEE Transactions on*, 14(6):1034–1046, Nov 2006.

[28] D. Casanova. *On minimum-time vehicle manoeuvring: The theoretical optimal lap*. PhD thesis, Cranfield University, 2000.

[29] C. C. Chan, Y. S. Wong, A. Bouscayrol, and K. Chen. Powering sustainable mobility: Roadmaps of electric, hybrid, and fuel cell vehicles. *Proceedings of the IEEE*, 97(4):603–607, 2009.

[30] D. Charters, M. Watkinson, D. Wykes, and B. Simpkin. H4V-Hybrid Four Wheel Drive vehicle. In *Hybrid and Eco-Friendly Vehicle Conference, 2008. IET HEVC 2008*, pages 1–4, Dec 2008.

[31] U. Chong, E. Namgoong, and S. Sul. Torque steering control of 4-wheel drive electric vehicle. In *Power Electronics in Transportation, 1996., IEEE*, pages 159–164, 1996.

[32] D. A. Crolla and D. Cao. The impact of hybrid and electric powertrains on vehicle dynamics, control systems and energy regeneration. *Vehicle System Dynamics*, 50(sup1):95–109, 2012.

[33] L. De Novellis, A. Sorniotti, and P. Gruber. Optimal wheel torque distribution for a Four-Wheel-Drive fully electric vehicle. *SAE Technical Paper 2013-01-0673*, 2013.

[34] S. Di Cairano, H. E. Tseng, D. Bernardini, and A Bemporad. Vehicle yaw stability control by coordinated active front steering and differential braking in the tire sideslip angles domain. *Control Systems Technology, IEEE Transactions on*, 21(4):1236–1248, July 2013.

[35] M. Diehl, H. G. Bock, J. P. Schlder, R. Findeisen, Z. Nagy, and F. Allgower. Real-time optimization and nonlinear model predictive control of processes governed

by differential-algebraic equations. *Journal of Process Control*, 12(4):577 – 585, 2002.

[36] A. Domahidi and J. Jerez. FORCES Professional. embotech GmbH (`http://embotech.com/FORCES-Pro`), Jul 2014.

[37] M. Doumiati, A. Victorino, A. Charara, G. Baffet, and D. Lechner. An estimation process for vehicle wheel-ground contact normal forces. {*IFAC*} *Proceedings Volumes*, 41(2):7110 – 7115, 2008. 17th {IFAC} World Congress.

[38] M. Doumiati, A. C. Victorino, A. Charara, and D. Lechner. Onboard real-time estimation of vehicle lateral tire-road forces and sideslip angle. *IEEE/ASME Transactions on Mechatronics*, 16(4):601–614, Aug 2011.

[39] H. Dugoff, P. Fancher, and L. Segel. An analysis of tire properties and their influence on vehicle dynamic performance. *SAE Technical Paper 700377*, 1970.

[40] E. Frazzoli E. Velenis and P. Tsiotras. Steady-state cornering equilibria and stabilization for a vehicle during extreme operating conditions. *International Journal of Vehicle Autonomous Systems, Special Issue on Autonomous and Semi-Autonomous Control for Safe Driving of Ground Vehicles*, 8(2-3):217241, 2010.

[41] P. Falcone, F. Borrelli, J. Asgari, H. E. Tseng, and D. Hrovat. A model predictive control approach for combined braking and steering in autonomous vehicles. In *Control Automation, 2007. MED '07. Mediterranean Conference on*, pages 1–6, June 2007.

[42] P. Falcone, F. Borrelli, J. Asgari, H.E. Tseng, and D. Hrovat. Predictive active steering control for autonomous vehicle systems. *Control Systems Technology, IEEE Transactions on*, 15(3):566–580, May 2007.

[43] P. Falcone, H. Eric Tseng, F. Borrelli, J. Asgari, and D. Hrovat. MPC-based yaw and lateral stabilisation via active front steering and braking. *Vehicle System Dynamics*, 46(sup1):611–628, 2008.

[44] P. Falcone, M. Tufo, F. Borrelli, J. Asgari, and H. E. Tseng. A linear time varying model predictive control approach to the integrated vehicle dynamics control problem in autonomous systems. In *Decision and Control, 2007 46th IEEE Conference on*, pages 2980–2985, Dec 2007.

[45] F. Feustel, S. Lang, and M. Hand. The electric super sports car SLS AMG electric drive. *ATZ Magazine*, 115:5–10, 2013.

[46] G. F. Franklin, J. D. Powell, and M. Workman. *Digital Control of Dynamic Systems*. Addison Wesley Longman, Menlo Park, CA, 3rd edition, 1998.

[47] J. V. Frasch, A. Gray, M. Zanon, H. J. Ferreau, S. Sager, F. Borrelli, and M. Diehl. An auto-generated nonlinear MPC algorithm for real-time obstacle avoidance of ground vehicles. In *Control Conference (ECC), 2013 European*, pages 4136–4141, July 2013.

[48] Y. Furukawa and M. Abe. Advanced chassis control systems for vehicle handling and active safety. *Vehicle System Dynamics*, 28(2-3):59–86, 1997.

[49] C. Geng, L. Mostefai, M. Denai, and Y. Hori. Direct yaw-moment control of an in-wheel-motored electric vehicle based on body slip angle fuzzy observer. *Industrial Electronics, IEEE Transactions on*, 56(5):1411–1419, 2009.

[50] T. D. Gillespie. *Fundamentals of Vehicle Dynamics*. Society of Automotive Engineers SAE International, Warrendale PA USA, 1992.

[51] N. Giorgetti, A Bemporad, I. V. Kolmanovsky, and D. Hrovat. Explicit hybrid optimal control of direct injection stratified charge engines. In *Industrial Electronics, 2005. ISIE 2005. Proceedings of the IEEE International Symposium on*, volume 1, pages 247–252, June 2005.

[52] Robert Bosch Gmbh. *Bosch Handbook for Safety, Comfort and Convenience Systems*. Bentley, Cambridge, USA, 2006.

[53] T. J. Gordon, M. Klomp, and M. Lidberg. Control mitigation for over-speeding in curves: Strategies to minimize off-tracking. In *11th International Symposium on Advanced Vehicle Control*, Seoul, Korea, September 9-12 2012.

[54] A. Gray, M. Ali, Y. Gao, J. K. Hedrick, and F. Borrelli. Integrated threat assessment and control design for roadway departure avoidance. In *2012 15th International IEEE Conference on Intelligent Transportation Systems*, pages 1714–1719, September 2012.

[55] M. J. Griffin. *Handbook of Human Vibration*. Academic Press, London, 1990.

[56] P. He, Y. Hori, M. Kamachi, K. Walters, and H. Yoshida. Future motion control to be realized by in-wheel motored electric vehicle. In *Industrial Electronics Society, 2005. IECON 2005. 31st Annual Conference of IEEE*, 2005.

[57] G. Heeb and A. van Zanten. System approach to vehicle dynamic control. *SAE Technical Paper 885107*, 1988.

[58] B. R. Hoehn, K. Stahl, P. Gwinner, and F. Wiesbeck. Torque-vectoring driveline for electric vehicles. In *Proceedings of the FISITA 2012 World Automotive Congress*, volume 191 of *Lecture Notes in Electrical Engineering*, pages 585–593. Springer Berlin Heidelberg, 2013.

[59] Y. Hori, Y. Toyoda, and Y. Tsuruoka. Traction control of electric vehicle: Basic experimental results using the test EV UOT Electric March. *Industry Applications, IEEE Transactions on*, 34(5):1131–1138, 1998.

[60] B. Houska, H. J. Ferreau, and M. Diehl. An auto-generated real-time iteration algorithm for nonlinear MPC in the microsecond range. *Automatica*, 47(10):2279–2285, 2011.

[61] K. Huh, D. Hong, P. Yoon, H. Kang, and I. Hwang. Robust wheel-slip control for brake-by-wire systems. *SAE Technical Paper 2005-01-1584*, 2005.

[62] Augsburg K. Savitski D. Ivanov, V. Torque vectoring for improving the mobility of all-terrain electric vehicles. In *Proceedings of the 12th ISTVS European Regional Conference*, Pretoria, South Africa, September 24-28 2012.

[63] V. Ivanov, K. Augsburg, D. Savitski, J. Plihal, P. Nedoma, and J. Machan. Advanced cost functions for evaluation of lateral vehicle dynamics. In *Proceedings of the FISITA 2012 World Automotive Congress*, volume 198 of *Lecture Notes in Electrical Engineering*, pages 425–440. Springer Berlin Heidelberg, 2013.

[64] E. J. Rossetter J. Ryu and J. C. Gerdes. Vehicle sideslip and roll parameter estimation using GPS. In *Proceedings of AVEC 2002*, Hiroshima, Japan, September 2002.

[65] B. Jacobsen. Potential of electric wheel motors as new chassis actuators for vehicle manoeuvring. *Proceedings of the Institution of Mechanical Engineers, Part D: Journal of Automobile Engineering*, 216(8):631–640, 2002.

[66] R. N. Jazar. *Vehicle Dynamics: Theory and Application*. Springer, New York, 2008.

[67] T. A. Johansen and T. I. Fossen. Control allocation - a survey. *Automatica*, 49(5):1087–1103, 2013.

[68] M. Jonasson and J. Andreasson. Exploiting autonomous corner modules to resolve force constraints in the tyre contact patch. *Vehicle System Dynamics*, 46(7):553–573, 2008.

[69] G. Kaiser, F. Holzmann, B. Chretien, M. Korte, and H. Werner. Torque vectoring with a feedback and feed forward controller - applied to a through the road hybrid electric vehicle. In *Intelligent Vehicles Symposium (IV), 2011 IEEE*, pages 448–453, 2011.

[70] G. Kaiser, Q. Liu, C. Hoffmann, M. Korte, and H. Werner. Torque vectoring for an electric vehicle using an LPV drive controller and a torque and slip limiter. In *Decision and Control (CDC), 2012 IEEE 51st Annual Conference on*, pages 5016–5021, 2012.

[71] L. Kakalis, A. Zorzutti, F. Cheli, and G. Travaglio. Brake based torque vectoring for sport vehicle performance improvement. *SAE Technical Paper 2008-01-0596*, 2008.

[72] M. Kamachi, K. Walters, and H. Yoshida. Improvement of vehicle dynamic performance by means of in-wheel electric motors. *Mitsubishi Motors Technical Review*, 18:106–112, 2006.

[73] A. Kampanakis, E. Siampis, E. Velenis, and S. Longo. 8th IFAC symposium on advances in automotive control, a torque vectoring optimal control strategy for combined vehicle dynamics performance enhancement and electric motor ageing minimisation. *IFAC Proceedings Volumes*, 2016.

[74] J. Kang, Y. Kyongsu, and H. Heo. Control allocation based optimal torque vectoring for 4WD electric vehicle. *SAE Technical Paper 2012-01-0246*, 2012.

[75] J. Kang, J. Yoo, and K. Yi. Driving control algorithm for maneuverability, lateral stability, and rollover prevention of 4WD electric vehicles with independently driven front and rear wheels. *Vehicular Technology, IEEE Transactions on*, 60(7):2987–3001, 2011.

[76] T. Keviczky, P. Falcone, F. Borrelli, J. Asgari, and D. Hrovat. Predictive control approach to autonomous vehicle steering. In *American Control Conference, 2006*, pages 6 pp.–, June 2006.

[77] H. K. Khalil. *Nonlinear Systems*. Pearson, Upper Saddle River, NJ, 3rd edition, 2003.

[78] U. Kiencke and L. Nielsen. *Automotive Control Systems For Engine, Driveline, and Vehicle*. Springer, New York, 2nd edition, 2005.

[79] D. Kim, S. Hwang, and H. Kim. Vehicle stability enhancement of Four-Wheel-Drive hybrid electric vehicle using rear motor control. *Vehicular Technology, IEEE Transactions on*, 57(2):727–735, 2008.

[80] D. Kim, K. Kim, W. Lee, and I. Hwang. Development of Mando ESP (Electronic Stability Program). *SAE Technical Paper 2003-01-0101*, 2003.

[81] D. H. Kim, J. M. Kim, S. H. Hwang, and H. S. Kim. Optimal brake torque distribution for a four-wheel-drive hybrid electric vehicle stability enhancement. *Proceedings of the Institution of Mechanical Engineers, Part D: Journal of Automobile Engineering*, 221(11):1357–1366, 2007.

[82] K. Kin, O. Yano, and H. Urabe. Enhancements in vehicle stability and steerability with slip control. *HONDA R&D Technical Review*, 13:91–98, 2001.

[83] D. E. Kirk. *Optimal Control Theory: An Introduction*. Dover Publications, New York, 2004.

[84] R. Kizu, H. Harada, and H. Minabe. Electronic control of car chassis present status and future perspective. In *Transportation Electronics, 1988. Convergence 88. International Congress on*, pages 173–188, 1988.

[85] S. Ko, J. Ko, S. Lee, J. Cheon, and H. Kim. Development of a vehicle stability control algorithm using velocity and yaw rate for an in-wheel drive vehicle. In *Vehicle Power and Propulsion Conference (VPPC), 2012 IEEE*, pages 24–27, 2012.

[86] K. Koibuchi, M. Yamamoto, Y. Fukada, and S. Inagaki. Optimal wheel torque distribution for a Four-Wheel-Drive fully electric vehicle. *SAE Technical Paper 960487*, 1996.

[87] R. Kunii, A. Iwazaki, Y. Atsumi, and A. Mori. Development of SH-AWD (Super Handling-All Wheel Drive) system. *HONDA R&D Technical Review*, 16:9–16, 2004.

[88] H. Leffler, R. Auffhammer, R. Heyken, , and H. Rth. New driving stability control system with reduced technical effort for compact and medium class passenger cars. *SAE Technical Paper 980234*, 1998.

[89] E. Liebemann and D. Fuehrer. More safety with vehicle stability control. *SAE Technical Paper 2007-01-2759*, 2007.

[90] E. K. Liebemann, K. Meder, J. Schuh, and G. Nenninger. Safety and performance enhancement: The Bosch Electronic Stability Control (ESP). *SAE Technical Paper 2004-21-0060*, 2004.

[91] Q. Liu, G. Kaiser, S. Boonto, H. Werner, F. Holzmann, B. Chretien, and M. Korte. Two-degree-of-freedom LPV control for a through-the-road hybrid electric vehicle via torque vectoring. In *Decision and Control and European Control Conference (CDC-ECC), 2011 50th IEEE Conference on*, pages 1274–1279, 2011.

[92] T. J. Gordon M. C. Best and P. J. Dixon. An Extended Adaptive Kalman Filter for real-time state estimation of vehicle handling dynamics. *Vehicle System Dynamics*, 34(1):57–75, 2000.

[93] J. M. Maciejowski. *Predictive control with constraints*. Prentice Hall, 2002.

[94] W. J. Manning and D. A. Crolla. A review of yaw rate and sideslip controllers for passenger vehicles. *Transactions of the Institute of Measurement and Control*, 29(2):117–135, 2007.

[95] D. Q. Mayne, J. B. Rawlings, C. V. Rao, and P. O. M. Scokaert. Constrained model predictive control: Stability and optimality. *Automatica*, 36(6):789 – 814, 2000.

[96] T. Miura, Y. Ushiroda, K. Sawase, N. Takahashi, and K. Hayashikawa. Development of integrated vehicle dynamics control system S-AWC. *Mitsubishi Motors Technical Review*, 20:21–25, 2008.

[97] M. Morari, C. E. Garcia, and D. M. Prett. Model predictive control: Theory and practice - A survey. *Automatica*, 25(3):335–348, 1989.

[98] S. Motoyama, H. Uki, K. Isoda, and H. Yuasa. Effect of traction force distribution control on vehicle dynamics. *Vehicle System Dynamics*, 22(5-6):455–464, 1993.

[99] K. Nam, H. Fujimoto, and Y. Hori. Lateral stability control of in-wheel-motor-driven electric vehicles based on sideslip angle estimation using lateral tire force sensors. *Vehicular Technology, IEEE Transactions on*, 61(5):1972–1985, 2012.

[100] M. Nanao and T. Ohtsuka. Nonlinear model predictive control for vehicle collision avoidance using C/GMRES algorithm. In *Control Applications (CCA), 2010 IEEE International Conference on*, pages 1630–1635, September 2010.

[101] L. De Novellis, A. Sorniotti, P. Gruber, J. Orus, Jose-Manuel R. Fortun, J. Theunissen, and J. De Smet. Direct yaw moment control actuated through electric drivetrains and friction brakes: Theoretical design and experimental assessment. *Mechatronics*, 26:1 – 15, 2015.

[102] K. Ogata. *Modern Control Engineering*. Pearson, Upper Saddle River, NJ, 5th edition, 2008.

[103] T. Ohtsuka. A continuation/GMRES method for fast computation of nonlinear receding horizon control. *Automatica*, 40(4):563 – 574, 2004.

[104] H. B. Pacejka and I. Besselink. *Tire and Vehicle Dynamics*. Butterworth-Heinmann, Oxford, 3rd edition, 2012.

[105] L. Pinto, S. Aldworth, M. Watkinson, P. Jeary, and M. Franco-Jorge. Advanced yaw motion control of a hybrid vehicle using twin rear electric motors. In *10th International Symposium on Advanced Vehicle Control*, Loughborough, UK, August 22-26 2010.

[106] D. Piyabongkarn, J. Y. Lew, R. Rajamani, and J. A. Grogg. Active driveline torque management systems. *IEEE Control Systems Magazine*, 30(4):86102, 2010.

[107] D. Piyabongkarn, J. Y. Lew, R. Rajamani, J. A. Grogg, and QingHui Yuan. On the use of torque-biasing systems for electronic stability control: Limitations and possibilities. *Control Systems Technology, IEEE Transactions on*, 15(3):581–589, 2007.

[108] D. Piyabongkarn, R. Rajamani, J. A. Grogg, and J. Y. Lew. Development and experimental evaluation of a slip angle estimator for vehicle stability control. *IEEE Transactions on Control Systems Technology*, 17(1):78–88, Jan 2009.

[109] J. H. Plumlee, D. M. Bevly, and A. S. Hodel. Control of a ground vehicle using quadratic programming based control allocation techniques. In *American Control Conference, 2004. Proceedings of the 2004*, volume 5, pages 4704–4709, 2004.

[110] S. J. Qin and T. A. Badgwell. A survey of industrial model predictive control technology. *Control Engineering Practice*, 11(7):733 – 764, 2003.

[111] W. Qiu, Q. Ting, Y. Shuyou, G. Hongyan, and C. Hong. Autonomous vehicle longitudinal following control based on model predictive control. In *Control Conference (CCC), 2015 34th Chinese*, pages 8126–8131, 2015.

[112] K. R. Schallock, K. Muske and J. P. Jones. Model Predictive Functional Control for an automotive three-way catalyst. *SAE Int. J. Fuels Lubr. 2(1):242-249*, 2009.

[113] R. Rajamani. *Vehicle Dynamics and Control*. Springer, New York, 2nd edition, 2012.

[114] R. Rajamani and D. Piyabongkarn. New paradigms for the integration of yaw stability and rollover prevention functions in vehicle stability control. *Intelligent Transportation Systems, IEEE Transactions on*, 14(1):249–261, 2013.

[115] J. Rauh and D. Ammon. System dynamics of electrified vehicles: some facts, thoughts, and challenges. *Vehicle System Dynamics*, 49(7):1005–1020, 2011.

[116] L. R. Ray. Nonlinear state and tire force estimation for advanced vehicle control. *IEEE Transactions on Control Systems Technology*, 3(1):117–124, Mar 1995.

[117] L. R. Ray. Nonlinear tire force estimation and road friction identification: Simulation and experiments. *Automatica*, 33(10):1819–1833, 1997.

[118] R. S. Rice. Measuring car-driver interaction with the g-g diagram. *SAE Technical Paper 730018*, 1973.

[119] R. Rieveley and B. Minaker. Variable torque distribution yaw moment control for hybrid powertrains. *SAE Technical Paper 2007-01-0278*, 2007.

[120] A. Rojas Rojas, H. Niederkofler, and W. Hirschberg. Mechanical design of in-wheel motor driven vehicles with torque-vectoring. *SAE Technical Paper 2011-36-0132*, 2011.

[121] H. Sakai. The dynamic properties of tires. *International Journal of Vehicle Design*, 2(1), 1981.

[122] S. Sakai and Y. Hori. Robustified model matching control for motion control of electric vehicle. In *Advanced Motion Control, 1998. AMC '98-Coimbra., 1998 5th International Workshop on*, pages 574–579, 1998.

[123] Y. M. Sam, M. R. H. A. Ghani, and N. Ahmad. LQR controller for active car suspension. In *TENCON 2000. Proceedings*, volume 1, pages 441–444 vol.1, 2000.

[124] S. Sarkka. On unscented kalman filtering for state estimation of continuous-time nonlinear systems. *Automatic Control, IEEE Transactions on*, 52(9):1631–1641, Sept 2007.

[125] K Sawase and K Inoue. Classification and analysis of lateral torque-vectoring differentials using velocity diagrams. *Proceedings of the Institution of Mechanical Engineers, Part D: Journal of Automobile Engineering*, 222(9):1527–1541, 2008.

[126] K. Sawase and Y. Sano. Application of active yaw control to vehicle dynamics by utilizing driving/braking force. *JSAE Review*, 20(2):289–295, 1999.

[127] K. Sawase, Y. Ushiroda, and T. Miura. Left-right torque vectoring technology as the core of Super All Wheel Control (S-AWC). *Mitsubishi Motors Technical Review*, 18:16–23, 2006.

[128] A. Shahzad. *New Optimization Methods in Predictive Control*. PhD thesis, Imperial College London, 2010.

[129] R. S. Sharp and H. Peng. Vehicle dynamics applications of optimal control theory. *Vehicle System Dynamics*, 49(7):1073–1111, 2011.

[130] R.S. Sharp and V. Valtetsiotis. Optimal preview car steering control. *Vehicle System Dynamics*, 35:101117, 2001.

[131] Y. Shibahata. Progress and future direction of chassis control technology. *Annual Reviews in Control*, 29(1):151–158, 2005.

[132] Y. Shibahata, N. Kuriki, K. Kitamura, K. Honda, K. Wada, H. Kajiwara, A. Nori, K. Kuwahara, and S. Okuma. Development of left-right torque distribution system. *HONDA R&D Technical Review*, 9:166180, 1997.

[133] E. Siampis. *Torque Vectoring in a Brunel Racing Electric Car*. BEng thesis, Department of Mechanical Engineering, Brunel University, 2012.

[134] E. Siampis, M. Massaro, and E. Velenis. Electric rear axle torque vectoring for combined yaw stability and velocity control near the limit of handling. In *Decision and Control (CDC), 2013 IEEE 52st Annual Conference on*, pages 1552–1557, 2013.

[135] F. Tahami, R. Kazemi, and S. Farhanghi. A novel driver assist stability system for all-wheel-drive electric vehicles. *Vehicular Technology, IEEE Transactions on*, 52(3):683–692, 2003.

[136] R. Tchamna and I. Youn. Yaw rate and side-slip control considering vehicle longitudinal dynamics. *International Journal of Automotive Technology*, 14(1):53–60, 2013.

[137] H. E. Tseng, B. Ashrafi, D. Madau, T. Allen Brown, and D. Recker. The development of vehicle stability control at Ford. *Mechatronics, IEEE/ASME Transactions on*, 4(3):223–234, 1999.

[138] Y. Ushiroda, K. Sawase, N. Takahashi, K. Suzuki, and K. Manabe. Development of Super AYC. *Mitsubishi Motors Technical Review*, 15:73–76, 2003.

[139] A. van Zanten. Bosch ESP systems: 5 years of experience. *SAE Technical Paper 2000-01-1633*, 2000.

[140] A. van Zanten, R. Erhardt, and G. Pfaff. VDC, the Vehicle Dynamics Control system of Bosch. *SAE Technical Paper 950759*, 1995.

[141] A. van Zanten, R. Erhardt, G. Pfaff, F. Kost, U. Hartmann, and T. Ehret. Control aspects of the Bosch-VDC. In *Proceedings of AVEC 1996*, Aachen, Germany, June 1996.

[142] E. Velenis, E. Frazzoli, and P. Tsiotras. On steady-state cornering equilibria for wheeled vehicles with drift. In *48th IEEE Conference on Decision and Control*, Shanghai, China, December 16-18 2009.

[143] E. Velenis, D. Katzourakis, E. Frazzoli, P. Tsiotras, and R. Happee. Steady-state drifting stabilization of RWD vehicles. *Control Engineering Practice*, 19(11):1363 – 1376, 2011.

[144] J. C. Wheals. Torque vectoring driveline: SUV-based demonstrator and practical actuation technologies. *SAE Technical Paper 2005-01-0553*, 2005.

[145] J. C. Wheals, H. Baker, K. Ramsey, and W. Turner. Torque vectoring AWD driveline: Design, simulation, capabilities and control. *SAE Technical Paper 2004-01-0863*, 2004.

[146] J. C. Wheals, M. Deane, S. Drury, and G. Griffith. Design and simulation of a torque vectoring rear axle. *SAE Technical Paper 2006-01-0818*, 2006.

[147] L. Xiong and Y. Zhuoping. Control allocation of vehicle dynamics control for a 4 in-wheel-motored EV. In *Power Electronics and Intelligent Transportation System (PEITS), 2009 2nd International Conference on*, volume 2, pages 307–311, 2009.

[148] K. Shimada Y. Shibahata and T. Tomari. The improvement of vehicle maneuverability by direct yaw moment control. In *Proceedings of AVEC 1992*, Yokohama, Japan, September 1992.

[149] H. Yu, W. Liang, M. Kuang, and R. McGee. Vehicle handling assistant control system via independent rear axle torque biasing. In *American Control Conference, 2009. ACC '09.*, pages 695–700, 2009.

[150] M. Zanon, J. V. Frasch, and M. Diehl. Nonlinear Moving Horizon Estimation for combined state and friction coefficient estimation in autonomous driving. In *Control Conference (ECC), 2013 European*, pages 4130–4135, July 2013.